

Dissertation
Submitted to the
Combined Faculties for Natural Sciences and for Mathematics
of Ruperto-Carola University of Heidelberg, Germany
for the degree of
Doctor of Natural Sciences

presented by
B.Sc. (Hons) Chemistry
Aritra Chowdhury
Kolkata, India
20.09.2018

Deciphering Interaction and Water Dynamics in Intrinsically Disordered Proteins with High Resolution Spectroscopic Tools

Referees: Dr. Jonas Ries

Prof. Dr. Michael Knop

Summary

Despite its utmost significance in biology, water dynamics has often been the ‘elephant in the room’ in experimental biophysics, owing to the challenges in measuring it. Water dynamics becomes more significant in case of intrinsically disordered proteins (IDPs) as IDPs fall out of the classical ‘structure-function’ paradigm and thus the typical structure-function relationship is modified to a dynamics-function relationship for IDP recognition. No study so far touched the highly important and complex topic on solvation dynamics on protein-protein interactions, let alone IDP recognition. In my PhD thesis my main aim has been to interrogate the interplay between solvation dynamics and binding mechanisms of IDPs involved in the nucleocytoplasmic transport pathway using a combination of steady state and picosecond resolved ensemble fluorescence spectroscopy and single molecule FRET (smFRET). I interrogated surface water dynamics in IDPs and its attenuation upon partner binding using three IDPs from the nucleocytoplasmic transport pathway, Nup153FG, NSP1FG and IBB which share one common binding partner, the nuclear transport receptor (NTR), Importin β , despite having different binding mechanisms and sites. Nup153FG and NSP1FG belong to the class of IDPs known as FG Nups, that constitute the permeability barrier of the nuclear pore complex (NPC). FG Nups bind Importin β through a set of ultrafast transient multivalent interactions retaining its disorder change while IBB forms a helix upon binding Importin β . Solvent fluctuations in the dynamic Nup153FG-Importin β complex and NSP1FG-Importin β complex were unperturbed relative to the unbound state while in the IBB-Importin β complex substantial relative slowdown of water dynamics was seen. These results directly showed a correlation between interfacial water dynamics and the plasticity of IDP complexes. Based on my results I concluded that solvation retardation poses energy barriers to conformational fluctuations, thus IDPs engage their partners with tunable solvation retardation, which directly correlates to their dynamics in the complex, enabling them to achieve functional diversity. In the context of nucleocytoplasmic transport such differential behavior of these two IDPs can be linked to their functions as well; dynamic FG Nup-Importin β complex likely expedites fast nucleocytoplasmic transport; while stable IBB-Importin β warrants integrity of the import-complex during a transport event.

Additionally I also performed femtosecond resolved fluorescence spectroscopy to explore the dynamics of IBB recognition by Importin β across timescales spanning over 5 orders of magnitudes from 100fs to ~20ns. Capturing the entire timescale of the dynamics enabled me to look at the nature of these dynamics more closely. Contrary to several hypotheses reporting protein solvation dynamics to be governed by discrete timescales I found that the dynamics could be well explained by a power law type of relaxation suggesting a possible entanglement of the different timescales. This provides new insights into the nature of protein solvation dynamics in general as well in the context of IDP recognition.

Zusammenfassung

Ungeachtet der äußerst wichtigen Rolle in der Biologie, ist wegen der messtechnischen Problematik die Wasserdynamik oft ein totgeschwiegenes Thema in der experimentellen Biophysik. Wasserdynamiken sind vor allem für die Funktion von intrinsisch ungeordneten Proteinen relevant (IDPs), weil IDPs nicht in das klassische „Struktur-Funktion“-Paradigma passen und somit die typische „Struktur-Funktion“-Beziehung zu einer „Dynamik-Funktion“-Beziehung für die IDP Erkennung verändert wird. Bisher hat keine Studie dieses sehr wichtige und komplexe Thema der Solvatisierungsdynamik von Protein-Protein-Interaktionen in diesem Zusammenhang bearbeitet. Der Hauptfokus meiner Doktorarbeit war es, das Zwischenspiel von Solvatisierungsdynamik und Bindungsmechanismus von IDPs, die im nukleocytoplasmatischen Transport involviert sind, mithilfe von einer Kombination aus stationärer und pikosekunden auflösender Ensemble-Fluoreszenz-Spektroskopie, sowie Einzel-Molekül FRET (smFRET) zu untersuchen. Ich analysierte Oberflächenwasserdynamiken in IDPs bei der Partnerbindung unter Verwendung von drei IDPs des nukleocytoplasmatischen Transportweges, Nup153FG, NSP1FG und IBB. Diese IDPs haben alle einen gemeinsamen Bindungspartner, den nuklearen Transportrezeptor (NTR) Importin β , jedoch unterschiedliche Bindungsmechanismen und -seiten. Nup153FG und NSP1 gehören zu der Klasse von IDPs, auch bekannt als FG-Nups, die die Permeabilitätsbarriere des Kernporenkomplexes (nuclear pore complex, NPC) bilden. FG-Nups binden Importin β durch eine Reihe von ultraschnellen transienten multivalenten Interaktionen ihre ungeordnete Struktur beibehaltend, während IBB sich bei der Bindung an Importin β zu einer Helix formt. Solvent-Schwankungen im dynamischen Nup153FG-Importin β - und NSP1-Importin β -Komplex blieben unbeirrt, verglichen mit dem ungebundenen Zustand, wohingegen im IBB-Importin β -Komplex eine substantielle Verlangsamung der Wasserdynamik beobachtet werden konnte. Diese Resultate zeigten unmittelbar eine Korrelation zwischen Grenzflächenwasserdynamiken und der Verformbarkeit von IDP-Komplexen. Basierend auf meinen Resultaten kann ich daraus schliessen, dass Solvatisierungsverzögerungen Energiebarrieren zu Konformationsfluktuationen produzieren. Im Zusammenhang mit dem nukleocytoplasmatischen Transport fördert der dynamische FG-Nup-Importin β -Komplex wahrscheinlich einen schnellen nukleocytoplasmatischen Transport, während der stabile IBB-Importin β -Komplex die Integrität des Import-Komplexes bei einem Transportereignis garantiert.

Zusätzlich habe ich auch femtosekunden aufgelöste Fluoreszenz Spektroskopie zur Bestimmung von Dynamiken der IBB Erkennung durch Importin β über eine Zeitspanne von 5 Größenordnungen (von 100fs zu \sim 20ns) durchgeführt. Das Erfassen der gesamten Zeitspanne der Dynamiken ermöglicht mir genauer auf die Natur dieser Dynamiken zu schauen. Im Gegensatz zu diversen Hypothesen, die von Protein-Solvatisierungsdynamiken beherrscht von diskreten Zeitskalen berichten, habe ich herausgefunden, dass die Dynamiken durch ein Potenzgesetz von Relaxationen, und somit einer möglichen Verbindung der unterschiedlichen Zeitskalen, sehr gut erklärt werden können. Dies bietet neue generelle Einblicke in die Natur von Protein-Solvatisierungsdynamiken im Zusammenhang von IDP Erkennung.

Publications List

1. Comment on “Innovative scattering analysis shows that hydrophobic disordered proteins are expanded in water”
G. F. Vives*, N. Banterle*, K. M. Ruff*, **A. Chowdhury***, R. V. Pappu, D. I. Svergun, Edward A. Lemke
Science (Conditionally Accepted)
2. Dissecting two opposing binding mechanisms of FG-nucleoporins and nuclear transport receptors
P. S. Tan*, I. V. Aramburu*, D. Mercadante*, S. Tyagi, **A. Chowdhury**, D. Spitz, F. Gräter, E. A. Lemke
Cell Reports, 22, 3660 (2018)
3. Decoupling of size and shape fluctuations in heteropolymeric sequences reconciles discrepancies in SAXS versus FRET measurements
G. F. Vives*, N. Banterle*, K. M. Ruff*, **A. Chowdhury**, D. Mercadante, C. Koehler, M. Kachala, G. E. Girona, S. Milles, A. Mishra, P. R. Onck, F. Gräter, S. Esteban-Martín, R. V. Pappu, D. I. Svergun, E. A. Lemke
PNAS 114: E6342–E6351 (2017)

*Contributed equally

Table of contents

Summary	i
Zusammenfassung	ii
Publications List.....	iii
Table of contents	v
List of figures	ix
List of abbreviations	xi
1 Introduction	2
1.1 IDPs in cellular function	2
1.1.1 IDPs evade the structure-function paradigm.....	2
1.1.2 Sequence determinants of intrinsic disorder	3
1.1.3 Binding mechanisms of IDPs.....	4
1.1.4 Functions of IDPs in the cell function and organization.....	6
1.2 Nucleocytoplasmic transport and the nuclear pore complex	7
1.2.1 The nuclear pore complex: Structure, function and the nucleocytoplasmic transport pathway 7	
1.2.2 FG-Nups	9
1.2.3 Nuclear transport receptors	11
1.2.4 Dynamics of interaction of NTRs with FG-Nups; towards deciphering the transport paradox 13	
1.3 Water in bio-molecular recognition	18
1.3.1 Water is universal necessity for life.....	18
1.3.2 Approaches to measure water dynamics.....	19
1.3.3 Principles of TDFSS	21
1.3.4 Dynamics of water in bulk and in biological matrices	22
1.3.5 Solvation dynamics in IDPs.....	25

2	Objectives	28
2.1	Relationship between solvation dynamics and IDP binding mechanism.....	28
2.1.1	Construction of a picosecond resolved TCSPC (Time Correlated Single Photon Counting) setup and establishment of solvation dynamics measurements using TDFSS	28
2.1.2	Measurement of solvation dynamics in an IDP (IBB) that forms a complex via a coupled-folding mechanism (IBB-Importin β).....	28
2.1.3	Measurement of solvation dynamics in FG Nups that form a complex via a fuzzy binding mechanism (FGNup-Importin β).....	29
2.1.4	Comparison and rationalization of the extent of solvation dynamics modulation in IDPs upon complex formation using different mechanisms.	29
2.2	Probing all the timescales of IDP recognition.....	29
2.2.1	Probing femtosecond resolved solvation dynamics for IBB recognition	29
3	Materials and methods.....	31
3.1	Methods.....	31
3.1.1	Purification of recombinant proteins	31
3.1.2	Fluorescent labeling of recombinant proteins.....	38
3.1.3	Fluorescence lifetime measurements using TCSPC	40
3.1.4	Time resolved anisotropy measurements.....	42
3.1.5	Solvation dynamics measurement using Time Dependent Fluorescence Stokes Shift (TDFSS) method.....	43
3.1.6	Basics of FRET and smFRET analysis pipeline	46
3.1.7	Single molecule Fluorescence Correlation Spectroscopy (FCS).....	48
3.1.8	Measuring static microenvironment polarity with acrylodan steady state emission 50	
3.1.9	Measuring apparent disassociation constants (K_D) of Nup153FG and Importin β using acrylodan lifetime	51
3.2	Materials.....	52
3.2.1	List of commonly used chemicals.....	52
3.2.2	List of SEC columns and concentration devices used for protein purification.....	52
3.2.3	List of solvents used in spectroscopy.....	53
3.2.4	List of synthetic fluorescent dye	53
3.2.5	List of commercial kits	54
3.2.6	List of <i>E.Coli</i> strains	54

3.2.7	List of specialized software	54
4	Results	56
4.1	Building and characterization of the TCSPC setup.....	56
4.1.1	Construction of the TCSPC setup.....	56
4.1.2	Characterisation of the TCSPC setup	58
4.2	Dynamic characterization of an IDP complex formed via coupled folding and binding	60
4.2.1	Single molecule studies of IBB recognition by Importin β	60
4.2.2	Probing IBB-Importin β interaction with acrylodan fluorescence.....	63
4.2.3	Probing solvation dynamics at IBB surface and the IBB-Importin β interface	66
4.3	Dynamic characterisation of an IDP complex formed via a fuzzy binding mechanism	68
4.3.1	Probing Nup153-Importin β interaction with acrylodan fluorescence	69
4.3.2	Local disassociation constants (K_D) for Nup153FG-Importin β interaction.....	72
4.3.3	Site selective chain motions of Nup153FG in the fuzzy complex using time resolved anisotropy measurements.....	74
4.3.4	Site selective solvation dynamics in free Nup153FG and Nup153FG in the fuzzy complex with Importin β	76
4.4	Dynamic characterization of a fuzzy complex NSP1FG and Importin β	79
4.4.1	Single molecule characterisation of fuzzy complex formation by NSP1FG.	79
4.4.2	Site specific acrylodan fluorescence to characterise NSP1FG-Importin β interface	81
4.4.3	Site specific solvation dynamics of NSP1FG and the NSP1FG-Importin β interface	83
5	Discussion.....	87
5.1	Implications of interfacial solvation dynamics in the plasticity of IDP-protein complexes.....	87
5.2	Complementation of solvation dynamics spectroscopic experiments with MD (Molecular Dynamics) Simulation	91
5.2.1	Challenges of monitoring solvation dynamics.....	91
5.2.2	Correspondence of the MD simulations with spectroscopy; insights from the combined approach.....	92
5.3	Implications of interfacial solvation dynamics in the plasticity of IDP-protein complexes.....	97
6	Outlook	100
6.1	Principles of measuring TDFSS using fsTA spectroscopy and its advantages.....	100

6.1.1	Basics of fsTA principles and schematic representation of data	100
6.1.2	TDFSS measurement from SE band from fsTA spectroscopy	102
6.2	Femtosecond resolved solvation dynamics of IBB and IBB-Importin β	105
6.2.1	Obtaining TDFSS data from 100 fs to ~15 ns for IBB and IBB-Importin β using a combination of fsTA data and TCSPC data.	105
6.2.2	Power law nature of solvent response of IBB and IBB-Importin β	108
	Acknowledgements.....	113
	Bibliography	115

List of figures

Figure 1.1 IDPs evade the structure-function paradigm.	3
Figure 1.2 Sequence descriptors of IDPs and folded proteins	4
Figure 1.3 Binding mechanisms of IDPs	5
Figure 1.4 Phase separation to facilitate cellular organization.	7
Figure 1.5 Schematic of the human NPC showing constituent FG Nups.	10
Figure 1.6 Structures of different NTRs.	12
Figure 1.7 Structures of different NTRs complexed with FG motifs.	14
Figure 1.8 Schematic representation of FG domain NTR interaction.	17
Figure 1.9 Schematic representation showing different approaches to measure solvation dynamics	19
Figure 1.10 Schematic representation of the role of hydrophobic effect in biology.	20
Figure 1.11 Principle of TDFSS measurements.	22
Figure 1.12 Schematic representation of the role of solvation dynamics on molecular recognition	24
Figure 1.13 Schematic representation of water structural transition during amyloid formation ..	26
Figure 3.1 Representative purification of Nup153FG single cysteine mutants	32
Figure 3.2 Representative purification of IBB.	34
Figure 3.3 Selectivity of acrylodan labelling	39
Figure 3.4 G factor calibration using Bis-ANS in methanol	43
Figure 3.5 Schematic showing the pipeline of TRES measurement.	45
Figure 4.1 Schematic and photograph of the TCSPC setup.	57
Figure 4.2 IRF of the TCSPC setup.	58
Figure 4.3 Solvation dynamics of C153 in Triton-X micelles.	59
Figure 4.4 smFRET to probe IBB-Importin β interaction	61
Figure 4.5 rms distance of a model Gaussian chain and a helix	62
Figure 4.6 FCS of IBB-Importin β recognition	63
Figure 4.7 Acrylodan emission and lifetime in IBB-Importin β interaction.	64
Figure 4.8 Relative permittivity for IBB in presence and absence of Importin β	65
Figure 4.9 Solvation dynamics of IBB in presence and absence of Importin β	67
Figure 4.10 Acrylodan emission and lifetime in Nup153FG-Importin β interaction	70
Figure 4.11 Relative permittivity for Nup153FG in presence and absence of Importin β	71
Figure 4.12 Titration of acrylodan labelled Nup153FG mutants with Importin β	73
Figure 4.13 Time resolved anisotropy decay of Nup153FG.	75
Figure 4.14 Solvation dynamics of Nup153FG mutants in presence and absence of Importin β . ..	77
Figure 4.15 smFRET and FCS to probe fuzzy complex formation between NSP1FG fragment and Importin β	80
Figure 4.16 Acrylodan emission and lifetime in NSP1-Importin β interaction.	82

Figure 4.17 Relative permittivity for NSP1 in presence and absence of Importin β	82
Figure 4.18 Solvation dynamics of NSP1 101C in presence and absence of Importin β	84
Figure 5.1 Comparison of solvation dynamics modulation upon partner binding in IDPs; fuzzy complex formation vs coupled folding-binding.....	88
Figure 5.2 A model highlighting potential regulatory roles of solvation dynamics in governing plasticity of IDP in a complex	90
Figure 5.3 Regions of interest defined for solvation dynamics analysis by MD simulations	93
Figure 5.4 Analysis of solvation dynamics from MD simulations	95
Figure 5.5 Comparison of solvation dynamics from MD simulations and spectroscopy.....	96
Figure 6.1 A schematic of fsTA spectroscopy	101
Figure 6.2 Schematic of stimulated emission	101
Figure 6.3 Schematic of fsTA spectra.....	102
Figure 6.4 fsTA spectra for acrylodan labelled BSA.....	103
Figure 6.5 Schematic for frequency determination of an SE band of an fsTA spectra	104
Figure 6.6 TDFSS measured with fsTA spectroscopy on BSA labelled acrylodan	104
Figure 6.7 TDFSS measured with fsTA spectroscopy on IBB and IBB-Importin β	105
Figure 6.8 TDFSS measured from TCSPC traces normalized to fluorescence oscillator distribution obtained from fsTA spectroscopy	107
Figure 6.9 TDFSS from 100 fs to ~20 ns from combined fsTA and TCSPC data for IBB and IBB-Importin β	108
Figure 6.10 C(t) and p(τ) from inverse Laplace transform of C(t) for IBB and IBB-Importin β .	110
Figure 6.11 type relaxation of solvation in IBB and IBB-Importin β	111

List of abbreviations

aaRS: aminoacyl t-RNA Synthetase
AcF : *p*-acetylphenylalanine
CBD: Chitin Binding Domain
CBP : CREB binding protein
CryoET: Cryo Electron Tomography
EDTA: Ethylene Diamine Tetracetic Acid
FCS : Fluorecence Correlation Spectroscopy
FRET : Fluorescence Resonance Energy Transfer
fsTA: femtosecond Transient Absorption
fwhm : full width at half maxima
IDP : Intrinsically Disordered Protein
IDR : Intrinsically Disordered Regions
IPTG: Isopropyl β -D-1-thiogalactopyranoside
IRF : Instrument Response Function
kcps : kilocounts per second
 K_D : disassociation constants
kDa : kilo Dalton
LB: Lysogeny broth
MD : Molecular Dynamics
MEM: Maximum Entropy Method
NES : Nuclear Export Signal
NLS : Nuclear Localization Signal
NMR : Nuclear Magnetic Resonance
NPC : Nuclear Pore Complex
NTA: Nitrilotriacetic acid
NTR : Nuclear Transport Receptor
OD: Optical Density
PAGE: Polyacrylamide Gel Electrophoresis
PBS : Phosphate Buffere Slaine
PDB: Protein Data Bank
PMSF: Phenyl Methane Sulfonyl Fluoride
rms : root mean squared
SDS: Sodium Dodecyl Sulfate
SEC: Size Exclusion Chromatography
SLiMs : Short Linear Motifs
smFRET : single molecule FRET
TB: Terrific Broth

TCSPC : Time Correlated Single Photon Counting

TCEP: Tris(2-carboxyethyl)phosphine TDFSS: Time Dependant Fluorescence Stokes Shift

TRES : Time Resolved Emission Spectra

Chapter 1

1 Introduction

1.1 IDPs in cellular function

1.1.1 IDPs evade the structure-function paradigm

Folded proteins have a defined three dimensional structure determined solely by its primary sequence. This principle holds a central place in biology and is a direct predecessor of the so called 'structure-function' paradigm which suggests a well-defined 3D structure encodes a specific function and thus by extrapolation a well-defined structure is a necessity for biological functionality¹. There has been substantial evidence for this dogma based on the ever increasing numbers of structures in Protein Data Bank (PDB). Several observations support this notion; for example a striking structural similarity of enzymes and often correspondence of structural footprints with evolution of molecular function support this dogma^{2,3}.

However, there has been increasing evidences that a significant number of proteins remain unfolded in physiological conditions^{4,5,6,7}. Such proteins adopt a multitude of rapidly interconverting structures instead of one predominant structure in contrast to folded proteins. Such proteins or such regions in a protein are thus named intrinsically disordered proteins (IDPs) or intrinsically disordered regions (IDRs) respectively^{8,9}. For sake of simplicity I will henceforth refer to both IDRs and IDPs as IDPs. After the human genome project, advanced protein structure prediction algorithms^{10,11,12} soon led to the realization that a large part of human proteins, reaching up to ~40%¹³ of the proteome, contain disordered regions. Protein synthesis is an energy expensive process for a living cell¹⁴ and the discussions above indeed prompt us to think if functionality was solely a fallout of structure why would a cell expend its resources into synthesizing IDPs; suggesting there must be 'method in the madness'. It has been shown that eukaryotes/complex life forms have significantly larger disorder in their proteomes compared to elementary organisms such as bacteria which typically have less than 10% of disordered proteins¹⁵ in their proteome. This indicates that IDPs might be crucial to several complex functionalities necessary for cellular function¹⁶. As is discussed below, an IDP has certain sequence idiosyncrasies that encode disorder and subsequently a function. Hence IDPs evade the classical structure-function paradigm and an alternate paradigm has to be invoked to comprehend IDP function where the sequence encodes disorder which encodes function¹⁷ (Fig 1.1).

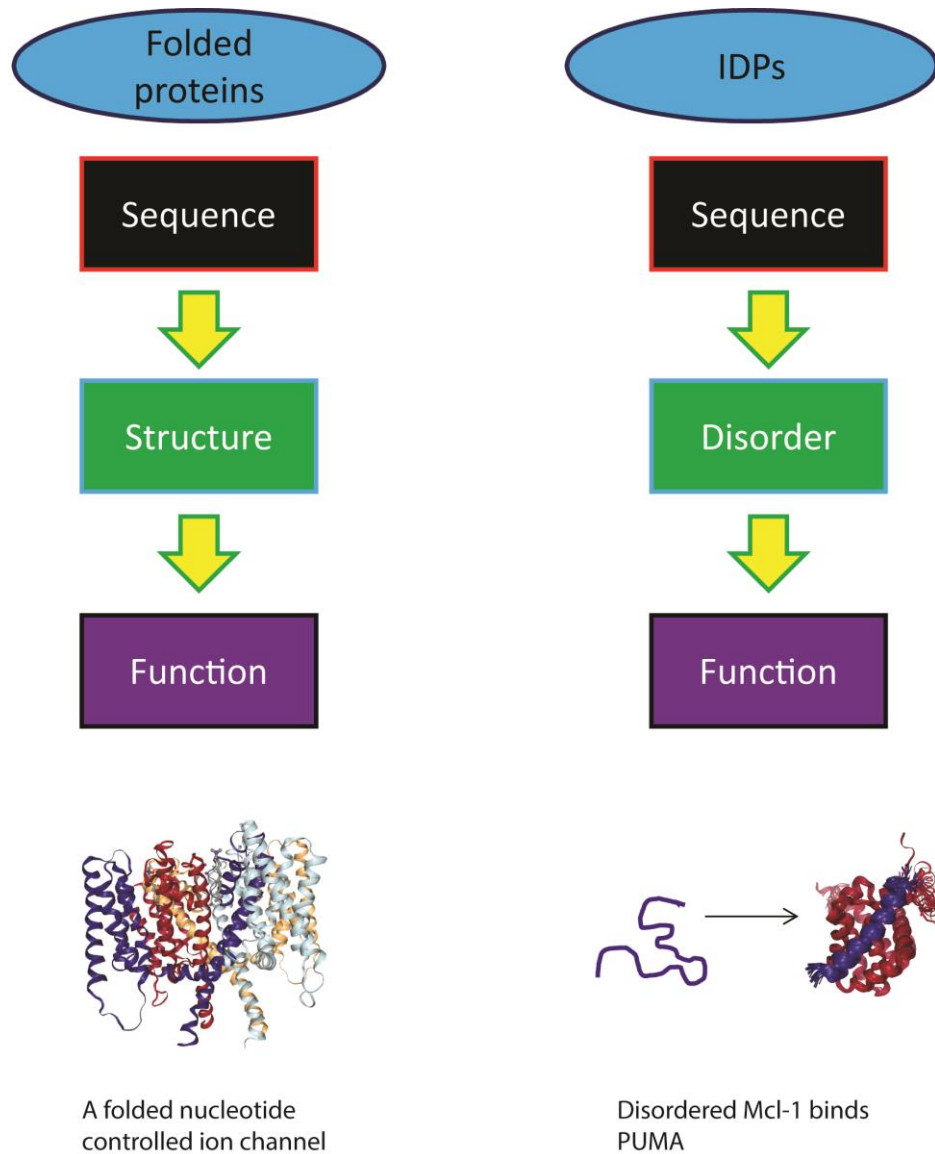


Figure 1.1 IDPs evade the structure-function paradigm: Folded proteins perform a function governed by their structure establishing the structure-function paradigm, as shown on the left for an ion channel (PDB:3BEH). However, IDPs have sequences that encode disorder which subsequently performs a function as shown on the right for disordered BH3 domain of PUMA (in violet) which binds Mcl-1 (red).

1.1.2 Sequence determinants of intrinsic disorder

Folded proteins have certain sequence characteristics that help them attain a folded globular structure. These sequence features include a certain fraction of hydrophobic residues that favor formation of a collapsed state where the hydrophobic side-chains are buried and allow secondary

structure elements to form. Unbalanced charge residues drive expansion of the protein ensemble due to electrostatic repulsive forces and hence there is a degree to which folded proteins can tolerate presence of such unbalanced charged residues. A comprehensive sequence analysis of numerous IDPs by Uversky et. al. showed a clear trend in the sequence composition of IDPs, IDPs systematically have more unbalanced charges and less hydrophobic residues compared to folded proteins¹⁸. The coordinates occupied by folded and disordered proteins on a plot of mean net charge vs mean hydrophobicity showed they were well segregated in terms of sequence space. This analysis even led to an empirical relation that led to a clear separation of the sequence space into folded and unfolded regions. (Fig 1.2). This suggests the presence of a threshold point in terms of the mean hydrophobicity relative to mean net charge after which proteins fail to fold¹⁸.

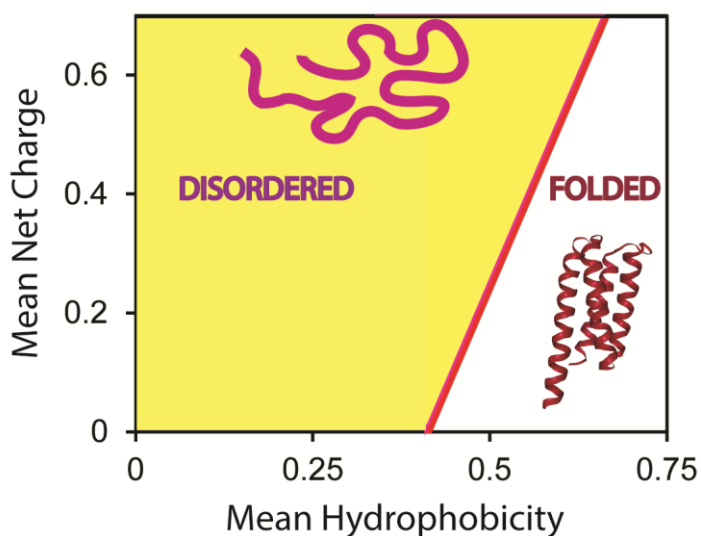


Figure 1.2 Sequence descriptors of IDPs and folded proteins: A plot of mean net charge vs mean hydrophobicity for several IDPs and folded proteins (PDB:3U3B) in [18] showed a clear demarcation in the sequence space between folded proteins and IDPs which is reproduced here. The boundary is given by the equation $R=2.785H-1.151$ where R and H are the mean net charge and mean hydrophobicity respectively¹⁸.

1.1.3 Binding mechanisms of IDPs

IDPs are known to bind several biological targets. The binding interactions of IDPs can be primarily classified into at least two categories which are: 1) Coupled folding-binding and 2) Fuzzy complex formation (Fig 1.3)^{19,20,21,22,23}. Coupled folding-binding mechanisms involve folding transition of the IDP where in the bound state the IDP adopts a folded structure. In such a binding mechanism the binding partner offers structure forming interactions which the IDP otherwise lacks, allowing it to adopt a folded structure in the context of the bound complex. Coupled folding-binding mechanisms again come in two flavors; induced fit and conformational

selection²⁴. In case of an induced fit mechanism the entire disordered ensemble can bind the partner and the folding transition occurs after binding. In contrast, for a conformational selection mechanism, a binding prone minor conformation in the disordered ensemble bearing significant resemblance to the bound state is selected out of equilibrium ensemble of structures by the binding partner. This unbound ensemble re-equilibrates producing again some binding competent conformers which again bind the partner and the process continues populating the bound state. Thus for a conformational selection the folding or structural transition primarily happens prior to the binding event.

Fuzzy complexes are formed when the disordered ensemble retains its disorder after binding the partner, without undergoing any folding transition. In several cases these involve multivalent interactions between the IDPs and the partner proteins where multiple small binding epitopes on the IDP serve as points of anchorage with the binding partner^{25,26}. Several IDPs contain short linear motifs (SLiMs)^{27,28} which serve as binding epitopes to engage a partner and multiple copies of such SLiMs can be present allowing the IDP to engage in multivalent interactions with the partner; such multivalency cooperatively leads to an increase in overall binding affinity but at the same time the small size of the epitopes allows the IDP to bind the partner and remain disordered without undergoing a folding transition.

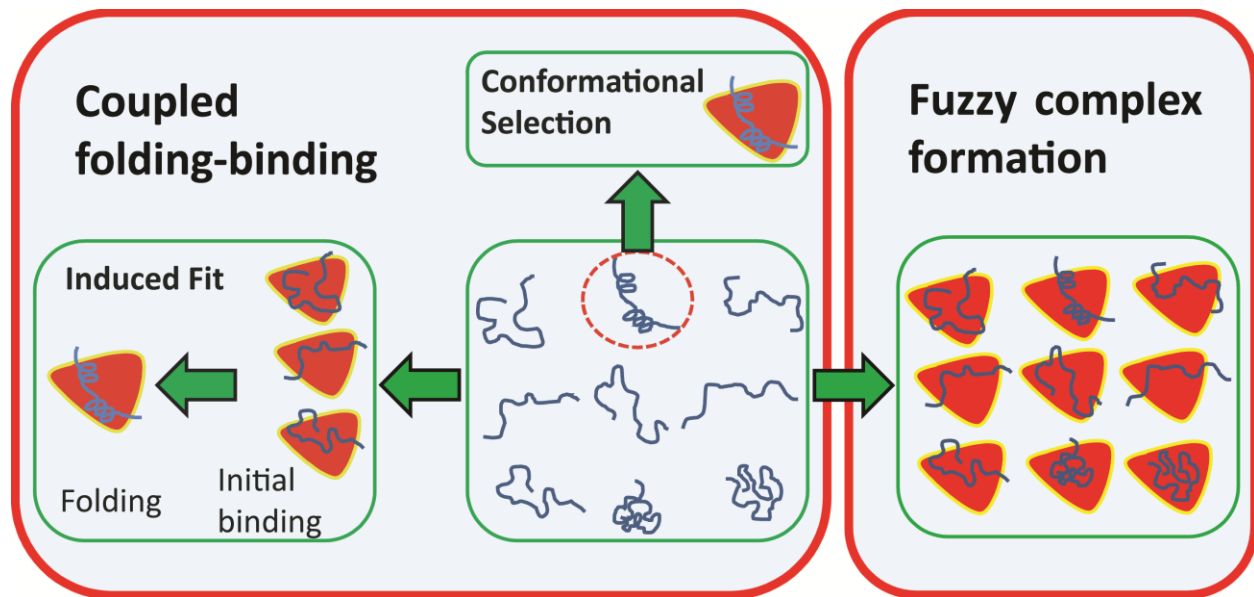


Figure 1.3 Binding mechanisms of IDPs: The schematic shows the binding mechanisms which IDPs deploy to engage binding partners, which can be sub divided into two broad classes coupled folding-binding (left) and fuzzy complex formation (right). For a fuzzy complex as shown on the right, the entire disordered ensemble is competent in binding the partner maintaining disorder. For coupled folding-binding scenarios, the IDP adopts a structured state upon binding; in an induced fit mechanism the folding occurs after binding and in a conformational selection mechanism the folding occurs before binding.

1.1.4 Functions of IDPs in the cell function and organization

It has now been clear that IDPs acts as key players in cellular regulation and function. Thus, it is fair to say IDPs form a cornerstone in eukaryotic cell biology as we know it.

Sequence analysis reveals a very high content of long disordered regions in proteins involved in transcription regulation like transcriptional factors, transcription co-activators and trans-activators, and chromosomal proteins like linker histones^{29,30,31}. The disordered regions play many roles in such cases³². IDPs can constitute linker regions between recognition motifs/domains in molecules acting as molecular hubs and facilitate allosteric interactions between distant sites. One classic example is the (CREB binding protein) CBP/p300 which harbors multiple sites for transcription factor separated by IDPs³³. Such a scaffold offers the possibility of allosteric and cooperative interactions. Interestingly several of the transcription factors that bind CBP/p300 are themselves disordered as well³³. IDPs due to their promiscuous binding behavior can also themselves act as nodal points in regulatory pathways and encode regulatory and signaling function¹⁶, a prime example being the transcription factor p53 that bears long disordered N and C-terminal domains and forms hub in cellular protein interaction network having ~100s of binding partners^{34,35}. IDPs having large surfaces are susceptible to posttranslational modifications, which happen to be a facile way to achieve dynamic regulation. Such regulatory mechanisms are widely seen in IDPs functioning at all stages of transcription regulation, ranging from transcription factors regulated by phosphorylation such as p53 to dynamic regulation of transcription via post translational modifications in the disordered tails of histones^{36,37}.

Owing to their disorder, physical chemistry of IDPs in solution, such as collapse, scaling of global dimensions with sequence length and phase behavior, can be explained to a large extent, based on the basic tenets of polymer physics³⁸. Hence, like polymers in solution IDPs can undergo phase separation forming a concentrated phase surrounded by a dilute phase (Fig 1.4)³⁹. In the recent years the discovery that many cellular organelles such as stress granules, P-bodies, nucleoli, Cajal-bodies, etc. are formed by liquid-liquid phase separation and are often driven by IDPs have led to fundamental new insights in cellular organization. In fact the permeability of the nuclear pore complex (NPC), is also hypothesized to be formed by phase separated IDPs (discussed in greater details in the following sections)^{40,41,42,43,44,45}. Thus, IDPs play a crucial role in cellular organization by forming different membraneless organelles, under different conditions via liquid-liquid phase separation, which serves as crucibles for several biochemical reactions which are otherwise not feasible in dilute concentrations.

Dispersed phase

Phase separated state

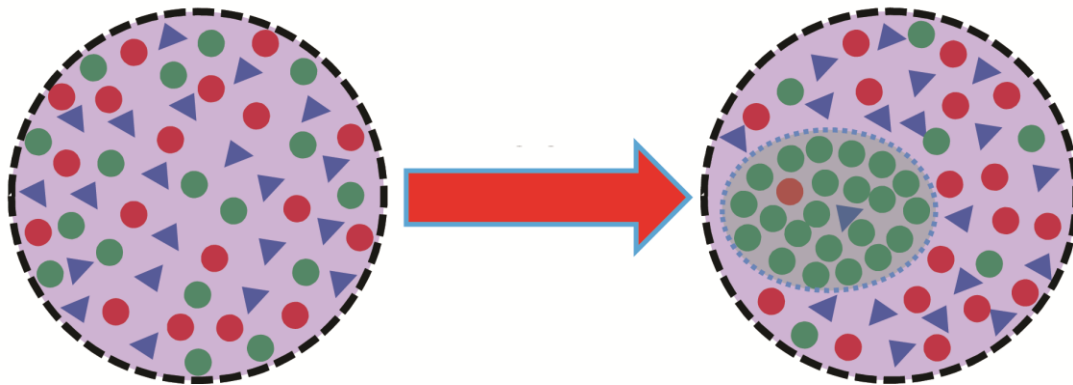


Figure 1.4 Phase separation to facilitate cellular organization: The schematic shows a dispersed phase which shows different molecules in blue, red and green (left). The green molecule bears an IDP. Certain conditions or changes in conditions results in liquid-liquid phase separation that leads to formation of a concentrated phase primarily composed of the green molecules (right) surrounded by a dilute phase.

1.2 Nucleocytoplasmic transport and the nuclear pore complex

1.2.1 The nuclear pore complex: Structure, function and the nucleocytoplasmic transport pathway

A cornerstone of eukaryotic cell-biology is the compartmentalization of cellular components. A eukaryotic cell is primarily compartmentalized into two components; the nucleus, which is a double membrane bound enclosure that harbors DNA/genetic information, surrounded by the cytosol, which constitutes an aqueous milieu containing the essential bio-molecules required for cellular function. Transport of molecules from the cytoplasm to the nucleus and vice-versa is crucial for cellular homeostasis. The nuclear envelope is decorated with several nuclear pore complexes (NPCs), which are giant macromolecular complexes that serve as the primary and in most cases the sole conduit for transport of molecules across the nuclear envelope between the nucleus and cytoplasm⁴⁶.

The megadalton sized NPC (with a size of 120 MDa in human) is one of the largest macromolecular complex in the eukaryotic cell. Since long the NPC had been known in the literature to have a ring like architecture with an apparent 8 fold rotational symmetry⁴⁷. Recent developments in cryoET have resulted in visualization of the NPC structure with unprecedented details^{48,49,50}. The basic framework of the NPC structure includes three rings, the inner ring, the nuclear ring and the cytoplasmic ring. The inner ring lies at the juncture of the outer and inner nuclear membrane and anchors the nuclear and cytoplasmic rings towards the nuclear and

cytoplasmic sides respectively. The nuclear and the cytoplasmic rings bear extensions known as the cytoplasmic filaments and the nuclear basket respectively. The NPC structure is formed by 30 different proteins known as nucleoporins (Nups) which are present in multiple copies; the copy numbers in numerous cases being a multiple of 8^{48,49}. A striking feature of all cryo-EM maps of the NPC is a big central hole (~27 nm in diameter at the narrowest for the human NPC), which might mislead one to think that the NPC really constitutes a hole in the nuclear envelope allowing molecular exchange. In reality the apparent hole is filled with a very high density of IDPs. About 1/3 of Nups bear IDP extensions and are known as FG Nucleoporins (FGNups)^{51,52}. These disordered FGNups extend from the NPC scaffold structure and form the permeability barrier of the NPC.

The nucleocytoplasmic transport is a highly regulated process; the regulation being important for maintenance of cellular homeostasis. Key to the regulatory function of the NPC is the permeability barrier formed by disordered FGNups. The NPC acts as a size selective filter that allows free passage of cargoes below a size threshold of ~40kDa. Although recent studies suggest that the NPC might not have a sharp size based cutoff and rather constitutes a soft barrier towards passive diffusion that intensifies with cargo size⁵³. Thus, above a certain size threshold passive transport across the NPC becomes practically negligible and necessitates recognition of the cargo by molecules known as nuclear transport receptors (NTRs) which chaperone the molecule across the NPC. Interactions between the disordered FGNups and NTRs forms the basis of NTR aided nucleocytoplasmic transport of cargoes⁵⁴.

While the translocation across the permeability barrier of the NPC does not require energy the directionality of export or import across the NPC is maintained by a RanGTP/GDP gradient formed across the NPC⁵⁴. Ran is a small GTPase; RanGTP is in excess on the nuclear side and RanGDP is in excess on the cytoplasmic side. The NTRs depending on whether they are involved in import (importins) or export (exportins) are differentially regulated by RanGTP and this governs the directionality of the transport. Nucleocytoplasmic transport involves three key steps, which are recognition of the cargo by NTR, translocation of the NTR/cargo complex across the permeability barrier and release of the cargo from the NTR on either the nuclear or the cytoplasmic side. For nuclear import, importins bind cargo bearing nuclear localization signals (NLSs) and the importin-cargo complex is shuttled across the NPC; at the nuclear side RanGTP binds the importin-cargo complex disassociating the cargo from importin⁵⁴. Export happens in a similar fashion where RanGTP bound exportins bind cargoes bearing nuclear export signals (NESs), and the exportin-cargo complex is shuttled across the NPC; at the cytoplasmic side GTP hydrolysis reduces the affinity of exportin towards the cargo leading to cargo release. The RanGTP/GDP gradient is maintained by differential spatial localization of the elements that govern the Ran cycle. NTF2 which is an NTR shuttles RanGDP to the nucleus where RanGEF catalyzes exchange of GTP for GDP producing RanGTP which disassociates from NTF2. This RanGTP can then traverse across the NPC bound to exportin-cargo complexes and in the

cytoplasm the RanGAP activates GTPase activity of Ran converting RanGTP to RanGDP which has minimal affinity for exportin and hence the RanGDP-exportin-cargo complex disassociates releasing RanGDP⁵⁴.

1.2.2 FGNups

FGNups consist of a structured domain that anchors into the scaffold of the NPC and a disordered domain, known as the FG domain, that bears several phenylalanine-glycine (FG) motifs and hence the name FGNups/FG domain⁵¹. FG motifs often have certain adjacent residues and thus can be classified such as PxFG, FxFG, GLFG and SAFG (See Fig1.5)^{55,56,57,58,59}. FG motifs are known to interact with NTRs; however, whether the different FG motifs have distinct functions is yet not clearly known. This is further compounded by the fact that several FGNups are highly redundant with respect to NPC function which is very robust, thus deletion studies provide limited insight^{52,60}. Sequence homology between FG domains is very limited across species owing to a high amino acid substitution rate which happens to be idiosyncratic of IDPs⁶¹. However, careful analysis have revealed small islands of sequences 6-11 residues long surrounding some FG motifs, which are thought to be important for engaging NTRs, show preservation⁶¹. Another characteristic feature of the FG domains is their position in the sequence space. The position of FG domains in sequence space deviates from that occupied by typical IDPs, and this is a feature which applies to all FG domains from diverse species despite low sequence conservation amongst them. FG domains can sometimes be as hydrophobic as folded globular domains and almost always have much low mean net charge which is not akin to typical IDPs^{45,62}. Whether functional necessity gave rise to a bespoke sequence space for FG domains is an interesting question.

It is now widely accepted that basis of size selectivity of the permeability barrier in the NPC is based on the FG motifs centered hydrophobic interactions of FG domains and interaction of FG domains and with the NTRs. There are several evidences to support this line of thought. Surface hydrophobicity of a cargo is known to be drastically related to its ability of crossing the NPC. Naim et al. demonstrated this in a beautiful experiment; a cargo which was unable to traverse the NPC by itself upon decoration with surface hydrophobic groups ceaselessly passed the NPC with rates comparable to NTR mediated transport⁶³. In another elegant essay developed by Patel et al., weak cohesive interactions between FG domains could be detected by imaging accumulation of fluorescently tagged FG domains on beads coated with FG domains and such interactions were only prominent for FG domains that constituted the central channel of the NPC⁵². Another key evidence is the fact that the permeability barrier of the NPC can easily be breached by hexanediol, a hydrophobic alcohol, reinforcing the theme that hydrophobic interactions are key to functioning of the permeability barrier⁶⁴.

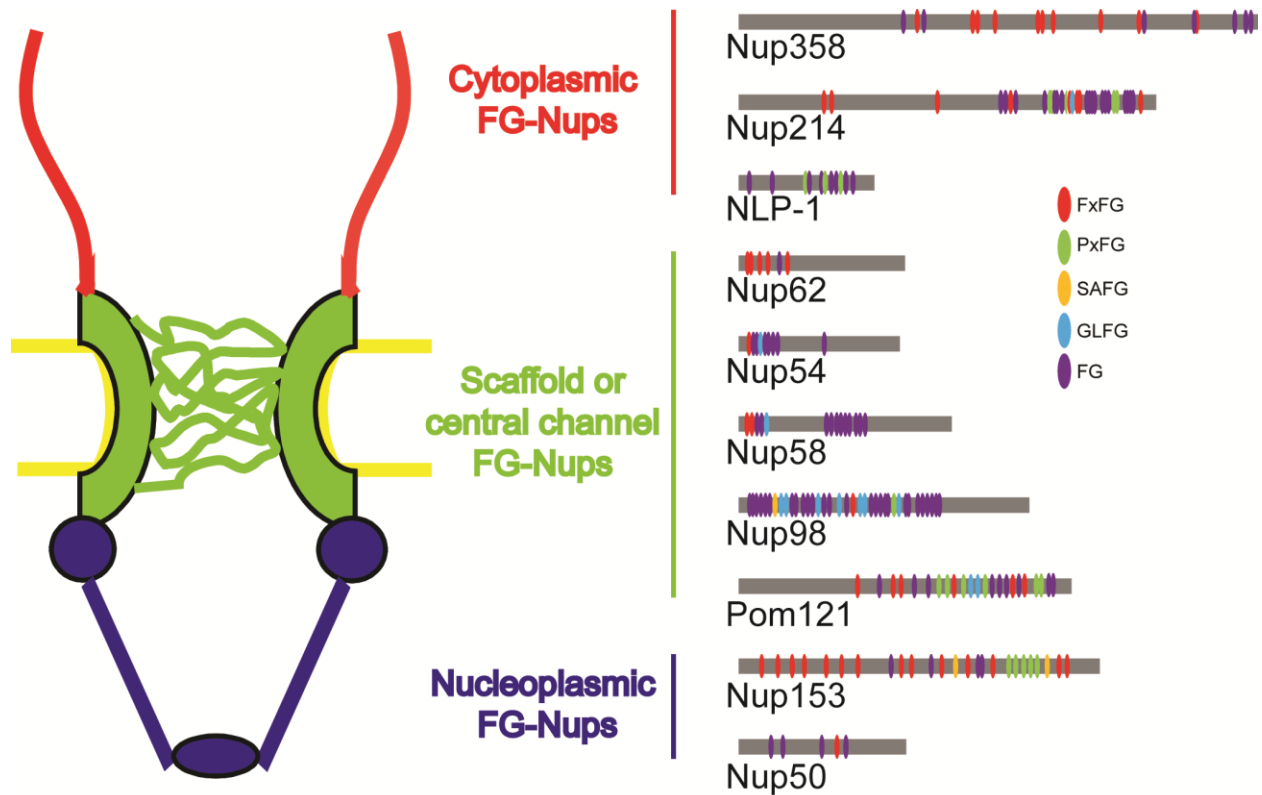


Figure 1.5 Schematic of the human NPC showing constituent FG-Nups: The different FG-Nups are segregated depending on their spatial location in the NPC. The corresponding FG domains are shown schematically with the different FG motifs color coded.

While the cohesive nature, that is the propensity for favourable self interaction, of some FG domains has been experimentally established, the exact nature of organization of FG domains in the NPC is a topic that is controversial and the subject of intense debate. It has been demonstrated that some FG domains like Nup100 in yeast are more collapsed, that is the ensemble is populated by more compact structures than others, based on a gel permeation chromatography assay⁶⁵. Later advanced single molecule FRET (smFRET) assays that directly probe collapse showed fragments of Nup98 FG domain, which is the human homologue of Nup100 in yeast, to be substantially more collapsed than FG domain fragments from other human FG-Nups like Nup153⁶⁶. Such cohesive FG domains have been shown to form hydrogels and these hydrogels recapitulate the essential functionalities of the NPC such as exclusion of large cargoes and rapid and selective import of NTR bound cargoes^{67,68}. This has led to the hypothesis that such hydrogels constitute the permeability barrier. Such hypothesis can collectively be seen as ‘barrier centric’ model of the NPC that emphasizes the role of FG-Nup forming a selective phase that acts as a barrier and can only be traversed by NTRs. Contrary to such view is a ‘NTR centric’ view of the transport. ‘NTR centric’ view takes into account the active role of formation of the permeability barrier itself and also takes into account the fact that the FG domains are anchored to a surface in the NPC. This line of thought primarily originated

from the experiments performed on FG domains grafted on the surface in a study by Lim et al⁶⁹. FG domains grafted on a surface shows behavior akin to polymeric brush which can be reversibly collapsed by NTRs⁶⁹. Such collapsed polymeric brush layers present a size dependent entropic barrier to cargo passage. The idea of ‘NTR centric’ control can be further extended taking into account that in the cell NTRs are always present and are high affinity binders of the FG domains. Thus, in principle the permeability barrier of the NPC can consist of a collapsed polymer brush coated with NTRs that lines the scaffold of the NPC and acts as an entropic barrier to external cargoes hindering their passage as their size increases; and this architecture allows 2D dimensional ‘skating’ of NTR bound cargo along this collapsed polymer brush coated with NTRs allowing fast NTR mediated transport across the NPC⁷⁰. It should however be noted that the behaviour of surface tethered FG domains toward NTR is disputed in literature; contrary to the study by Lim et al.⁶⁹ other studies have not found any collapse of a layer of surface tethered FG domains upon interaction with NTRs^{71,72}. One also has to keep in mind that the disordered FG domains owing to their disorder display behavior akin to polymeric coils. Scaling properties of various FG domain/FG domain fragments based on smFRET assays typically show a scaling exponent of ≥ 0.5 ⁶⁶ suggesting collapsed behavior to be a general feature of all FG domains irrespective of whether they are cohesive or not. Since collapsed behaviour can only originate from cohesivity, that is propensity of self-interaction, it can be said in other words that all FG domains are cohesive to some extent from a polymer physics standpoint; with FG domains traditionally defined as cohesive based on different assays (such as the bead binding assay by Patel et al.⁵² or hydrogel formation assays⁶⁸) being just more collapsed than other ones. Collapsed IDPs engender behavior and dynamics characteristic of self-associating polymers and thus are expected to undergo liquid-liquid phase separation. Indeed FG domains have shown to undergo phase separation, producing phases that are selectively permeable to NTR bound cargoes and exclude inert cargoes⁶². Also a recent study provided a comprehensive mathematical model, based on polymer like behavior of FG domains and their collapse, phase separation and NTR binding, that recapitulated at the phenomenological level most of the experimental observations made on FG domains so far and suggested that both 'brush-like' and ‘hydrogel-like’ effects cooperate in dictating the structure of FG domains in presence of NTRs and thus these two opposing views do not need to be mutually exclusive⁷³.

In summary, controversies remain about the spatial organization of the FG domain in the NPC and the exact physical nature of the permeability barrier they constitute. However, what is unambiguously established is that the FG domains are essential for the selective permeability of the NPC and FG domain/NTR interaction is necessary for traversing the NPC by NTR bound cargoes.

1.2.3 Nuclear transport receptors

The NTRs execute translocation of cargoes across the NPC by their ability to recognize

localization signals, NESs or NLSs on a specific cargo and to traverse the permeability barrier via interaction with FG domains. A common structural feature of most NTRs are three fold; they have structural elements that can bind FG motifs, they can bind Ran allowing Ran binding induced allosteric regulation and most of them can recognize NESs or NLSs. β -karyopherin/Importin β superfamily is the largest family of NTRs consisting of about 20 NTRs⁷⁴. This superfamily is characterized by very high structural similarity with nominal sequence similarity⁷⁵. The most common structural feature of members from this family is the fact they are constituted by several stacked HEAT repeats (see Figure 1.6)^{76,77,78}. HEAT repeats are structural elements formed by a helix-loop-helix motif where two amphipathic helices are arranged in an antiparallel orientation with the helix helix interface formed by the hydrophobic faces of both helices⁷⁶. β -karyopherin/Importin β members are both importins like Importin β and exportins like CRM1 and CAS. The heat repeat interfaces typically provide hydrophobic clefts and thus binding spots for the FG motifs.

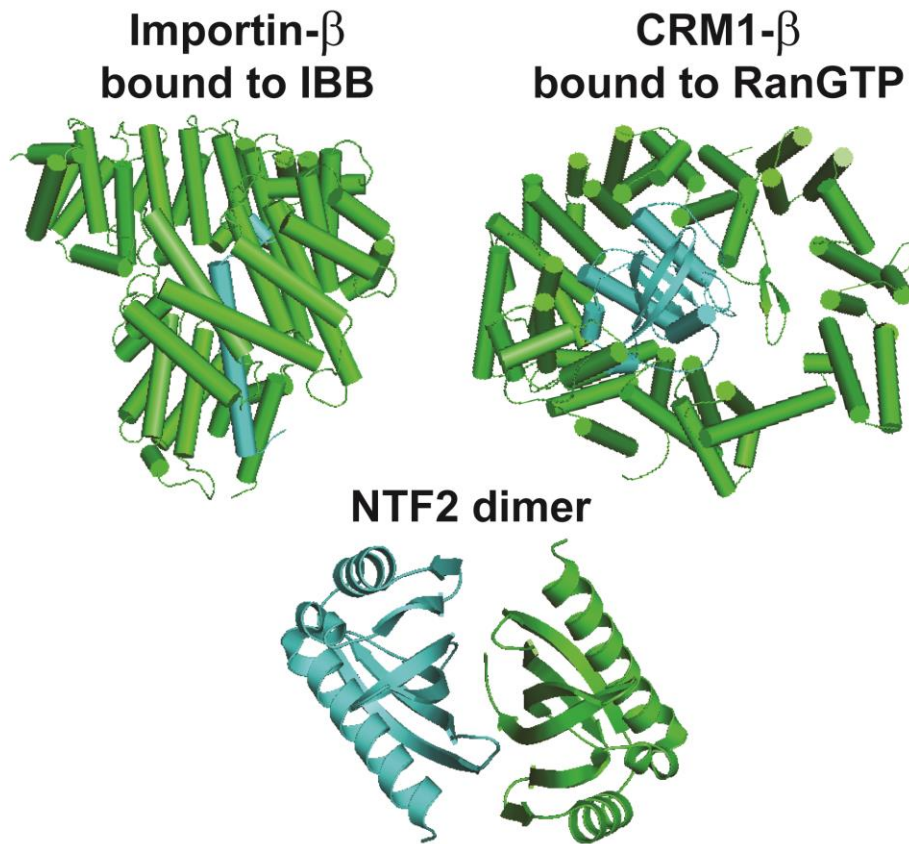


Figure 1.6 Structures of different NTRs: Crystal structure (PDB:1QGK) of Importin β (shown in green with all the helices of the HEAT repeats shown as cylinders) bound to IBB domain of Importin α (shown as cylinder in cyan), (top left). Crystal structure of CRM1 (3NC1) shown in green with all the helices of the HEAT repeats shown as cylinders bound to RanGTP shown as cyan (top right). Crystal structure of NTF2 homo-dimer (PDB:1OUN) with one subunit in green and the other in cyan (bottom).

The HEAT repeats attribute a large amount of dynamic flexibility to the transporters due to which they can adopt several conformers such as superhelical, torroidal and globular^{79,80}. The HEAT repeats also allow the NTRs to adopt a conformation depending on the external environment; for example it was shown with a FRET assay that the extension of Importin β is dependent on the solvent hydrophobicity and more compact conformations were populated in hydrophobic environments⁸¹. Such environment sensitive behavior has biological implications, in the hydrophobic environment of the permeability barrier of the NPC a more compact NTR structure may have functional relevance. These NTRs bind RanGTP with a conformational change that allows allosteric control. For the classical NLS Importin- β RanGTP binding causes disassociation of the NLS bearing cargo-bound Importin α ⁷⁷ while for the exportin CRM1 RanGTP binding increases affinity for cargo bearing NESs⁷⁸; in both these cases RanGTP binding is however supposed to involve similar structural changes causing rather expanded unbound states of Importin β and CRM1.

NTRs can also have architectures that are without HEAT repeats. For example NTF2, the RanGDP transporter, is devoid of HEAT repeats but is composed of a bent β -sheet and three helices and the native protein is a homodimer formed by a β -sheet interface (see Fig 1.6)⁸². The NTF2 domain architecture is also used in other NTRs. For example the NXF1:NXT1 complex also known as the TAP:p15 complex is a general mRNA exportin where each of NXT1 and NXF1 possesses a NTF2 like domain which forms a heterodimeric structure in the complex, resembling the NTF2 homodimer, which can bind FG motifs and subsequently traverse the NPC⁸³.

The discussion above highlights the primary fact that while NTRs might employ different structural architectures a key functionality of all NTRs is that they can traverse the permeability barrier of the NPC and interact with the FG domains. In the following sections this interaction is described in greater details.

1.2.4 Dynamics of interaction of NTRs with FG Nups; towards deciphering the transport paradox

The interaction of FG domains with NTRs forms a foundation of current NPC biology. Numerous permeabilized cell assays have demonstrated the need for different NTRs to mediate cargo transport; when cytosolic contents are washed away post permeabilization nuclear transport comes to a halt but can be ceaselessly brought back to life by externally adding NTRs and Ran clearly demonstrating that these cytosolic components are indispensable for transport^{84,85,57}. In addition, several *in vitro* assays have demonstrated binding between different FG domains and NTRs. Moreover mutants of NTRs such as Importin- β or NTF2 that have diminished affinity for FG domains also demonstrate reduced cargo transport or localization at the NPC^{86,87,88,89,82}. These biochemical studies have also been supplemented by structural biology studies. Importin β

fragment crystallized with a fragment of the FG domain of Nsp1 bearing 5 FxFG motifs clearly showed two FG binding motifs on Importin β formed by hydrophobic pockets (See Fig 1.7) and these sites were shown to be conserved in a structure of Importin β crystallised with a GLFG peptide⁹⁰. Similarly, NTF2 was also crystallized with a short FxFG peptide which was shown to bind the hydrophobic groove formed by the dimeric interface by NTF2 (Fig 1.7)⁸². More FG motif binding sites were detected for Importin β and NTF2 via molecular dynamics (MD) simulations^{91,92}. Also the FG binding sites in Importin β were shown to be modulated by Ran binding using single molecule force spectroscopy which is in line with a structural study that showed RanGTP binding misplaces the binding site in Importin β from its original position⁹³.

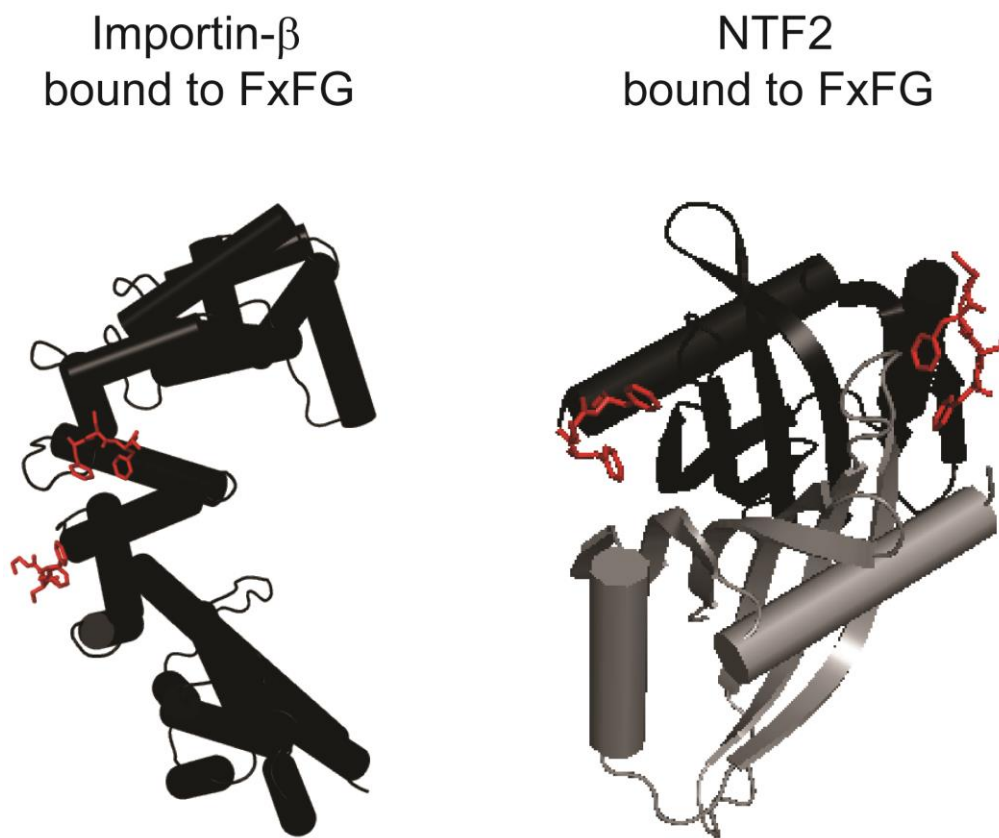


Figure 1.7 Structures of different NTRs complexed with FG motifs: Crystal structure (PDB:1F59) of Importin β (1-442 aa) (black) bound to a FxFG motifs (red) of Nsp1p peptide composed of 5 FxFG repeats (left). Crystal structure (PDB:1GYB) of a homo-dimer of NTF2 (one subunit in grey and the other in black) bound to an FxFG peptide, where the motifs bind two hydrophobic pockets at the dimeric interface (right).

Several studies have employed single particle tracking assays and tracked the translocation of single fluorescent cargoes across the NPC revealing that the typical transit times of variously sized cargoes are only a few millisecond^{94,95,96,97}. Thus, the transport process is extremely fast. The transport process is also extremely selective based on highly specific recognition of FG

domains by NTRs. From a biochemical standpoint ‘fast’ and ‘selective’ are two concepts that do not occur simultaneously as selectivity is manifested through high affinity binding and consequently long lived complexes and contrastingly fast processes typically involve low affinity interactions with short lived complexes. The discrepancy between ‘fast’ and ‘selective’ in the context of nucleocytoplasmic transport becomes much more apparent when we start putting realistic numbers. The affinity between FG domains and NTRs has been measured to be within micromolar to nanomolar range^{98,99,100,101}. The concentration of FG, GF and F motifs combined is ~250 mM considering the dimensions of the pore and sequence and copy numbers of FG domains¹⁰². Now, if we consider the typical disassociation constant (K_D) between a generic FG domain and a NTR as 1 μ M and the association rate constant (k_{on}) at $\sim 10^7$ $M^{-1}s^{-1}$ which is the typical upper limit of fast protein-protein interactions that are not dominated by electrostatics, one can calculate the upper limit of the disassociation rate constant (k_{off}), which is the product of K_D and k_{on} , and subsequently the disassociation half-life of the complex. Using these values one can get an upper bound on ($t_{1/2}$) the disassociation half-life of the complex (where $t_{1/2} = \ln 2/k_{off}$) which comes out at ~70ms. This value is an order of magnitude larger than the transit times of typical cargoes.

Considering that during translocation through the NPC, NTRs interact with several FG domains and can have submicromolar affinities, the actual discrepancy can be even larger. This apparent discrepancy between the timescales of transit across the NPC and that of the lifetime of a stable complex constitutes what is known as the ‘transport paradox’. The key to deciphering this transport paradox lies in understanding the binding mechanism of FG domains with NTRs which is discussed below.

Motivated by understanding the transport paradox our lab initiated a multi-disciplinary approach involving single molecule spectroscopy, stopped-flow kinetic measurements, MD simulations and NMR experiments to understand the details of the dynamics of interaction between FG domains and NTRs²⁵.

smFRET experiments that probe the distances between two points in an IDP, were performed on several FG domains in presence and absence of several NTRs. The smFRET experiment revealed a striking feature about the interaction of FG domains and NTRs; the FG domains showed no change in FRET efficiency, which served as a proxy for conformational change, when binding NTR²⁵. This observation clearly demonstrates the role of multivalency in the interaction as binding without conformational change could possibly happen only if the disordered IDP bears several binding motifs in the form of FG motifs that can bind several binding spots on an NTR such that every pose in the unbound conformational ensemble of the FG domain presents some binding competent motifs. Such an interaction is principally similar to that of a classical fuzzy complex, like Sic1-Cdc4 where multiphosphorylated disordered Sic1 participates in a multivalent interaction with Cdc4 without undergoing any conformation change, where each

phosphorylated Sic1 site constitutes a binding motif and can bind Cdc4²⁶. These observations thus point towards fuzzy complex formation as the mechanism behind FG domain and NTR interaction as the IDP do not undergo any conformational change upon partner binding. It should be noted that lack of conformational change is not a criterion for fuzzy complex formation, lack of a folding transition is; thus, a conformational change may or may not be associated with a folding transition but a lack of conformational change certainly excludes a folding transition. In fact at concentrations much higher than that used in smFRET assays, a recent study showed extension of the FGNup upon NTR binding in a concentration dependent way suggesting that despite being fuzzy the interaction between NTRs and FGNups in certain special conditions can also involve conformational change¹⁰³. To understand more about the dynamics of the interaction association rate constants or k_{on} were measured between several FG domains and NTRs using stopped-flow kinetics²⁵. The association rate constants were found to be in the order of $10^9 \text{ M}^{-1} \text{ s}^{-1}$ which essentially happened to be the diffusion limited rate constants indicating that every encounter between the FG domains and NTRs led to a complex formation²⁵. Such high k_{on} values are only known for systems where the binding is dominated by electrostatic attraction¹⁰⁴ which however was clearly not the case for FGNups and NTR interaction as was evidenced by very low dependence of k_{ons} on ionic strength, unlike complexes driven by electrostatics. Finally, NMR studies done with a short FGNup fragment showed the direct experimental evidence about the role of F residues in the binding and the effect of multivalency. NMR data demonstrated that the FGNup fragment remained disordered in both presence and absence of NTRs with only the F residues showing largest perturbations upon NTR binding²⁵. Also, since NMR provides residue specific information the affinities for the different individual F residues for the NTR Importin β were obtained and found to be in millimolar range. In a construct devoid of all F residues but one there was a decreased affinity of that particular F residue for the NTR compared to the wild type construct showing a clear effect of the multivalency²⁵ in the interaction. This result was qualitatively consistent with a similar NMR study of FGNup-NTR interaction¹⁰⁵.

The mentioned experiments were further augmented by MD and brownian dynamics (BD) simulations to gain molecular insight in to this interaction²⁵. The simulations showed F residues despite being hydrophobic have exposed side chains rendering a highly reactive surface to the FG domains, and this results in ultrafast binding as was confirmed by BD simulations yielding a near exact match between BD and stopped-flow obtained k_{on} values and their minimal dependence on electrostatic effects²⁵. BD simulations also suggested apolar desolvation to be the driving force for the binding suggesting a key role of water in the interaction.

Based on the experimental and computational studies of the FG domain and NTR interaction mentioned above, a general picture of this interaction can be drawn which also helps to clarify the transport paradox. The currently accepted idea, as was proposed by our group and other studies that reached a similar qualitative conclusion¹⁰⁵, is that a FG domains presents exposed F residues that render the FG domain highly reactive towards a NTR leading to a fuzzy complex

formation where the FG domain binds the NTR with diffusion limited rate constants without undergoing any folding transition and for most conditions any major conformational change; the overall affinity of the complex is high owing to the presence of multiple binding motifs. However, individual FG motifs have very low affinities and are thus in a dynamic equilibrium binding and unbinding different NTR sites. With this picture in mind, the transport paradox can be explained very nicely as well. Firstly, if we just consider a k_{on} of $10^9 \text{ M}^{-1} \text{ s}^{-1}$ the disassociation half-life of the complex that we previously calculated becomes 0.7 ms from 70 ms, which is already comparable or shorter than typical transport times of cargoes.

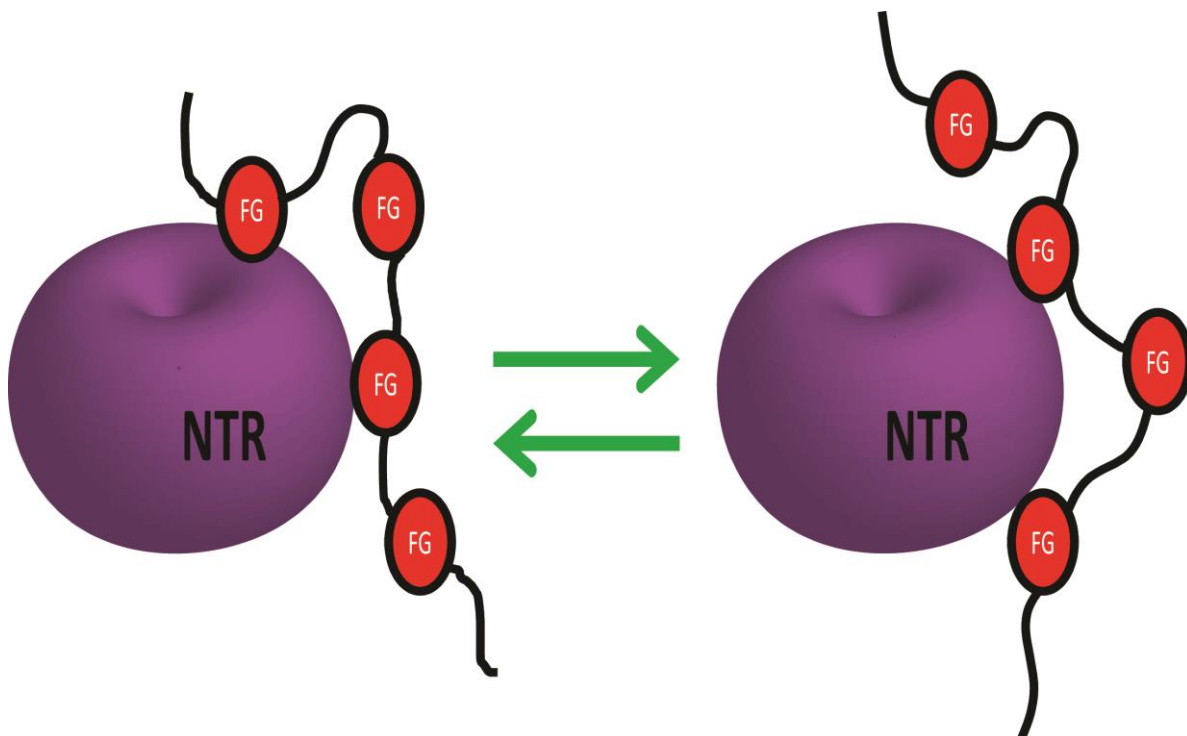


Figure 1.8 Schematic representation of FG domain NTR interaction: A fuzzy complex is formed between FG domains and NTRs where multivalent FG motifs interact with the NTRs. The individual motifs have low affinity and thus are in a dynamic equilibrium between bound and unbound form. The overall affinity of the complex is high due to the multivalency of the interaction despite low affinity of the individual motifs.

Further replacing the affinity values with that of 1 mM which is affinity of individual sites the half-life of individual sites bound on the NTR is around 700 ns which is ~ 4 orders of magnitude faster than typical transport times suggesting that many possible binding and unbinding event between FG motifs and NTRs can take place while the cargo transits the NPC. This view has been further substantiated by a computational study that proposes a ‘slide and exchange’ mechanism based on a very long MD simulation trajectory where one FG motif on the FG domain of NSP1 kicks out an FG motif prebound to the NTR NTF2 in nanosecond timescales, allowing a visualization of how NTRs can rapidly interact with multiple FG domains in the

NPC¹⁰⁶. The other aspect that came out from this study is reduction of dimensionality during such a slide and exchange mechanism where the search for a binding site on the NTR by a FG motif on FG domain essentially becomes a 2D search vs a 3D search when the FG domain is already anchored to the NTR via a different FG motif. This greatly accelerates the process.

In summary, FG domains interacts with NTRs with ultrafast kinetics forming fuzzy complexes where the affinity of the complex is high due to the multivalent nature of the interaction but individual binding motifs have low affinity allowing rapid exchange of motifs at a given binding site and this process allows for NTR mediated fast and selective nucleocytoplasmic transport.

1.3 Water in bio-molecular recognition

1.3.1 Water is universal necessity for life

Historically the role of water in supporting life is well known; the renowned renaissance polymath Leonardo Da Vinci described water as ‘vetturale di natura’ which essentially means that ‘water is the vehicle of nature’. And in the modern era of space exploration the search of extra-terrestrial life is often centered on the search for mobile water in extra-terrestrial celestial objects. Most living beings are composed of ~70% by weight of water and thus all the process needed to support life as we know it occurs in water.

The concentration of pure water in liquid state is 55.5 M under standard temperature and pressure. While in the crowded environment of a living cell water concentration can be lower it is still by far the most concentrated molecular species with concentrations 3-6 orders of magnitude more than any other biomolecule which typically have micromolar to millimolar concentrations. Thus, water often plays a crucial role in mediating all biochemical processes, owing to several unique properties of water as a solvent. Water participates in hydrogen bonding (H-bonding) very extensively, and thus allows log range communication between two water molecules via H-bonded network¹⁰⁷. This H-bonding allows water to act as a facile solvent for several molecules where water can readily solvate them by H-bonding with H-bond donor or acceptor groups on the molecule. This also means that water can directly H-bond with many protein residue side chains often acting as side chain extensions. This ability also allows water to stabilize several high energy intermediates by hydrogen bonding formed during enzyme catalysis pathways and thus increase enzymatic efficiency¹⁰⁸. Water can simultaneously act as hydroxyl and proton donor and can thus participate in acid-base catalysis type of reactions and activate functional groups for reactions¹⁰⁹. Water often directly participates in several biochemical processes; such as all hydrolytic reactions where hydrolase enzymes such as peptidases, amylases and lipases catalyze hydrolysis of peptides, saccharides and lipids respectively. Water is also used for carbon fixation in plants during photosynthesis. Another key mechanism by

which water molecules mediate biological processes is known as the hydrophobic effect. This effect is due to the fact that water is a highly polar solvent and thus hydrophobic molecules in water tend to aggregate preferring self solvation than aqueous solvation. This effect largely governs several molecular recognition processes where a relatively hydrophobic biomolecule binds a hydrophobic spot, where water is excluded from the solvation shells of both these molecules forming a hydrophobic interface and the process is both entropically and enthalpically favourable due to the release of a large number of water molecules and maximization of hydrophobic contacts respectively. (See Fig 1.9)¹¹⁰. The same effect is also thought to be the first step of protein folding, where the polypeptide chain for which water is a bad solvent undergoes a collapse transition which is entropically favorable owing to release of several water molecules¹¹¹.

In summary, water owing to its diverse physiochemical properties plays a crucial role in biology by directly participating and mediating almost all biological processes.

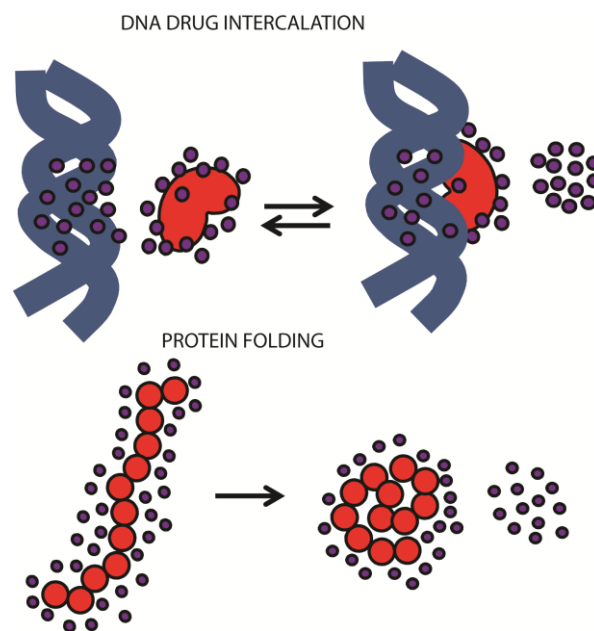


Figure 1.9 Schematic representation of the role of hydrophobic effect in biology: As a drug molecule intercalates with DNA release of water from both the DNA and drug entropically favors the interaction (top, adopted from [110]). A polypeptide chain adopts a collapsed conformation which is entropically favorable due to release of solvation water.

1.3.2 Approaches to measure water dynamics

Biology is inherently dynamic and thus to understand interactions of biomolecules with water and with other molecules mediated by water one must experimentally study the dynamics of water itself and its perturbation in biological milieus. Broadly, approaches to study solvation

dynamics can be categorized into techniques that measure a) average water dynamics of all water molecules within the geometric confines of an assembly or b) the collective response of all the water molecules or c) the collective response of all the water molecules from the perspective of a local probe¹¹² (See Fig 1.10).

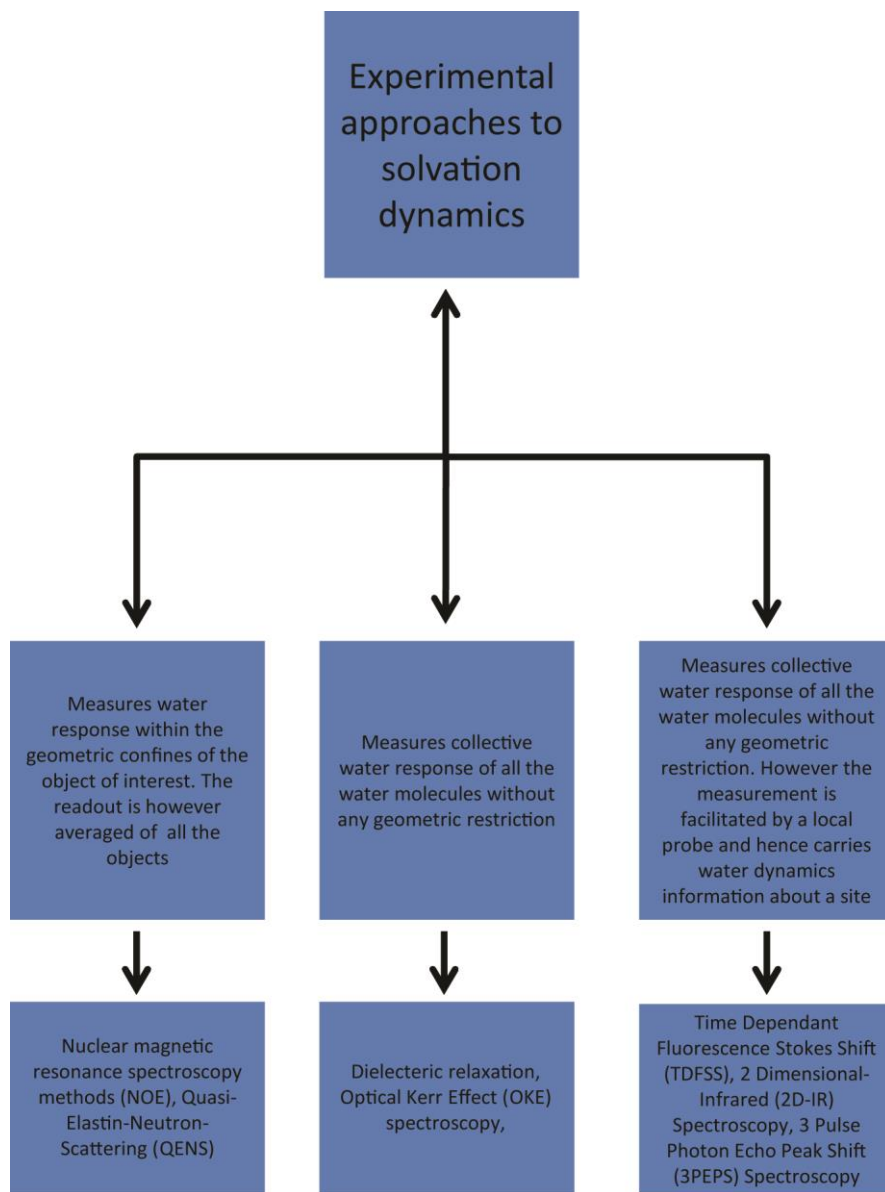


Figure 1.10 Schematic representation showing different approaches to measure solvation dynamics: Based on [112]. The schematic shows that water dynamics can be measured in three key forms; within the geometric confines on an assembly, of all the water molecules and of all the water molecules from the perspective of local probe. The techniques that can be used are also depicted.

Thus, these techniques are sensitive to water dynamics over varying length and time scales and report on different aspects of solvation dynamics. NMR and quasi-elastic neutron scattering (QENS) report on the dynamics of water within the confines of the hydration layer of an assembly, however the data involves averaging of all the water molecules and hence any site specific information is not obtainable from these approaches. On the contrary, dielectric relaxation and Optical Kerr Effect (OKE) spectroscopy measure response from all the water molecules and thus is only sensitive for large scale perturbations of overall solvent response achieved by rather high solute concentration. The 3rd category involves techniques such as 2D-IR, 3PEPS and TDFSS spectroscopy which measure overall solvent response from all the water molecules like in OKE spectroscopy or dielectric relaxation spectroscopy albeit with a key difference; the measurement is from the perspective of a local probe thus allowing site-specific studies of dynamics in an assembly. Since biological functionality is often encoded through site specific dynamic attributes the third category of techniques is most valuable for studying water dynamics in the context of biological functionality. 2D-IR spectroscopy is limited by the range of dynamics accessible which is only upto a few tens of picoseconds; this is because the vibrational lifetimes of most probes are a few tens of picoseconds¹¹³ and hence the technique is incapable of accessing slower dynamics often encountered in biological systems. 3PEPS and TDFSS are somewhat related and can access dynamics from femtosecond to nanosecond; however TDFSS is more popular for studying solvation dynamics in biological assemblies. In my PhD work the technique I used is TDFSS and describe it in more details in the following section.

1.3.3 Principles of TDFSS

TDFSS has been extensively used to probe solvation dynamics and involves measuring the time dependent emission frequency shift of a solute probe dye after instantaneous alteration of its charge distribution via optical excitation¹¹⁴. For this purpose a dye molecule is used where there is a large change in dipole moment in the excited state typically facilitated via a photo induced intramolecular charge transfer (ICT). The physics of the process is depicted in Figure 1.11 and is described in the following paragraph.

An ICT probe in the ground state is in equilibrium with the surrounding solvent molecules that are oriented stabilizing the ground state charge distribution of the probe. Now upon optical excitation, which causes a Frank-Condon transition, there is a change in dipole moment and charge distribution of the probe, instantaneously. However, the solvent molecules still retain their configuration and position that they had when in equilibrium with the ground state of the probe, and this leads to a highly non-equilibrium situation as the energy of this system is higher than the minimum potential energy of the probe-solvent system with the probe in the excited state. Subsequently the solvent molecules respond to the altered charge distribution of the probe and reorient to stabilize the excited state of the probe. This stabilization by the solvent is reflected in a continuous red shift of the probes

emission spectrum and the time dependence of this process directly reflects the time dependence of solvation. Thus by following this continuous frequency shift of the emission as a function of time one basically monitors the solvation dynamics. Experimental approaches to perform TDFSS are described in later sections.

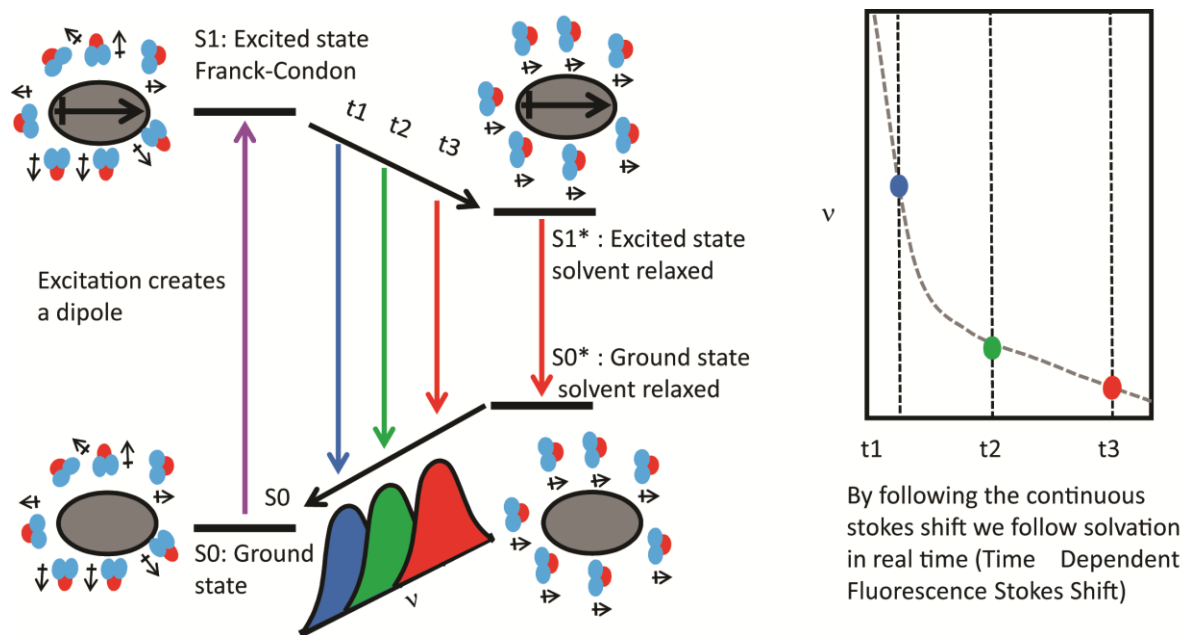


Figure 1.11 Principle of TDFSS measurements: Schematic of the process of solvation dynamics of a probe is shown on the left. Optical excitation from ground (S0) state creates instantaneously a dipole moment formation in excited Frank-Condon state of the probe (S1-Frank-Condon). The solvent molecules respond to this change via reorienting to stabilize the excited state charge distribution finally reaching a stabilized excited state (S1*). During this process of stabilization the emission spectrum undergoes a constant frequency shift as showed at three different time points t1, t2 and t3. On right is a schematic of the time dependence of the frequency shift for such a system as a function of time also showing the three specific time points described t1,t2 and t3 shown in the scheme on the left.

1.3.4 Dynamics of water in bulk and in biological matrices

The timescales involved in the response of a liquid solvent to a perturbation in an entity that is solvated by the liquid play a key role in reaction rates of chemical processes^{115,116,117}. For example if the solvent does not respond fast enough and cannot keep up with the progress of a particular reaction as the molecule proceeds to the transition state, rate of a reaction may be slowed down. Water has the fastest solvent response among all known solvents. Several

experiments and simulations have shown that solvation dynamics in water occurs with major sub-picosecond component and is complete within 2 ps^{118,119}.

The ultrafast dynamics of water is very well characterized now from both a theoretical and experimental perspective. However, the dynamic behavior of water changes dramatically and it is very heterogeneous on the surface of a biomolecule and is typically dynamically retarded by one to three orders of magnitude on different biomolecule surfaces such as DNA, lipids and proteins, presenting different types of surface properties and geometries^{120,121}. This has led to the coinage of the term ‘biological water’ to describe the distinct dynamical features of water at the interface of biomolecules¹²².

Solvation dynamics measurements with nucleoside analogues¹²³ and minor groove binders¹²⁴ in DNA have shown power law type of relaxation behavior which suggests intimate coupling of the water and biomolecule dynamics; for a T-T mismatch such power law relaxation occurred with a different exponent compared to regular dsDNA suggesting the importance of such dynamics in molecular recognition¹²⁵.

Solvation at the interface of lipid or lipid like environments such as micelles or vesicles has been studied extensively as well¹²⁰. Studies using femtosecond fluorescence up-conversion spectroscopy¹²⁶ and photon echo spectroscopy¹²⁷ have shown acute slowing down of solvation dynamics in aqueous lipid bilayer. The altered dynamical properties of water in membrane structures have been shown to be largely membrane depth¹²⁸ dependent; with progressive slowing down of water dynamics as one move deeper into the bilayer from the water bilayer interface. Such depth dependent behavior can have a huge biological impact for systems such as transmembrane domains of proteins where the transmembrane domain would experience this depth dependent dynamics^{129,130}.

Of all the bio-molecules solvation protein surfaces have been studied the most extensively. First indications of slow protein solvation dynamics came from dielectric relaxation experiments where compared to free water, which showed a relaxation component ~10 ps, a myoglobin solution showed additional slower relaxation times of 200 ps which was attributed to slow surface water dynamics¹³¹. Further solvent retardation on protein surfaces have been seen via various techniques. Kurt Wurtrich’s group have reported the time scales of water dynamics on protein surface to be less than 300 ps¹³² while another NMR study suggested only 2-5 fold average slowdown of all the water¹³³ molecules that are on the protein surface compared to bulk water. Contrasting to these NMR studies a series of publications from Ahmed Zewail and Dong Ping Zhong’s group using ultrafast fluorescence spectroscopy and tryptophan as a local probe in several proteins placed in the context of different secondary structure elements and surrounded by different residues, had shown that the dynamics of solvation on protein surface occurred on two dominant timescales, one in <10 ps and another in 10s of picoseconds^{134,135,136,137,138,139,140}.

While when probing solvation dynamics the numbers obtained from different techniques may seem to be at odds with each other; such discrepancies can be explained taking on board the fact that different techniques probed different properties of water which were differentially modulated in presence of a biomolecular surface¹¹². Water dynamics have been widely implicated in biological recognition; for example water dynamics on protein surface measured locally on a polymerase active site forming an interface with DNA, showed limited retardation of water dynamics in presence of DNA for a fast polymerase¹⁴¹ and more acute water dynamics retardation for a slower polymerase¹⁴². The most striking example of such functional relevance of dynamics happens to be a case where solvation dynamics seems to defy even the ‘structure function’ paradigm; when the active site of an enantio-selective dehalogenase DbjA was transplanted into another dehalogenase scaffold leading to a new dehalogenase DhaA12 with identical active site structure but not the same enantioselectivity of DbjA, this was attributed to very different solvation dynamics at the active site of these two enzymes when probed using a fluorescent substrate analogue¹⁴³ (See Figure 1.12).

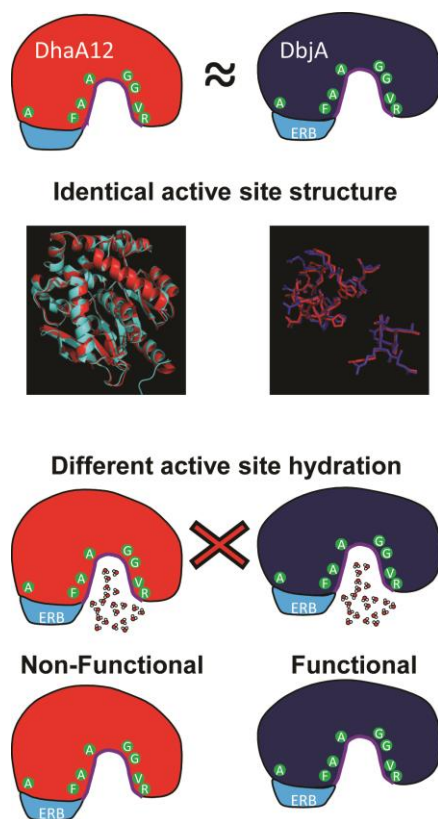


Figure 1.12 Schematic representation of the role of solvation dynamics on molecular recognition: The active site of an enantio-selective dehalogenase DbjA was transplanted into another dehalogenase scaffold leading to a new dehalogenase DhaA12 with identical active site structure. However, DhaA12 did not have the same enantioselective function of DbjA and this was attributed to very different solvation dynamics at the active site of these two enzymes (based on [143]).

Such cases of direct implication of solvation dynamics in molecular recognition can be understood in the light of the fact that recent experimental evidence suggests that dynamic motions of protein side chains are slave to solvent motions, based on the fact that timescales of solvent motion despite being always faster than local motions of side chains are always correlated^{144,145}. In a very recent study, Zhong group demonstrated same energy barriers for solvent motions and side chain motions albeit very different timescales for the two processes; time scales of solvation were always faster than side chain motions indicating that solvent fluctuations drive side chain motions and the two are intimately coupled¹⁴⁵.

In summary, the dynamics of water in bulk water is extremely fast; however, this dynamics is greatly attenuated on a bio-molecular surface leading to retardation of this dynamics. This altered water dynamics on bio-molecular surface has profound role in molecular recognition.

1.3.5 Solvation dynamics in IDPs

IDPs unlike folded proteins do not have stable structural elements to attenuate function and can thus solely depend on dynamics to execute molecular recognition. Thus, the role of solvation dynamics in such systems becomes magnified in comparison to folded proteins.

Despite the likely importance of solvation dynamics in IDP function, studies of solvation dynamics in IDPs have been rather few compared to folded proteins. A neutron scattering study demonstrated the extent of coupling between atomic motions and solvation dynamics for IDPs to be substantially more than that for folded proteins, providing experimental support for the conjecture that IDPs primarily use dynamics to execute molecular recognition¹⁴⁶. MD simulations have shown the nature of solvation water on IDPs to be different compared to folded proteins^{147,148}. It was also shown in a different study using ODNP (Overhauser Dynamic Nuclear Polarization) spectroscopy, facilitated by site specific spin probes, that the nature of solvation water on IDP surfaces are substantially less heterogeneous compared to folded proteins¹⁴⁹. Many IDPs such as tau, α -synuclein and A β are amyloidogenic and implicated in neurodegenerative diseases¹⁵⁰. Hence, the role of solvation dynamics in amyloid formation has also been investigated. It was shown using site selective ODNP spectroscopy that the earliest steps in induced tau fibrillation are related with changes in solvation dynamics and these changes precede fibril formation¹⁵¹. Another study using femtosecond fluorescence spectroscopy with dye labelled IDP κ -casein showed dramatic slowdown of solvation water in picosecond to nanosecond timescales in the fibril state compared to the native state¹⁵². Such slowdown of solvation in amyloid fibrils may have role in kinetic stabilization of the fibril and indicate entropically favorable release of mobile water from the IDP surface during transition to fibril form (See Figure 1.13).

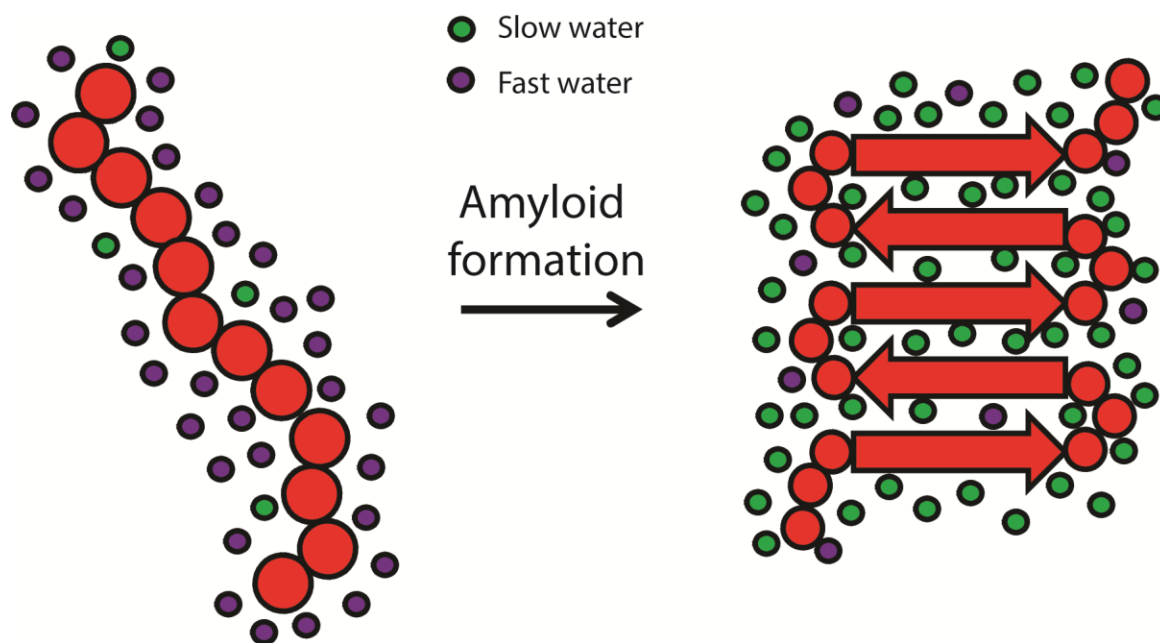


Figure 1.13 Schematic representation of water structural transition during amyloid formation: Dynamic and fast water molecules (represented in violet) primarily surrounds and IDP in solution (left) with few retarded and slow water molecules (represented in green), however, when the IDP undergoes a transition into an amyloid (right) the situation is reversed with slow water molecules primarily solvating the amyloid with few fast water molecules (based on [152]).

While the above mentioned studies underscore the potential role of solvation dynamics in the function and molecular recognition of IDPs, direct investigation of the role of solvation dynamics in IDP recognition has not yet been perused and remains a largely uncharted territory. During the course of my PhD studies my primary research focus has been the investigation of the role of solvation dynamics in molecular recognition of IDPs that engage partners using different binding mechanisms using IDPs that have a key role in nucleocytoplasmic transport to elucidate general biophysics of IDP interactions as well as how such biophysical principles might facilitate functionality in the context of nucleocytoplasmic transport.

To summarize, IDPs due to their lack of stable folded structural elements use predominantly dynamics to facilitate molecular recognition and thus the role of solvation dynamics is likely to be very important in IDP function and recognition.

Chapter 2

2 Objectives

The primary aim of my PhD can be divided under two broad headings: 1) investigate the relationship between solvation dynamics and IDP binding mechanisms, with a focus on IDPs involved in nucleocytoplasmic transport 2) understand all the timescales of solvation dynamics involved in IDP recognition for a model system. To realize my first objective I aim to see the extent of solvation dynamics modulation in IDPs when they bind their partners. IDPs bind their partners primarily via two mechanisms, coupled folding-binding and fuzzy complex formation. I will perform experiments on IDPs which are involved in nucleocytoplasmic transport and represent both the coupled folding-binding and fuzzy complex formation mechanisms. This should contribute to the understanding of nucleocytoplasmic transport process from a more molecular standpoint and also shed light on how IDPs exploit dynamic attributes, due to lack of structural elements, to facilitate molecular recognition. To realize my second objective I aim to perform femtosecond spectroscopy on a model IDP system so that I can access all the timescales involved. I also aim to investigate how the involved timescales are affected upon partner binding. My objective is delineated below as two broad aims (as mentioned above) with modular sub-objectives.

2.1 Relationship between solvation dynamics and IDP binding mechanism

2.1.1 Construction of a picosecond resolved TCSPC (Time Correlated Single Photon Counting) setup and establishment of solvation dynamics measurements using TDFSS

To measure solvation dynamics using TDFSS I aim to use picosecond resolved fluorescence spectroscopy. My aim is to build a picosecond resolved TCSPC setup and establish the procedure for TDFSS measurement.

2.1.2 Measurement of solvation dynamics in an IDP (IBB) that forms a complex via a coupled-folding mechanism (IBB-Importin β).

IBB undergoes a helix transition upon binding Importin β , the interaction involving a coupled folding-binding mechanism. I will investigate the solvation dynamics in free IBB and IBB in IBB-Importin β complex.

2.1.3 Measurement of solvation dynamics in FGNups that form a complex via a fuzzy binding mechanism (FGNup-Importin β).

FGNups form a fuzzy complex with Importin β . I will measure solvation dynamics in a model FGNup, Nup 153FG, at multiple sites that are heterogeneous in terms of sequence features, in the free state and in a fuzzy complex with Importin β . I will repeat similar measurements on NSP1FG, another model FGNup, to establish generality of the findings.

2.1.4 Comparison and rationalization of the extent of solvation dynamics modulation in IDPs upon complex formation using different mechanisms.

I aim to compare the measured modulation of solvent dynamics in IDPs upon complex formation for fuzzy and coupled folding-binding mechanisms, based on my results. I aim to rationalize the comparative result in the context of molecular aspects of the two mechanisms involved. I also aim to compare my results from TCSPC experiments with MD data from our collaborators, notwithstanding the challenges I might face due to the comparatively limited time resolution of TCSPC measurements.

2.2 Probing all the timescales of IDP recognition

2.2.1 Probing femtosecond resolved solvation dynamics for IBB recognition

I aim to perform femtosecond resolved solvation dynamics in IBB and IBB-importin β to characterize the entire time scale where solvation dynamics happen. This pursuit is mainly motivated by the limited time resolution of TCSPC measurements. Such high time resolution data may also yield more informative comparisons with MD data. I aim to shed some light on the ultrafast dynamics aspect of IDP recognition.

Chapter 3

3 Materials and methods

The materials and methods chapter is divided into two broad sections, methods and materials. In the methods section I provide protocols used for protein purifications and labelling, describe the equations and approaches used for the spectroscopic measurements (single molecule and ensemble). In the materials section I provide an appendix for the list of various reagents used.

3.1 Methods

3.1.1 Purification of recombinant proteins

Purification of Nup153FG single cysteine mutants

Lysis buffer: 2 M urea, 4xPBS pH 8.5, 5 mM imidazole, 1 mM PMSF, 0.2 mM TCEP

Wash buffer 1: 2 M urea, 4xPBS pH 8.5, 10 mM imidazole, 1 mM PMSF, 0.2 mM TCEP

Wash buffer 2: 2 M urea, 4xPBS pH 8.5, 15 mM imidazole, 1 mM PMSF, 0.2 mM TCEP

Elution buffer: 2 M urea, 4xPBS pH 8.5, 400 mM imidazole, 1 mM PMSF, 0.2 mM TCEP

TEV cleavage buffer: 50 mM Tris pH 7.5, 150 mM NaCl, 1 mM PMSF, 0.2 mM TCEP

Dialysis buffer: 2 M urea, 4xPBS pH 8.5, 1 mM PMSF, 0.2 mM TCEP

SEC buffer: 2 M urea, 4xPBS pH 8.5, 1 mM PMSF, 0.2 mM TCEP

Storage buffer: 4M GdmHCl, 1xPBS pH 7.4

A small amount of cells from a frozen glycerol stock of *E.coli* BL21 DE3 (AI) cells harbouring the required plasmids, either of pTXB3-6His-N153FG-Intein-CBD_883Cys, pTXB3-6His-N153FG-Intein-CBD_990Cys, pTXB3-6His-N153FG-Intein-CBD_1330Cys and pTXB3-6His-N153FG-Intein-CBD_1355Cys (all the constructs expressed 875aa-1475aa of the human Nup153 sequence with all internal cysteines removed and cysteines introduced at either of 883,990,1330 and 1355 positions with a fusion of a 6His TEV site on the N-terminal and an Intein-CBD domain at the C-terminal) plasmid was inoculated in LB medium supplemented with 50 µg/ml of ampicillin. The cultures were grown overnight at 37°C with shaking. For protein expression TB medium was inoculated with a 1:100 dilution of the overnight culture. The TB cultures were shaken at 37°C and cell growth was monitored periodically by measuring OD@600nm of the cultures. The cultures were induced for protein expression with 1 mM IPTG and 0.02 % arabinose at OD@600nm=1. Post induction the cells were grown for an additional 6 h at 37°C with shaking. Cells were harvested by centrifugation in a Beckmann centrifuge, rotor JLA 8.100, at 5000 rpm for 20 min at 4°C. The harvested cell mass was resuspended in lysis buffer (10ml/L expression). Cell disruption and lysis was achieved via 3-5 rounds of passage through a microfluidizer or by sonication. The lysate was subsequently centrifuged in a Beckmann centrifuge, rotor JA 25.50 26 at 15000 rpm for 1 h at 4°C to clarify it. The clarified lysate was then incubated on Ni-NTA bearing agarose beads (1ml/L expression, the beads were

already equilibrated in lysis buffer before the clarified lysate was added) for 2 h at 4°C under gentle rotation. The suspension of the beads in the lysate was poured on polypropylene columns that were prewashed with water and lysis buffer. The flow through was collected and the beads were subsequently washed with wash buffer 1 and wash buffer 2 (10 ml of each of the wash buffers 1 and 2 was used per unit volume of beads). The protein was eluted with elution buffer (5 ml of elution buffer per unit volume of bead). The eluate was incubated on chitin beads, prewashed with elution buffer, (2ml of chitin beads/L expression) overnight at 4°C with gentle rotation. The flow through was discarded and the beads were washed with lysis buffer (10ml per unit volume of beads) and then were equilibrated on TEV cleavage buffer (1 ml per unit volume of beads). 0.5 mg of TEV protease was added per litter of expression to the suspension of beads in cleavage buffer and 2-mercaptoethanol was added to a final concentration of 100 mM. Cleavage was performed for a minimum of 6 hours (upto overnight) at room temperature under gentle rotation. The flow through containing the cleaved protein was collected and dialyzed against dialysis buffer to remove the 2-mercaptoethanol and exchange the protein to mildly denaturing conditions. The dialysate was subsequently incubated on agarose beads bearing Ni-NTA beads to remove uncleaved protein (0.5-1 ml/L expression). The flow through was then supplemented with solid GdmHCl powder to a concentration of 4M and concentrated using centrifugal filters (3kDa cut off) and subsequently exchanged with storage buffer. The protein concentration of the sample was estimated using BCA assay with dilutions of bovine serum albumin (BSA) as a standard and the sample was flash frozen and stored at -80°C. Samples from all purification stages were analysed with SDS page. Typically for most purification the flow through from second round of Ni-NTA purification contained the protein with sufficient purity and was directly used for labelling (See Figure 3.1).

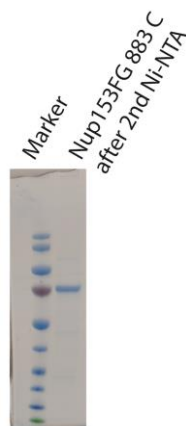


Figure 3.1 Representative purification of Nup153FG single cysteine mutants: SDS page after the final step of purification (2nd round of Ni-NTA purification).

If however this was not the case the protein was further purified via size exclusion chromatography on a Superdex-200 (10/300) column. The fractions were analysed with SDS

page and those containing the pure protein were pooled together. The pooled fractions were subsequently concentrated and exchanged in storage buffer using centrifugal filters (3kDa cut off). The concentrated sample was flash then frozen and stored at -80°C after its concentration has been estimated using BCA assay.

Purification of IBB single and double cysteine mutants

Lysis buffer: 2 M urea, 4xPBS pH 8.5, 5 mM imidazole, 1 mM PMSF, 0.2 mM TCEP

Wash buffer: 2 M urea, 4xPBS pH 8.5, 25 mM imidazole, 1 mM PMSF, 0.2 mM TCEP

Elution buffer: 2 M urea, 4xPBS pH 8.5, 400 mM imidazole, 1 mM PMSF, 0.2 mM TCEP

Dialysis buffer: 2 M urea, 4xPBS pH 8.5, 1 mM PMSF, 0.2 mM TCEP

SEC buffer: 2 M urea, 4xPBS pH 8.5, 1 mM PMSF, 0.2 mM TCEP

Storage buffer: 4M GdmHCl, 1xPBS pH 7.4

A small amount of cells from a frozen glycerol stock of *E.coli* BL21 DE3 (AI) cells harbouring the either pBAD-IBB-Intein-CBD-12His_S24C or pBAD-IBB-Intein-CBD-12His_S24C/S55C plasmids (all constructs expressed 1aa-95aa of human Importin α -1 that contained the IBB domain with a C-terminal Intein-CBD-12His tag; the IBB domain had cysteine insertions at position 24 for a single cysteine construct and position 24 and 55 for a double cysteine construct) was inoculated in LB medium supplemented with 50 μ g/ml of ampicillin. The cultures were grown overnight at 37°C with shaking. For protein expression TB medium was inoculated with a 1:100 dilution of the overnight culture. The TB cultures were shaken at 37°C and cell growth was monitored periodically by measuring OD@600nm of the cultures. The cultures were induced for protein expression with 0.02 % arabinose at OD@600nm=0.6-0.8. Post induction the cells were grown for an additional 6 h at 37°C with shaking. Cells were harvested by centrifugation in a Beckmann centrifuge, rotor JLA 8.100, 5000 rpm for 20 min at 4°C. Harvested cell mass was resuspended in lysis buffer (10ml/L expression). Cell disruption and lysis was achieved via 3-5 rounds of passage through a microfluidizer or by sonication. The lysate was subsequently centrifuged in a Beckmann centrifuge, rotor JA 25.50 26 at 15000 rpm for 1 h at 4°C to clarify it. The lysate supernatant was then incubated on Ni-NTA bearing agarose beads (1ml/L expression, beads were pre-equilibrated in lysis buffer) for 2 h at 4°C under gentle rotation. The suspension of the beads in the lysate was poured on polypropylene columns that were prewashed with water and lysis buffer. The flow through was collected and the beads were subsequently washed with wash buffer (20 ml of wash buffer was used per unit volume of beads). The protein was eluted with elution buffer (5 ml of elution buffer per unit volume of bead). The eluate was supplemented with 2-mercaptoethanol to a final concentration of 100 mM and incubated overnight at room temperature with gentle rotation to cleave the intein-CBD-12His tag. The sample was then dialyzed against dialysis buffer to remove the 2-Mercaptoethanol and imidazole. The dialysate was subsequently incubated on agarose beads bearing Ni-NTA beads to remove uncleaved protein (0.5-1 ml/L expression). The flow through containing mainly the pure protein was then supplemented with solid GdmHCl powder to a

concentration of 4M and concentrated using centrifugal filters (3kDa cut off) and subsequently exchanged with storage buffer. The protein concentration of the sample was estimated using BCA assay with dilutions of bovine serum albumin (BSA) as a standard and the sample was flash frozen and stored at -80°C. Samples from all purification stages were analysed with SDS page. Typically for most purification the flow through from second round of Ni-NTA purification contained the protein with sufficient purity (See Figure 3.2) and was directly used for labelling. If however this was not the case the protein was further purified via size exclusion



Figure 3.2 Representative purification of IBB: SDS page after the final step of purification (2nd round of Ni-NTA purification)

chromatography on a Superdex 75 (10/300) column. The fractions were analysed with SDS page and those containing the pure protein were pooled then concentrated and exchanged in storage buffer using centrifugal filters (3kDa cut off) and the sample was flash frozen and stored at -80°C after its concentration had been estimated using BCA assay.

Purification of Nup153FG WT

Lysis buffer: 2 M urea, 4xPBS pH 8.5, 5 mM imidazole, 1 mM PMSF, 0.2 mM TCEP

Wash buffer: 2 M urea, 4xPBS pH 8.5, 25 mM imidazole, 1 mM PMSF, 0.2 mM TCEP

Elution buffer: 2 M urea, 4xPBS pH 8.5, 400 mM imidazole, 1 mM PMSF, 0.2 mM TCEP

Dialysis buffer: 2 M urea, 4xPBS pH 8.5, 1 mM PMSF, 0.2 mM TCEP

HPLC buffer A: ddH₂O, 0.1 % trifluoroacetic acid (TFA)

HPLC buffer B: acetonitrile (MeCN), 0.1 % TFA

Storage buffer: 4M GdmHCl, 1xPBS pH 7.4

Unlabeled Nup153FG WT was used to assess the selectivity of thiol labelling with acrylodan. The expression and purification of Nup153FG WT (the construct was pBAD-N153FG-Intein-CBD-12His expressing 875aa-1475aa of Nup153 with an Intein-CBD-12His C-terminal fusion,

with all internal cysteine residues of Nup153 removed) is the same as for IBB single cysteine mutant with the exception that after the 2nd round of Ni-NTA purification the sample was purified via RP-HPLC. The protein sample obtained after 2nd round of Ni-NTA purification was mixed with 5 % MeCN and acidified with HCl (1% HCl final concentration) and then clarified via filtration with a 0.22 µM syringe filtration unit. The sample was loaded on a C18 HPLC column pre-equilibrated with 95 % buffer A and 5 % buffer B. The protein was eluted from the column by running a gradient from 5-100 % of buffer B. Fractions eluting at 60-64% of buffer B primarily contained the protein as was verified from SDS page analysis. This fraction was flash frozen and was lyophilized into a powder, which was dissolved in storage buffer and exchanged multiple times with fresh storage buffer to remove any residual TFA, concentrated and flash frozen for later use after its concentration has been estimated with BCA assay.

Purification of NSP1FG single cysteine mutant

Lysis buffer: 2 M urea, 4xPBS pH 8.5, 5 mM imidazole, 1 mM PMSF, 0.2 mM TCEP
Wash buffer: 2 M urea, 4xPBS pH 8.5, 25 mM imidazole, 1 mM PMSF, 0.2 mM TCEP
Elution buffer: 2 M urea, 4xPBS pH 8.5, 400 mM imidazole, 1 mM PMSF, 0.2 mM TCEP
Dialysis buffer: 2 M urea, 4xPBS pH 8.5, 1 mM PMSF, 0.2 mM TCEP
SEC buffer: 2 M urea, 4xPBS pH 8.5, 1 mM PMSF, 0.2 mM TCEP
Storage buffer: 4M GdmHCl, 1xPBS pH 7.4

The expression and purification of NSP1FG single cysteine mutant (the construct was pBAD-NSP1(1-602)-Intein-CBD-12His_101C expressing Yeast NSP1(1aa-601aa) 101C with a C-terminal Intein-CBD-12His) was identical to that of IBB single cysteine mutant, albeit with one difference mentioned below.

The purity of the protein in the flow through after 2nd round of Ni-NTA purification was not sufficient. Hence after this purification step, protein was further purified via size exclusion chromatography on a Superdex-200 (10/300) column. The fractions were analysed with SDS page and those containing the pure protein were pooled then concentrated and exchanged in storage buffer using centrifugal filters (3kDa cut off) and the sample was flash frozen and stored at -80°C after its concentration has been estimated using BCA assay. This sample was used for further labelling.

Purification of NSP1FG fragment with single cysteine and single amber mutation

Lysis buffer: 2 M urea, 4xPBS pH 8.5, 5 mM imidazole, 1 mM PMSF, 0.2 mM TCEP
Wash buffer: 2 M urea, 4xPBS pH 8.5, 25 mM imidazole, 1 mM PMSF, 0.2 mM TCEP
Elution buffer: 2 M urea, 4xPBS pH 8.5, 400 mM imidazole, 1 mM PMSF, 0.2 mM TCEP
Dialysis buffer: 2 M urea, 4xPBS pH 8.5, 1 mM PMSF, 0.2 mM TCEP

SEC buffer: 2 M urea, 4xPBS pH 8.5, 1 mM PMSF, 0.2 mM TCEP

Storage buffer: 4M GdmHCl, 1xPBS pH 7.4

A small amount of cells from a frozen glycerol stock of *E.coli* BL21 DE3 (AI) cells harbouring the pBAD-NSP1(2-175)-Intein-CBD-12His_3C/174TAG plasmid (the plasmid expressed NSP1(2aa-175aa) with a C-terminal Intein-CBD-12His fusion and with a cysteine insertion in position 3 and a TAG insertion in position 174) and pEvol-AcF plasmid, which encodes the orthogonal tRNA/aaRS (aminoacyl t-RNA synthetase) pair for charging the tRNA^{TAG} with the ncAA AcF, was inoculated in LB medium supplemented with 50 µg/ml of ampicillin and 33 µg/ml of chloramphenicol. The cultures were grown overnight at 37°C with shaking. For protein expression TB medium was inoculated with a 1:100 dilution of the overnight culture. The TB cultures were shaken at 37°C and cell growth was monitored periodically by measuring OD@600nm of the cultures. The ncAA AcF was added from 1M stock in water to the cultures to a final concentration of 1mM when the OD@600nm of the cultures was between 0.2-0.4. The cultures were induced for protein expression 0.02 % arabinose when OD@600nm was between 0.6-0.8. Post induction the cells were grown for an additional 6 hours at 37°C with shaking. Cells were harvested by centrifugation in a Beckmann centrifuge, rotor JLA 8.100, 5000 rpm for 20 min at 4°C. Subsequently the purification method was identical to that of NSP1FG single cysteine mutant, with the only exception that the size exclusion chromatography step was performed on a Superdex 75 (10/300) column instead of a Superdex 200 (10/300) column owing to the much smaller size of NSP1FG fragment .

Purification of Importinβ

Lysis buffer: 50 mM Tris-HCl pH 7, 650 mM NaCl, 5 mM MgCl₂, 5 mM imidazole, 1 mM PMSF, 0.2 mM TCEP.

Wash buffer 1: 50 mM Tris-HCl pH 7, 650 mM NaCl, 5 mM MgCl₂, 10 mM imidazole, 1 mM PMSF, 0.2 mM TCEP.

Wash buffer 2: 50 mM Tris-HCl pH 7, 650 mM NaCl, 5 mM MgCl₂, 15 mM imidazole, 1 mM PMSF, 0.2 mM TCEP.

Elution buffer: 50 mM Tris-HCl pH 7, 650 mM NaCl, 5 mM MgCl₂, 400 mM imidazole, 1 mM PMSF, 0.2 mM TCEP.

SEC buffer: 50 mM Tris-HCl pH 7, 650 mM NaCl, 5 mM MgCl₂, 1 mM PMSF, 0.2 mM TCEP.

Storage buffer: 50 mM Tris-HCl pH 7, 650 mM NaCl, 5 mM MgCl₂, 1 mM PMSF, 0.2 mM TCEP, 25% glycerol

A small amount of cells from a frozen glycerol stock of *E.coli* BL21 DE3 (AI) cells harbouring the plasmid pTXB3-12His-Importin beta WT (which expresses human Importinβ with an Intein-CBD-12His as a C-terminal fusion) and was incubated under shaking conditions overnight at 37°C. Then the overnight culture was added in a 1:100 dilution to TB medium containing 50 µg/ml ampicillin. The cultures were grown at 37°C with shaking with frequent monitoring of

OD@600nm. Protein expression was induced by the addition of 1mM IPTG and 0.02 % arabinose at OD@600nm=0.4-0.6. The cultures were grown at 30°C overnight with shaking after induction. Cells were harvested by centrifugation in a Beckmann centrifuge, rotor JLA 8.100, 5000 rpm for 20 min at 4°C. The harvested cell mass was resuspended with lysis buffer (10ml/L expression). Cell disruption and lysis was achieved via 3-5 rounds of passage through a microfluidizer or by sonication. The lysate was subsequently centrifuged in a Beckmann centrifuge, rotor JA 25.50 26 at 15000 rpm for 1 h at 4°C to clarify it. The lysate supernatant was then incubated on Ni-NTA bearing agarose beads (1ml/ L expression) for 2 h at 4°C under gentle rotation. The suspension of the beads in the lysate was poured on polypropylene columns that were prewashed with water and lysis buffer. The flow through was collected and the beads were subsequently washed with lysis buffer, wash buffer 1 and wash buffer 2 (10 ml of lysis buffer and each of the wash buffer was used per unit volume of beads). The protein was eluted with elution buffer (10 ml of elution buffer per unit volume of bead). The eluate was supplemented with 2-mercaptoethanol to a final concentration of 100 mM and incubated overnight at room temperature with gentle rotation to cleave the intein-CBD-12His tag. The sample was then dialyzed against dialysis buffer to remove the 2-mercaptoethanol and imidazole at 4°C. The dialysate was subsequently incubated on agarose beads bearing Ni-NTA beads to remove uncleaved protein (0.5-1 ml/L expression). The flow through was collected. All stages of the purification were analysed on a SDS page. The collected flow through was then concentrated and subsequently purified by size exclusion chromatography (SEC) at 4°C on a Superdex 200 column (16/600). From the elution profile of the SEC run fractions where the monomeric protein eluted were identified. These fractions were then analysed on a SDS page and fractions containing the pure protein were pooled and subsequently concentrated and exchanged with storage buffer using centrifugal filters (5kDa cutoff), flash frozen and stored at -80°C after its concentration has been estimated from absorbance at 280 nm using an extinction coefficient of 78270 M⁻¹cm⁻¹.

Table for all purifications

Here I list all the proteins purified with the actual description of the proteins and how they are referred to in the results and the plasmids used.

Plasmid	Protein purified	Name primarily used in following sections to refer to the protein
pTXB3-12His-Importin beta WT	Human Importinβ	Importinβ
pBAD-N153FG-Intein-CBD-12His	Human Nup153(875aa-1475aa), all internal cysteines were removed from the sequence	Nup153FG WT
pTXB3-6His-N153FG-Intein-CBD_883Cys	Human Nup153(875aa-1475aa), all internal cysteines were removed from the sequence and cysteine was introduced at position 883	Nup153FG 883C

pTXB3-6His-N153FG-Intein-CBD_990Cys	Human Nup153(875aa-1475aa), all internal cysteines were removed from the sequence and cysteine was introduced at position 990	Nup153FG 990C
pTXB3-6His-N153FG-Intein-CBD_1330Cys	Human Nup153(875aa-1475aa), all internal cysteines were removed from the sequence and cysteine was introduced at position 1330	Nup153FG 1330C
pBAD-IBB-Intein-CBD-12His_S24C	Human Importin α -1(1aa-95aa), with cysteine introduced at position 24	IBB S24C
pBAD-IBB-Intein-CBD-12His_S24C/S55C	Human Importin α -1(1aa-95aa), with cysteines introduced at S24C and S55C mutation	IBB S24C/S55C
pBAD-NSP1(1-602)-Intein-CBD-12His_101C	Yeast NSP1(1aa-601aa) with cysteine introduced 101 position	NSP1FG 101C
pBAD-NSP1(2-175)-Intein-CBD-12His_3C/174TAG	Yeast NSP1(2aa-175aa) with cysteine introduced at position 3 and TAG (amber stop codon) introduced at position 174	NSP1FG fragment

3.1.2 Fluorescent labeling of recombinant proteins

Acrylodan labelling of Nup153FG, NSP1FG and IBB single cysteine constructs

DTT wash buffer: 4 M GdmHCl, 1xPBS pH 7, 0.2 mM EDTA, 10 mM DTT

TCEP wash buffer: 4 M GdmHCl, 1xPBS pH 7, 0.2 mM EDTA, 0.2 mM TCEP (this buffer was degassed by prolonged incubation under vacuum with stirring to remove all dissolved oxygen)

SEC buffer: 2 M urea, 4xPBS pH 8.5, 1 mM PMSF, 0.2 mM TCEP

Storage buffer: 4M GdmHCl, 1xPBS pH 7.4

10-50 nmoles of the proteins were buffer exchanged 3x with DTT wash buffer to reduce all cysteine residues using centrifugal filters (3kDa cutoff). The sample was subsequently exchanged with TCEP wash buffer 5x using centrifugal filters (3kDa cutoff) to remove excess DTT. This sample was concentrated to a concentration of \sim 150 μ M. To this protein sample a freshly prepared solution of acrylodan in DMF (N,N-Dimethylformamide) of appropriate concentration was added such that the final concentration of the DMF in the labelling reaction was under 5% and the molar excess of acrylodan over the protein was \sim 6.5 fold. The labelling reaction was allowed to proceed for 4 h in the dark with mild shaking at room temperature. After 4 h the sample was centrifuged at 16,000 rpm on an Eppendorf tabletop centrifuge for 15 minutes to remove most of the poorly soluble unreacted acrylodan which settled as a pellet. The supernatant was taken and DTT was added to a final concentration of 10 mM to quench any unreacted acrylodan. The sample was then washed 3-4x with storage buffer, concentrated and purified by SEC on a S-75(10/300) column (for IBB constructs) or a S-200(10/300) column (for Nup153FG and NSP1FG constructs) which were pre-equilibrated with SEC buffer. The fractions were run on a SDS page and analysed by coomassie staining and fluorescent scanning. The fractions

containing the pure fluorescently labelled protein were pooled, exchanged with storage buffer, concentrated, flash frozen and stored at -80°C , after its concentration has been estimated. The protein concentration was estimated using BCA assay and the dye concentration was estimated from absorbance at 391 nm using an extinction coefficient of $20,000\text{ M}^{-1}\text{cm}^{-1}$ for acrylodan. The labelling efficiency defined as percentage of labelled protein was typically 50-75% with this protocol. Acrylodan bears an α,β -unsaturated carbonyl as the reactive handle towards cysteine. This functionality is not as reactive as maleimides and also known to be reactive towards amine¹⁵³. Thus to validate that our protocol yielded both good labelling efficiency and selectivity a control experiment was performed where identical amounts of wild type Nup153FG (cysteine less) and a single cysteine mutant Nup153FG 883C was labelled with acrylodan in identical conditions following the above mentioned protocol. Aliquots were taken from the labelling reactions after 2 and 4 h and flash frozen and subsequently analysed with SDS page. This assay showed the selectivity of acrylodan towards cysteine using our protocol to be $>90\%$ (See Figure 3.3).



Figure 3.3 Selectivity of acrylodan labelling: Fluorescent scan of a SDS-page of labelling reactions of wild-type (wt) and 883C variant of Nup153FG with acrylodan, at 2 h and 4 h, showing selective labelling of the cysteine mutant and minimal background labelling of the wt.

Alexa488 and 594 maleimide double labelling of IBBS24C/S55C construct

DTT wash buffer: 4 M GdmHCl, 1xPBS pH 7, 0.2 mM EDTA, 10 mM DTT

TCEP wash buffer: 4 M GdmHCl, 1xPBS pH 7, 0.2 mM EDTA, 0.2 mM TCEP

SEC buffer: 2 M Urea, 4xPBS pH 8.5, 1 mM PMSF, 0.2 mM TCEP

Storage buffer: 4M GdmHCl, 1xPBS pH 7.4

10-25 nmoles of the IBB S24C/S55C was exchanged 3x with DTT wash buffer to reduce all cysteine residues using centrifugal filters (3kDa cutoff). The sample was subsequently exchanged with TCEP wash buffer 5x using centrifugal filters (3kDa cutoff) to remove excess DTT. This sample was concentrated to a concentration of $\sim 150\text{-}200\mu\text{M}$. To this protein sample a freshly prepared solution of Alexa488 maleimide and Alexa594 maleimide in DMSO was added such that the final concentration of the DMSO in the labelling reaction was under 5% and the molar

excess of Alexa488 and Alexa594 over the protein was 3 and 3.5 fold respectively. The labelling reaction was allowed to proceed for 4 h in the dark with mild shaking at room temperature. After 4 h DTT was added to the sample a final concentration of 10mM to quench all unreacted dye. The sample was then washed 3-4x with storage buffer, concentrated and purified by SEC on a S-75(10/300) column which was pre-equilibrated with SEC buffer. The fractions were run on a SDS page and analysed by coomassie staining and fluorescent scanning. The fractions containing the pure fluorescently labelled protein were pooled; exchanged with storage buffer, concentrated, flash frozen and stored at -80°C, after its concentration has been estimated. The protein concentration was estimated using BCA assay and the dye concentration for Alexa488 and Alexa594 was estimated from absorbance at 496 nm and 590 nm respectively using extinction coefficients provided by the manufacturer, 71,000 M⁻¹cm⁻¹ and 73,000 M⁻¹cm⁻¹ for Alexa488 and Alexa594 respectively. The labelling efficiency defined as percentage of labelled protein was typically >70% for each of Alexa488 and Alexa594.

Alexa488 hydroxylamine and Alexa594 maleimide double labelling of NSP1(1-175)C2TAG175 construct

Oxime ligation buffer: 4 M GdmHCl, 1xPBS pH 4, 50 mM sodium acetate-HCl, 0.2 mM TCEP

DTT wash buffer: 4 M GdmHCl, 1xPBS pH 7, 0.2 mM EDTA, 10 mM DTT

TCEP wash buffer: 4 M GdmHCl, 1xPBS pH 7, 0.2 mM EDTA, 0.2 mM TCEP

SEC buffer: 2 M Urea, 4xPBS pH 8.5, 1 mM PMSF, 0.2 mM TCEP

Storage buffer: 4M GdmHCl, 1xPBS pH 7.4

SEC buffer: 2 M Urea, 4xPBS pH 8.5, 1 mM PMSF, 0.2 mM TCEP

Storage buffer: 4M GdmHCl, 1xPBS pH 7.4

10-25 nmoles of the NSP1 fragment was buffer exchanged 3x with oxime ligation buffer using centrifugal filters (3kDa cutoff). This sample was concentrated to a concentration of ~200µM. To this protein sample a freshly prepared solution of Alexa488 hydroxylamine in DMSO was added such that the final concentration of the DMSO in the labelling reaction was under 5% and the molar excess of Alexa488 over the protein was 3.5. The labelling reaction was allowed to proceed overnight in the dark with mild shaking at 60°C. After this stage the labelling with Alexa594 maleimide, purification and quantification was done exactly the same way as in the case of labelling of IBBS24C/S55C construct with the sole difference that in this case only Alexa594 maleimide was used in the labelling. The labelling efficiency defined as percentage of labelled protein was typically >50% for each of Alexa488 and >70% for Alexa594.

3.1.3 Fluorescence lifetime measurements using TCSPC

The laser pulse used in a TCSPC setup is not a δ -function and has a finite width and a characteristic shape and thus can be approximated by a sum of several delta functions with

different amplitudes. Thus the measured fluorescence decay $I(t)_{measured}$ is a convolution integral of the actual decay function $I(t)$ and the instrument response function IRF, which basically describes the fastest time response that can be obtained in a particular TCSPC setup and is in itself a convolution of the laser pulse profile and all other factors that contribute to the setups time response such the counting electronics (Equation 3.1)¹⁵⁴.

Equation 3.1

$$I(t)_{measured} = \int_0^t I(t - t')IRF(t')dt' = I(t) \otimes IRF$$

The model decay function $I(t)$ is typically described as a sum of n exponentials with time constants τ_i and a_i as corresponding amplitudes (Equation 3.2)¹⁵⁴

Equation 3.2

$$I(t) = \sum_{i=1}^n a_i \exp\left(-\frac{t}{\tau_i}\right)$$

For lifetime decay measurements the emission polarizer was set to 54.7° relative to the excitation polarizer to attain magic angle conditions to negate the effect of any depolarization processes (such as segmental motion and rotation) on the fluorescence decay. The data was acquired such that the count rates were not more than 1% of the frequency of the laser pulse to avoid photon pile-up¹⁵⁴ and the count rates were typical kept at 200kcps. Typically decays were measured till the peak count value was 30,000 photons. The IRF was measured with a sample that has a zero time response and thus the measured time response originates solely from the setup. For this purpose typically a scatterer is used; I used a dilute solution of ludox (0.05%) in water and the signal was measured at the same wavelength as the excitation pulse. The count rate for measurement of the IRF was kept much lower than that when measuring lifetime decays. This is to account for the fact that a decay and an IRF has very different temporal profiles, the former being temporally very narrow. The differential count rate which is the actual, momentary photon detection probability in a given time window when the signal is actually present can be actually very high, owing to the ultrafast pulsed nature of an IRF signal, even when average count rates are 1% of the frequency of the laser pulse. Thus for IRF measurements it is necessary to use low count rates. For IRF measurements typical count rates were kept between 5-10 kcps.

The measured decays were fitted as a convolution integral of a sum of exponentials with measured IRF using iterative reconvolution in SymPhoTime 64 software (PicoQuant, Berlin). Since the IRF is always measured at a fixed wavelength, when using a scattering solution, while the decays are measured at different wavelengths the actual IRF at the wavelength where the decays are measured can be shifted in time for the measured IRF. This time shift is accounted for in the fitting procedure where the time shift between the IRF and the decay is a fit parameter. To correct for this shift when decays were measured at wavelengths > 120 nm from the IRF, the

shift between the IRF and the decay was used as a fixed parameter in the fit and was obtained by fitting the decay of a monoexponential emitter like R6G measured at the same wavelength as the decay.

Lifetime data for solvation dynamics was typically measured with 1 μ M labelled protein and varying amounts of unlabelled binding partner (described for in the relevant figure legend) in 1xPBS buffer (pH 7.4) supplemented with 2mM magnesium acetate and DTT. For titration experiments lifetimes were measured with 50 nM labelled protein in the same buffer and titrated with increasing concentrations of binding partner.

3.1.4 Time resolved anisotropy measurements

For time resolved anisotropy measurements, decays were measured at parallel ($I(t)_{para}$) and perpendicular ($I(t)_{perp}$) polarization conditions with the emission polarization was set to 0° and 90° with respect to the excitation polarization respectively. The anisotropy $r(t)$ decay was constructed following equation Equation 3.3¹⁵⁵.

Equation 3.3

$$r(t) = \frac{I(t)_{para} - GI(t)_{perp}}{I(t)_{para} + 2GI(t)_{perp}}$$

G is a parameter that accounts for the differential detection efficiencies in different polarizations and was obtained using the long-time tail matching method¹⁵⁶ by measuring a free rotor in fluid solvent, in our case Bis-ANS dye in methanol. For such a system the tails of the parallel and perpendicular decay becomes equal at long time or in other words the anisotropy decays to zero. The G factor is obtained by varying the G factor until the tail of the anisotropy is nicely centred on zero value (See Figure 3.4). The G factor of our setup was found to be 0.785 for 400 nm excitation over an emission range of 480 to 540 nm. The time zero point for the obtained anisotropy decay $r(t)$ was set to the time point where parallel decay reached its maximum. The anisotropy decay was fitted using Equation 3.4¹⁵⁵.

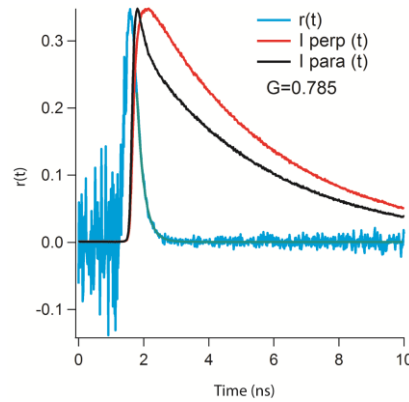


Figure 3.4 G factor calibration using Bis-ANS in methanol: Anisotropy decay $r(t)$ of Bis-ANS in methanol with $G=0.785$ showing the tail of the anisotropy decays to zero. The parallel and perpendicular decays, normalized to the maximum of $r(t)$ is also superimposed on the graph. The anisotropy decay is fitted to a single exponential (green line) yielding a rotational correlation time of ~ 220 ps.

Equation 3.4

$$r(t) = r_0 \left[\sum_{i=1}^n a_i \exp\left(-\frac{t}{\phi_i}\right) \right]$$

The anisotropy decay is described as a sum of exponentials with time constants ϕ_i , known as rotational correlation times, having corresponding amplitudes a_i and with the r_0 the initial anisotropy. For cases of free dye in a fluid solvent one rotational correlation time is sufficient and for protein samples typically two rotational correlation times are used.

Time resolved anisotropy data for IDP samples was typically measured with $1\mu\text{M}$ labelled protein and varying amounts of unlabelled binding partner (described for in the relevant figure legend) in 1xPBS buffer (pH 7.4) supplemented with 2mM $\text{Mg}(\text{OAc})_2$ and DTT. For titration experiments lifetimes were measured with 100nM labelled protein in the same buffer and titrated with increasing concentrations of binding partner.

3.1.5 Solvation dynamics measurement using Time Dependent Fluorescence Stokes Shift (TDFSS) method

To measure solvation dynamics by TDFSS thus one needs to obtain the Time Resolved Emission Spectra (TRES) which is the emission spectra of a probe as a function of time¹⁵⁷. The approach we use to measure TRES is based on spectral reconstruction from the steady state emission spectra and lifetimes measured at different wavelengths. Typically the lifetimes are measured at

multiple wavelengths across the emission spectra. From the time constant and amplitudes of these lifetime decays and the steady state emission intensity at these wavelengths the intensity at those wavelengths can be computed as a function of time, from which the emission spectra at any given time can be obtained by fitting the intensity value at those wavelengths for a given time to line shape. Mathematically the process is described below.

The lifetime decays at each of the measured wavelength $I(\lambda, t)$ is fitted as a sum of exponentials like in Equation 3.2 where $\tau_i\lambda$ are the time constants with associated amplitudes $a_i(\lambda)$ for a given wavelength (See Equation 3.5)¹⁵⁷. A characteristic feature of lifetime decays in a system where solvation dynamics is their striking wavelength dependence, at the blue end of the spectrum (higher energy) decays are fast as the excited state is depopulated both by emission and solvation dynamics while at the red end decays are longer and often have a rise, which is a time component having a negative amplitude.

Equation 3.5

$$I(\lambda, t) = \sum_{i=1}^n a_i(\lambda) \exp\left(-\frac{t}{\tau_i\lambda}\right)$$

Now if the steady state fluorescence intensity at a wavelength be $F(\lambda)$, then for each wavelength a normalization factor $H(\lambda)$ as given below was computed from the steady state intensity and lifetime parameters (See Equation 3.6)¹⁵⁷.

Equation 3.6

$$H(\lambda) = \frac{F(\lambda)}{\sum a_i(\lambda)\tau_i(\lambda)}$$

Then finally the appropriately normalized intensity $I'(\lambda, t)$ as a function of time for a given wavelength λ is given by Equation 3.7¹⁵⁷

Equation 3.7

$$I'(\lambda, t) = H(\lambda) I(\lambda, t)$$

The TRES typically expressed in frequency ν instead of wavelength λ (the relation being $\lambda=1/\nu$) at a given time is computed by fitting the intensity values at different frequencies, given by

equation 3.7, to a spectral line shape function; most commonly a lognormal function given by equation 3.8 is used as a spectral line shape function¹⁵⁸.

Equation 3.8

$$I(\nu) = I_0 \exp(-\ln(2) \left(\frac{\ln[1+2b(\nu-\nu_{\max})/\Delta]}{b} \right)^2) \text{ where } 2b(\nu - \nu_{\max})/\Delta > -1$$

(for $2b(\nu - \nu_{\max})/\Delta = 0$ the expression becomes a Gaussian)

In Equation 3.8 the peak frequency is ν_{\max} with intensity I_0 is the amplitude, Δ is the width of the lognormal shape function and b is the asymmetry parameter. The measurement pipeline is schematically depicted in Figure 3.5.

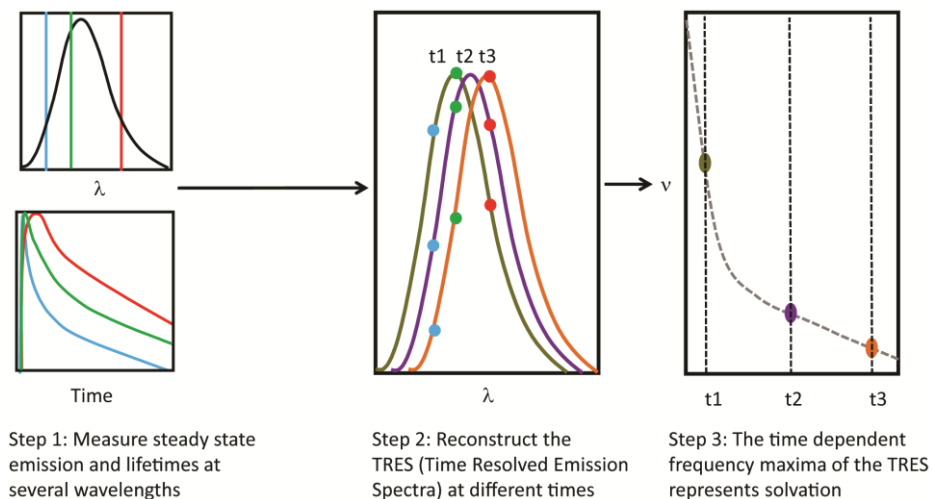


Figure 3.5 Schematic showing the pipeline of TRES measurement: First steady state spectrum (see top left) and lifetimes (see bottom left) at different wavelengths (three representative examples shown with cyan, green and red). From the steady state and time resolved data the intensity at the measured wavelengths at different time points are constructed which are fitted to a lognormal function to obtain the TRES (see middle). In the TRES three representative wavelengths cyan, green and red (which are shown in the left) are shown as points and the representative fitted lognormal shapes in olive, violet and orange are shown for three time points t_1 , t_2 and t_3 . The maximum frequency of TRES at each time point plotted as function of time constitutes the solvent response (see right), with three representative frequency maxima of the TRES at three times t_1 , t_2 and t_3 (the same times shown in the middle) shown with olive, violet and orange dots.

Usually the TDFSS data $v_{\max}(t)$ is directly analysed as a sum of exponential given by Equation 3.9. with time constants τ_i and corresponding amplitudes a_i . The Stokes shift data measured for the different IDP systems were analysed by this approach.

Equation 3.9

$$v(t) = \sum_{i=1}^n a_i \exp\left(-\frac{t}{\tau_i}\right)$$

TDFSS data can also be analysed a normalized function known as the solvation correlation function $C(t)$ given by Equation 3.10 where $v(t)$ is the v_{\max} of the TRES at time t , $v(0)$ is the v_{\max} of the TRES at time 0 and $v(\infty)$ is the v_{\max} of the TRES at infinity, that is after the process of solvation is completed¹⁵⁸.

Equation 3.10

$$C(t) = \frac{v(t) - v(\infty)}{v(0) - v(\infty)}$$

$C(t)$ from equation 3.10 is again typically analysed as a sum of exponentials like that in Equation 3.9. For analysing TDFSS data using $C(t)$ one needs to know the $v(\infty)$ value; which under the assumption that solvation happens much faster than emission is the v_{\max} of the steady state emission¹⁵⁹. However where solvation dynamics happen on a timescale comparable to the lifetime of the probe this does not apply anymore¹⁵⁹.

3.1.6 Basics of FRET and smFRET analysis pipeline

FRET is a dipole-dipole interaction mediated distance dependent non-radiative energy transfer process occurring between two chromophores when the absorption spectra of one chromophore (acceptor chromophore) overlap with the emission spectra of the other chromophore (donor chromophore)¹⁶⁰. FRET results in a quenching of donor fluorescence accompanied by an increase in acceptor fluorescence and the efficiency of the process is expressed as E given by Equation 3.11 where I_{DA} and I_D is the intensity of the donor in the presence and the absence of the acceptor respectively¹⁶⁰.

Equation 3.11

$$E = 1 - \frac{I_{DA}}{I_D}$$

The distance dependence of E is given by Equation 3.12¹⁶⁰ where $E(r_{DA})$ is the E value when the donor and acceptor is separated by a distance of r_{DA} and R_0 is the distance where the FRET efficiency E is 0.5 or 50%. This distance dependence of FRET allows its use to probe conformational changes.

Equation 3.12

$$E(r_{DA}) = \frac{R_0^6}{R_0^6 + r_{DA}^6}$$

R_0 is a constant for a specific dye pair and is given by Equation 3.13, where $J(\lambda)$ is the spectral overlap integral between the donor emission and the acceptor absorption, κ^2 is the orientation factor which can be approximated as 2/3 where the chromophores have substantial rotational freedom and n is the refractive index of the medium, Φ_D is the quantum yield of the donor.

Equation 3.13

$$R_0 = \sqrt[6]{\frac{9(\ln 10)\kappa^2 J(\lambda) \Phi_D}{128 \pi^5 n^4 N_A}}$$

Because of the sixth power dependence of FRET on distance (See Equation 3.12) FRET efficiency very rapidly decreases to zero at distances greater than R_0 . For most typical dye pairs the value of R_0 ranges between 30Å and 90Å¹⁶⁰ and this puts an upper and lower limit of distance where FRET can operate from (~20Å-100Å).

In smFRET data, FRET for each molecules is computed. For this a very dilute solution (picomolar) of fluorescently double labelled molecules are measured in a confocal microscope measuring different fluorescence parameters. The detailed setup is described in a following section. The acquired data is subjected to multiparameter fluorescence analysis^{161,162,163} using a custom written program in IgorPro (Wavemetrics, Oregon, USA). Trajectories of single

molecules passing the confocal volume gives rise to a ‘burst’ of photons. We employed a burst search algorithm on photon stream after lee filtering it¹⁶⁴. Fluorescence intensities(I), lifetimes(τ) and anisotropies(r) were obtained from individual bursts¹⁶² and thus individual molecules. An interphoton lag time threshold of 80 microseconds was used for burst selection and the identified bursts was subsequently subjected to another photon based selection criteria (typically 70 photons/bursts unless mentioned otherwise)

FRET efficiencies and stoichiometry S can be calculated from the photon counts using Equation 3.14 and 3.15 respectively¹⁶⁵.

Equation 3.14

$$E_{FRET} = \frac{I_A^D}{\gamma I_D^D + I_A^D}$$

Equation 3.15

$$S = \frac{\gamma I_D^D + I_A^D}{\gamma I_D^D + I_A^D + I_A^A}$$

Here I_x^y describes the corrected intensity I detected in x channel upon excitation with y laser pulse and D and A refer to donor and acceptor; thus as an example I_A^D refers to corrected intensity detected in acceptor channel upon excitation with donor laser. γ accounts for differential quantum yields of donor and acceptor dyes and differential detection efficiencies of acceptor and donor channels. Photon counts used in Equation 3.14 and 3.15 were corrected for leakage of donor signal into the acceptor channel and direct excitation of the acceptor from the laser pulse used to excite the donor.

Typically for smFRET experiments 50-100pM concentration of double labelled protein samples were measured for 1 h in 1x PBS (pH 7.4) supplemented with 10mM DTT and 2mM Mg(OAc)₂ and upto 5μM of unlabelled binding partners depending on the experiment.

3.1.7 Single molecule Fluorescence Correlation Spectroscopy (FCS)

Fluorescence correlation spectroscopy (FCS) can be used to determine diffusion coefficients and thus hydrodynamic radius of molecules¹⁶⁶. The technique is based on analyzing decay correlation of intensity fluctuations of fluorescence detected from a small volume (here a confocal excited

volume). Such correlation decay is caused primarily by Brownian diffusion allowing estimation of diffusion coefficients and consequently size changes in molecules¹⁶⁶. The correlation function is defined by Equation 3.16 $G(\tau)$ is the correlation for lag-time τ where $\delta I(t)$ and $\delta I(t + \tau)$ are the difference in fluorescence intensity from the mean intensity $\langle I \rangle$ at time t and $t + \tau$ respectively.

Equation 3.16

$$G(\tau) = \frac{\langle \delta I(t) \delta I(t + \tau) \rangle}{\langle I \rangle^2}$$

If only Brownian diffusion contributes to the decay of the correlation then the process can be described by Equation 3.17. Here $G(\tau)$ is the correlation for lag-time τ , τ_D is the diffusion time and N is the average number of emitting species in the confocal volume. A confocal volume can be described by a 3D ellipsoid, however since I collect the FCS data from the same experiment as for smFRET our confocal volume is very elongated in z ($z \gg x, y$ dimensions) owing to using an under-filled objective. This allows diffusion in the volume to be approximated as 2D diffusion. Thus equation 3.17 describes the decay of $G(\tau)$ due to 2D diffusion.

Equation 3.17

$$G(\tau) = \frac{1}{N} \left(1 + \frac{\tau}{\tau_D} \right)^{-1}$$

In reality the correlation decay is not exclusively due to Brownian diffusion. Any fluctuation in fluorescence intensity causes decay of correlation on timescales that are relevant for the process in question. Due to the use of picosecond pulsed excitation at moderately high power that I used in these experiments, a detectable fraction of the fluorophores go to non-fluorescent dark states triplet states. This switching between these two states results in fluorescence intensity fluctuations and if $G(\tau)$ only decays due to such fluctuations it can be described by Equation 3.18 where $G(\tau)$ is the correlation for lag-time τ , T is the fraction of molecules in the triplet state and τ_T is the single-triplet relaxation time.¹⁶⁶

Equation 3.18

$$G(\tau) = \left[1 + \frac{T}{1-T} \exp(-\tau/\tau_T) \right]$$

Usually triplet dynamics and diffusion happen on very different time timescales, microseconds and milliseconds being the timescales associated with triplet dynamics and diffusion respectively. This separation of time scales allows the description of $G(\tau)$ from microseconds to milliseconds as a product of the two terms, given in equation 3.19, accounting for diffusion and triplet dynamics (product of Equation 3.17 and 3.18). I fitted my FCS data with Equation 3.19.

Equation 3.19

$$G(\tau) = \frac{1}{N} \left[1 + \frac{T}{1-T} \exp(-\tau/\tau_T) \right] \left(1 + \frac{\tau}{\tau_D} \right)^{-1}$$

FCS data were extracted from smFRET experiments; thus the measurement condition was one and the same as in smFRET experiments described in previous section.

3.1.8 Measuring static microenvironment polarity with acrylodan steady state emission

The static polarity of a medium is expressed very well by relative permittivity ϵ_r of the medium (where $\epsilon_r = \epsilon/\epsilon_{\text{vacuum}}$). A medium with a high dielectric constant can solvate polar species better by stabilizing a polarized charge distribution of a polar molecule through dipole dipolar interactions. Most solvatochromic probes including acrylodan have dipolar excited states and thus their emission spectrum is sensitive to ϵ_r and thus micropolarity of the medium. For many solvatochromic probes maximal frequency of emission (ν_{max}) shows a linear dependence on ϵ_r ¹⁶⁷. Hence to estimate the local polarity expressed by ϵ_r I used emission maxima data for acrylodan-2-mercaptoethanol conjugate in different solvents (1,4-dioxane, ethanol, methanol, acetonitrile and water) of different ϵ_r from literature¹⁶⁸. The micropolarity in terms of ϵ_r experienced by acrylodan in the different protein environments I measured was estimated the emission maxima ν_{max} using Equation 3.20. Equation 3.20 was obtained from a linear fit of the emission maxima data for acrylodan-2-mercaptoethanol conjugate in different solvents¹⁶⁸ vs corresponding ϵ_r of those solvents.

Equation 3.20

$$\epsilon_r = -0.013\nu_{\text{max}} + 304$$

3.1.9 Measuring apparent disassociation constants (K_D) of Nup153FG and Importin β using acrylodan lifetime

For measurement of apparent binding constants using acrylodan lifetime decays was used. Lifetime decays of acrylodan labelled Nup153FG samples were measured in TCSPC with varying concentrations of Importin β . Average lifetimes τ_{avg} were obtained from the TCSPC decays using Equation 3.21 after the decays were fitted to multiexponentials using Equation 3.21.

Equation 3.21

$$\tau_{avg} = \frac{\sum \tau_i a_i}{\sum a_i}$$

Here τ_{avg} is the average lifetime, the τ_i is the i th lifetime component and a_i is the corresponding amplitude.

To estimate the apparent K_D a plot of τ_{avg} vs Importin β concentration was fitted to equation 3.22.

Equation 3.22

$$\tau_{avg} = \frac{[Importin\beta]}{([Importin\beta] + K_D)} \times (\tau_{avg(bound)} - \tau_{avg(free)}) + \tau_{avg(free)}$$

Here $[Importin\beta]$ represents the concentration of Importin β , τ_{avg} is the average lifetime of acrylodan for different Importin β concentrations, $\tau_{avg(bound)}$ and $\tau_{avg(free)}$ represent the average lifetimes in completely bound and free states respectively and K_D represents the apparent binding constant. While the $\tau_{avg(bound)}$ value was obtained from the fit $\tau_{avg(free)}$ value was fixed to that for the free Nup153FG samples. This equation is based on a model that assumes excess of Importin β and a constant Nup153FG concentration during the titration^{100,25}.

3.2 Materials

3.2.1 List of commonly used chemicals

Commonly used chemicals	
Imidazole	Sigma (I5513)
1,4- Dithiothreitol (DDT)	biomol (04010)
2-Mercaptoethanol	Aldrich (M6250)
Complete EDTA free (Protease inhibitor cocktail tablets)	Roche (11873580001)
Magnesium acetate tetrahydrate	Sigma-Aldrich (M2545)
Triton X-100	AppliChem (A1388.0500)
Urea	Merck (1.08487.1000)
Chloramphenicol	AppliChem (A6435)
Ampicillin-sodium salt	AppliChem (A08390025) 25 g
Chitin Resin	NEB (S6651)
His-Pur Ni-NTA Resin	ThermoScientific (88223)
Sodium acetate anhydrous	Merck (1.06268.1000)
Dimethylsulfoxide (DMSO)	Merck (1.02931.0161)
N,N-Dimethylformamide (DMF)	SigmaAldrich (40248)
Acetonitrile (0.1% TFA)	Roth (CP02.1)
Trifluoroacetic Acid (TFA)	Sigma (302031)
L(+)-Arabinose	Roth (5118.2)
Isopropyl β -D-1-thiogalactopyranoside	Biomol
(Tris(2-carboxyethyl)-Phosphine Hydrochloride (TCEP)	Thermo scientific (20491)
Guanidine hydrochloride	USB (75823 500 GM)
4-Acetylphenylalanine (AcF)	Synchem
EDTA (0.5 M EDTA, pH 8)	Ambion (AM9261)
phenylmethylsulfonyl fluoride (PMSF)	Biochemica (A0999.0025)
Glycerol	Merck (1.04093)

3.2.2 List of SEC columns and concentration devices used for protein purification

SEC columns and concentration devices used for protein purification	
Superdex 200 (10/300) SEC column	GE Healthcare
Superdex 200 (16/600) SEC column	GE Healthcare
Superdex 75 (10/300) SEC column	GE Healthcare

Amicon Ultra 0.5 mL Centrifugal Filters (3kDa molecular weight cutoff)	Merk-Millipore
Amicon Ultra 4 mL Centrifugal Filters (3kDa molecular weight cutoff)	Merk-Millipore
Corning Spin-X UF 20 mL Centrifugal Concentrator (5kDa molecular weight cutoff)	CORNING(431487)

3.2.3 List of solvents used in spectroscopy

Solvents used for spectroscopy	
PBS 10x pH 7.4	Gibco (70011-036)
Water	Sigma-Aldrich (270733-2L)
Methanol	Sigma-Aldrich (1.06002)

3.2.4 List of synthetic fluorescent dye

Fluorescent dyes			
Dye	Reactive Group	Reactive towards	Manufacturer
Alexa488	maleimide	thiols	Invitrogen (A10254)
Alexa594	maleimide	thiols	Invitrogen (A10256)
Alexa488	hydroxylamine	aldehydes and ketones	Invitrogen (A30629)
Acrylodan	α,β -unsaturated carbonyl	thiols	Invitrogen (A433)
Bis-ANS	NA	NA	Sigma-Aldrich (D4162)
Coumarin153	NA	NA	Sigma-Aldrich (01511)
Rhodamine-6G	NA	NA	Sigma-Aldrich (252433)

3.2.5 List of commercial kits

<u>Commercial kits</u>	
Commercial kits	Manufacturer
BCA Protein Assay Kit	ThermoScientific (23227)
Quick Plasmid Miniprep Kit	Invitrogen (K210011)
Quick Gel extraction kit	Invitrogen (K210012)
Quick PCR purification kit	Invitrogen (K310002)

3.2.6 List of *E.Coli* strains

<u><i>E.coli</i> strains</u>		
Strain type	Features	Manufacturer
<i>E.coli</i> BL21 (DE3) AI	Harbours araBAD which is an arabinose inducible promoter upstream of T7 RNA polymerase. Gene used in protein expression	Invitrogen
<i>E.coli</i> XL10 Gold cells	High transformation efficiency with large plasmids, can also serve as expression host strain for large plasmids and for for protein expression	Stratagene

3.2.7 List of specialized software

<u>List of special software</u>	
Igor Pro	Wavemetrics
SymPhoTime	PicoQuant
PyMol	Schrödinger
SnapGene	GSL Biotech LLC
Image Lab 5.2.1	Bio-RAD
EndNote	Clarivate Analytics

Chapter 4

4 Results

The result chapter is divided into four broad sections. I first describe the construction of the Time Correlated Single Photon Counting (TCSPC) setup that I have built for picosecond resolved fluorescence studies and dynamic characterisation of IDP complexes. Then I describe my experimental results about an IDP complex (IBB-Importin β) formed by coupled-folding binding mechanism. Subsequently, I describe my results about a complex formed by fuzzy complex formation mechanism (Nup153FG-Importin β) and finally I describe additional results for a different complex (NSP1FG-Importin β) formed by fuzzy complex formation mechanism to verify generality of the observations in fuzzy complexes.

4.1 Building and characterization of the TCSPC setup

4.1.1 Construction of the TCSPC setup

For measuring time-resolved fluorescence, I constructed a TCSPC spectrometer. The three essential components of a picosecond TCSPC spectrometer are a picosecond pulsed excitation source, a photon detector with single photon sensitivity and timing electronics with picosecond resolution. For the excitation source I used a QuixX 405 nm picosecond pulsed laser (Omicron, Germany) that produces picosecond pulsed (~ 80 ps) output of up to 200 μ W (average power) and variable frequency (1-40 MHz). For a photon detector with single photon sensitivity I used PMA Hybrid detector (PicoQuant, Berlin). For timing electronics and data acquisition I used Hydrharp400 which is an integrated TCSPC counting module (PicoQuant, Berlin). The whole setup was constructed with an 8 cm beam height on an optical table (See Figure 4.1). The laser pulse was passed through a Glan-laser polarizer (Thorlabs) and was used to excite the sample in cuvette holder. The emission path perpendicular to the excitation path consisted of another Glan-laser polarizer (Thorlabs), passed through a monochromator (repurposed from a PTI fluorimeter), and focused on the detector through a 4 mm lens (Thorlabs). The part of the setup consisting of the laser, polarizers and the cuvette holder was placed in a light tight black coloured box. The box door also had an interlock circuit which automatically switched off the detector when the door was opened. The monochromator window reached inside the box and the junction was made light tight. The relative small phase mismatch between two polarizers at the same angle was pre-calibrated by passing a linear polarized light from a laser concurrently through the two polarisers and changing the angle of one until maximum intensity could be recovered; the final polarizer angle used for all the measurements took this mismatch into account. My measurements involved wavelength dependent time resolved fluorescence. Hence for proper chromatic separation of the fluorescence signal the slit width of the monochromator was set to only ± 2 nm. The setup was built keeping in mind that biologically labile systems would be measured and hence fast measurements at low concentrations were essential. With a

high repetition rate (30-40 MHz) of the laser, measurements could be made at rather high count rates of ~200 kcps without the problem of photon pile-up.

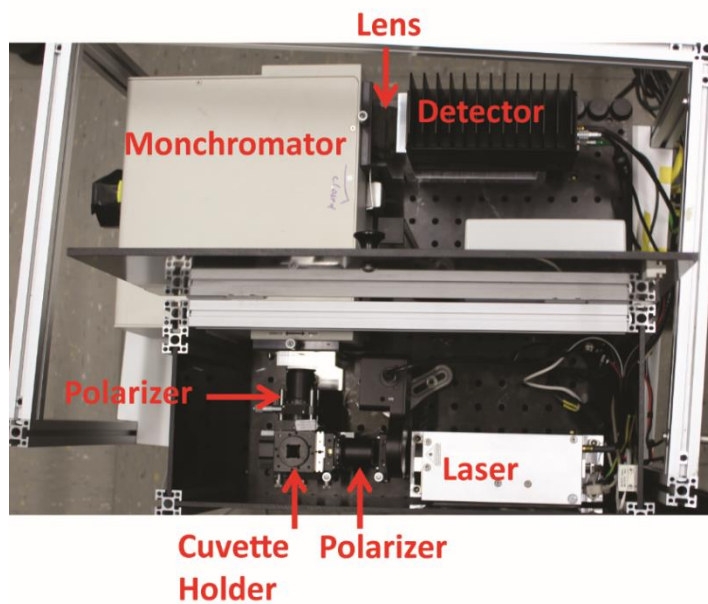
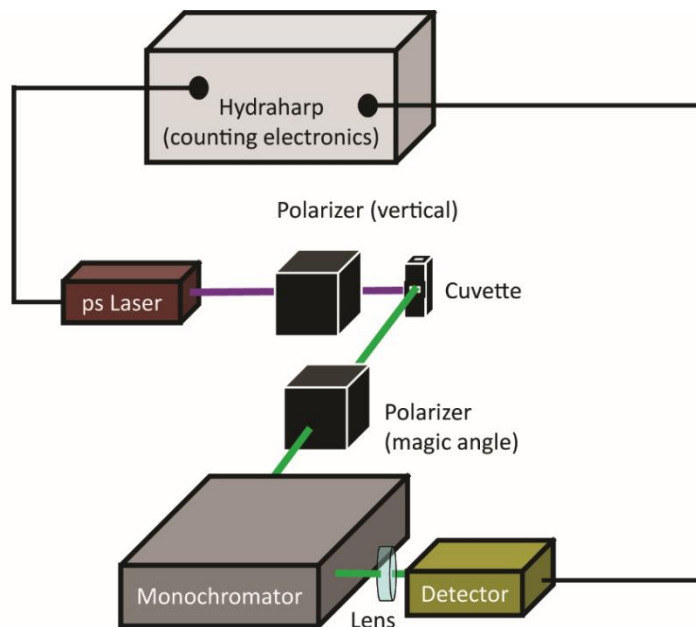


Figure 4.1 Schematic and photograph of the TCSPC setup: Schematic of the TCSPC setup (top) with all the components, the excitation source, the optical path and the detectors. Photograph of the setup (bottom) showing the corresponding components.

In my setup measurement of a fluorescence decay trace with a peak count of 30000 photons using 500 nM acrylodan labelled sample could be measured in ~2-3 minutes.

4.1.2 Characterisation of the TCSPC setup

To characterise the temporal resolution of my TCSPC setup I measured the instrument response function of the setup by measuring rayleigh scattering from a colloidal ludox solution at the excitation wavelength (See Figure 4.2). Since scattering is an instantaneous response the finite temporal width/profile of an IRF originates solely from component of the TCSPC such as the width and shape of the laser pulse, the timing electronics and the optics. The IRF describes the narrowest temporal profile experimentally accessible by a TCSPC. The IRF, in the system I built had an fwhm (full-width at half maxima) of ~125 ps; it had the shape of an asymmetric peak that tails to longer times. The fwhm of the TCSPC was consistent within $\pm 15\%$ of the mean value over different measurements. The fwhm of the IRF determines the minimum value of the time component resolvable from a fluorescence decay, via iterative deconvolution, as $\sim 1/10$ of the IRF fwhm. However, it is to be noted that this is a very optimistic estimate and the actual resolvable shortest time component might be larger specially for complex multiexponential decays and hence more conservative estimates for the time resolution of a TCSPC setup is considered to be approximately equal to IRF fwhm or half of the IRF fwhm.

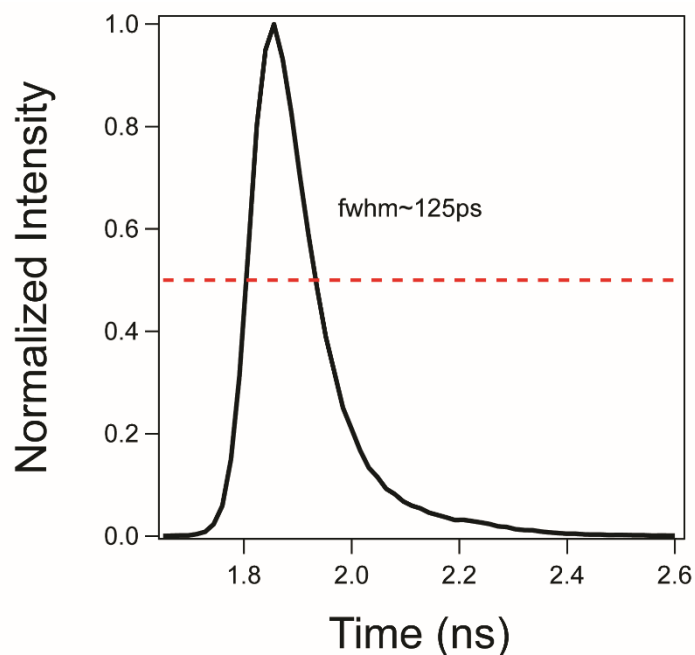


Figure 4.2 IRF of the TCSPC setup: The IRF of the TCSPC setup measured with a suspension of 1% ludox in water at 400 nm at count rate of 5 kcps. The IRF had a asymmetrical profile with an fwhm of ~125 ps.

To validate my measurement and analysis pipeline for solvation dynamics, I decided to measure solvation dynamics on a simple system for which solvation dynamics measurements had been made with a setup having a comparable time resolution as the one I built; this was very crucial for proper comparison as the amount of solvation dynamics captured experimentally depends on the time resolution of the setup. Solvation dynamics of the coumarin dye C153 (Coumarin153) in Triton-X micelles was found to be a system that fulfilled the mentioned criteria. Our experimental data on this system was found to be in close agreement with previous reports, as our measured $C(t)$ function overlapped well with the published references (See Figure 4.3)^{169,170}. The small offsets between the three curves originated likely from the time t , where $v(t)$ was taken to be $v(\infty)$ to construct the normalized $C(t)$.

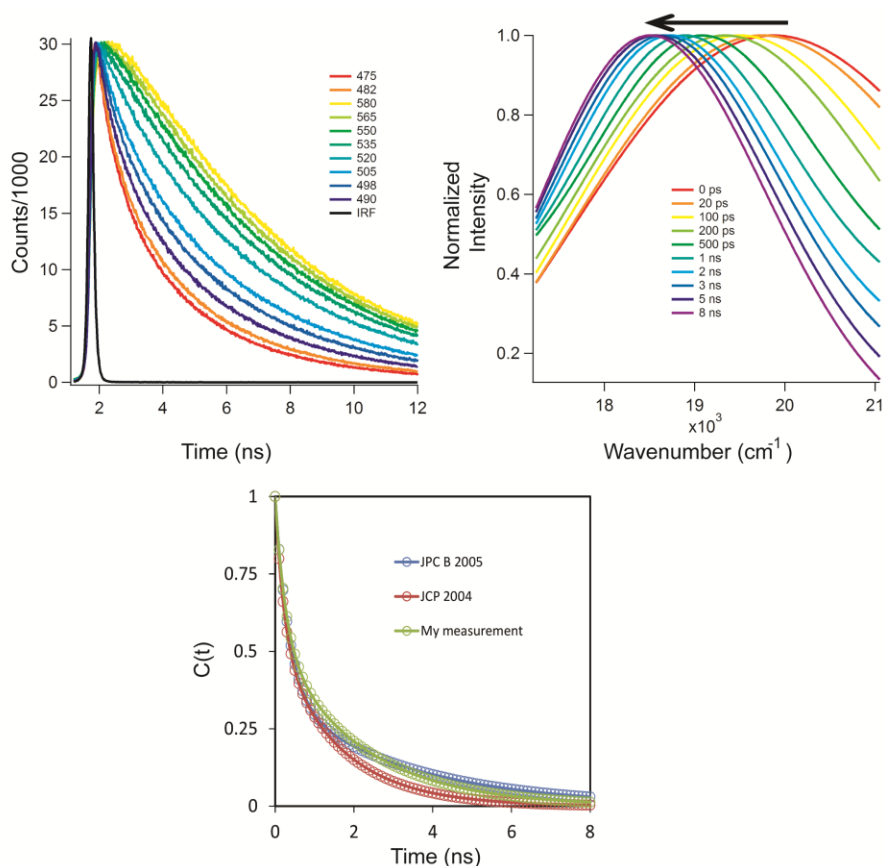


Figure 4.3 Solvation dynamics of C153 in Triton-X micelles: Wavelength dependent decays showing fast decays at bluer wavelength and slower decays with rise at redder wavelengths (top left). The reconstructed TRES showing constant frequency shift to lower frequencies with time (top right). The obtained $C(t)$ compared with those reported in literature (from ref [169] and ref [170]) for the same system by the same lab showing a good match.

4.2 Dynamic characterization of an IDP complex formed via coupled folding and binding

For an IDP system that undergoes complex formation via coupled-folding binding mechanism, I chose the IBB-Importin β system. Here IBB (Importin β binding) domain constitutes the disordered N-terminal part of Importin α which undergoes a folding transition forming a helix upon binding its partner Importin β . I have first described the characterization of this complex using multiparameter smFRET and FCS. Subsequently, I characterized the interfacial environment in the IBB-Importin β complex, using site-selective steady state and time-resolved fluorescence spectroscopy. Finally, I used time resolved fluorescence spectroscopy to characterize the time scales of surface solvation on IBB in free and Importin β bound state and to see how binding its partner modulates the nature and the dynamics of solvation by probing the interfacial solvation dynamics in the IBB-Importin β complex.

4.2.1 Single molecule studies of IBB recognition by Importin β

smFRET probes FRET between two points in a protein where the donor and acceptor labels are positioned. Owing to the distance dependence of FRET in the range of $\sim 2 - 10$ nm, it serves as a proxy for conformational change for biomolecules and is aptly described as a ‘molecular ruler’¹⁶⁰. I generated a double cysteine IBB mutant IBB S24C/S55C where the two cysteine residues were positioned near the ends of the helix that was formed when IBB bound Importin β . Donor and acceptor dyes (Alexa488 and Alexa594) were conjugated randomly to these residues via maleimide chemistry. This would allow one to directly monitor the disorder to helix transition via FRET when IBB would bind Importin β .

I used the PIE excitation scheme as it allowed me to directly interrogate acceptor molecules in each molecule. I performed multiparameter smFRET data with PIE excitation combined with burst wise analysis on double labelled IBB S24C/S55C samples. The data presented as 2D histograms of stoichiometry S vs FRET efficiency (E_{FRET}) showed two major populations in all the conditions (See Figure 4.4). One population appearing at around $S=1$ and $E_{\text{FRET}}=0$, and originating from molecules that lacked an active acceptor dye molecule is termed the ‘donor only’ population. The other population at around $S\sim 0.5$ and varying E_{FRET} originated from molecules that had both the donor and the acceptor dyes and thus carried FRET information; this population was used to monitor changes in E_{FRET} in different conditions.

Free IBB in solution showed a high E_{FRET} 0.79, which was consistent with a short (31aa) separation between the donor and acceptor in a disordered protein. In presence of Importin β there was a shift in the E_{FRET} from 0.79 to 0.37. Such a large E_{FRET} shift suggested a change in distance and thus a conformational change upon Importin β binding; reduction in E_{FRET} efficiency

implied the conformational change was associated with an increase in distance between the two labelling sites.

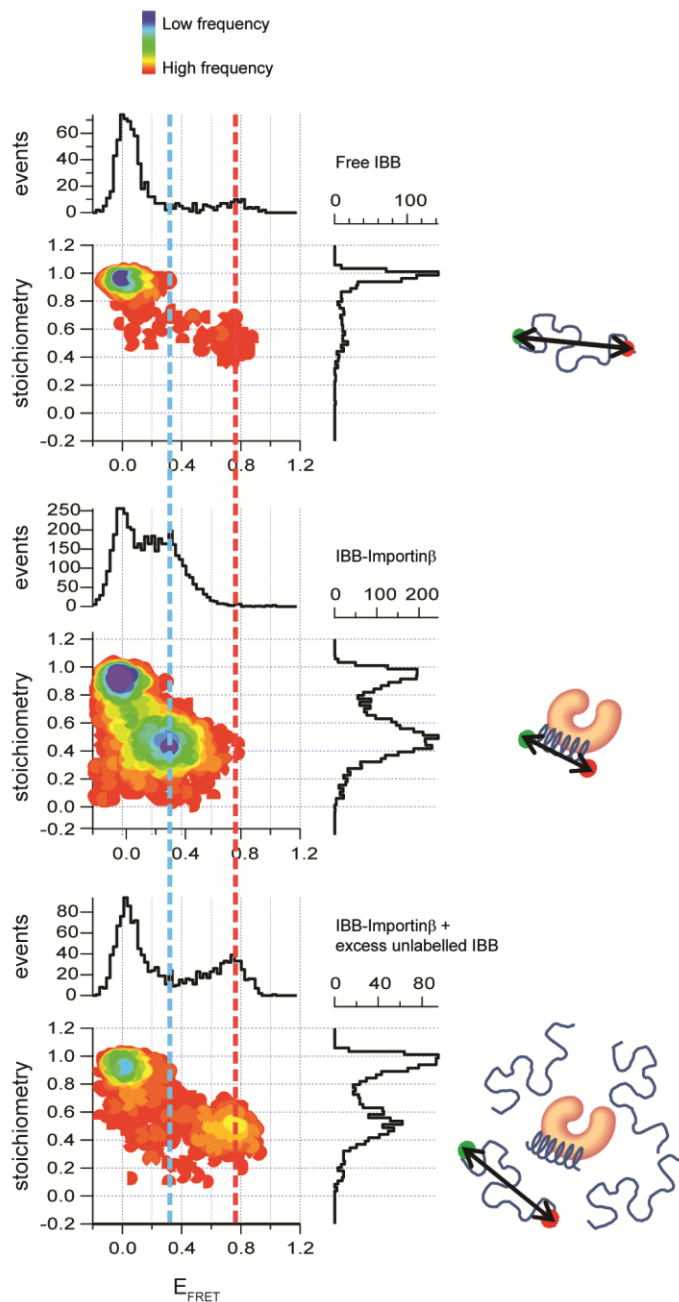


Figure 4.4 smFRET to probe IBB-Importin β interaction: The smFRET data is represented as 2D histograms of S vs E_{FRET} where populations corresponding to $S \sim 0.5$ represent molecules where FRET is happening. In free IBB the E_{FRET} is 0.79 and represents the distance between the labelling positions in the disordered IBB (top). In presence of 1 μM Importin β IBB undergoes a coil to helix transition, this results in a change in E_{FRET} to 0.37 (middle). When a preformed complex of IBB and Importin β is diluted with excess Importin β (5 μM) the E_{FRET} value is shifted to that of free IBB (bottom).

From this data one could not assess directly the kinetic stability of the complex or the binding affinity. One could however say that the binding is in the nanomolar range as I saw no populations corresponding to the unbound state in presence of just 1 μM Importin β ; and I could also say that the half-life of the complex was higher than the timescales of diffusion across the confocal volume, which was typically ~ 1 ms, based on the fact that I could clearly resolve bound and unbound populations which would not be possible in case the disassociation half-lives were faster. Next to assess the specificity of this conformation change I performed smFRET experiments after diluting double labelled IBB S24C/S55C pre-incubated with Importin β in excess unlabelled IBB. In the presence of the excess unlabelled IBB the FRET efficiency of the sample recovered to the value of the unbound IBB (See Figure 4.4 bottom). This proved that the E_{FRET} shift in IBB was due to a biochemically specific interaction with Importin β which was reversible with excess IBB.

E_{FRET} changes represent changes in distance between the donor and the acceptor, with a decrease in E_{FRET} implying an increase in distance. For IBB-Importin β interaction the FRET efficiency shifted to a lower value upon Importin β binding corresponding to an increased separation between the two labelling points. To evaluate whether a coil to helix transition, which happens to be the conformational change associated with IBB-Importin β interaction, involved extension in end to end distance, I simulated rms (root mean squared) end to end distance for a statistical coil, which is a fairly apt representation for end to end distances in IDPs, and a helix (See Figure 4.5).

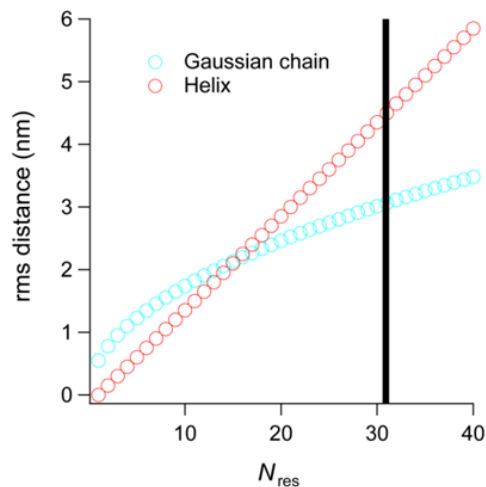


Figure 4.5 rms distance of a model Gaussian chain and a helix: The rms end to end distance is plotted as a function of the number of residues (N_{res}) time (top right). The black line represents the N_{res} value for IBB smFRET construct and shows that for that sequence length a gaussian chain is shorter than the helix.

For a statistical coil representation of free IBB, I chose a Gaussian chain model with a Flory exponent $\nu=0.5$ based on previous studies.⁶⁶ At a residue separation of 31aa, which was the separation between the FRET labels in IBB, the rms distance of a helix happened to be ~ 1.5 nm longer than that of a Gaussian chain. This was thus in perfect agreement with a decrease in E_{FRET} in double labelled IBB S24C/S55C upon Importin β binding. It has to be noted that direct comparison of distance in the bound helical state with the crystal structure is not straightforward here primarily for the fact that one of the labelling positions in IBB was one residue later than the last residue resolved in the crystal structure.

Finally, I extracted FCS traces from the smFRET data (See Figure 4.6). For the FCS data only the acceptor signal resulting from the acceptor laser pulse was used. Owing to an underfilled objective in our setup the focal volume is extended in the z direction and in such a setup the FCS data could be approximated to be originating from 2D diffusion. Free IBB showed a diffusion time of ~ 0.26 ms. In presence of Importin β the diffusion time changed to ~ 0.40 ms suggesting a large change in molecular weight which would be in line IBB (~ 10 kDa) complex formation with Importin β (80 kDa).

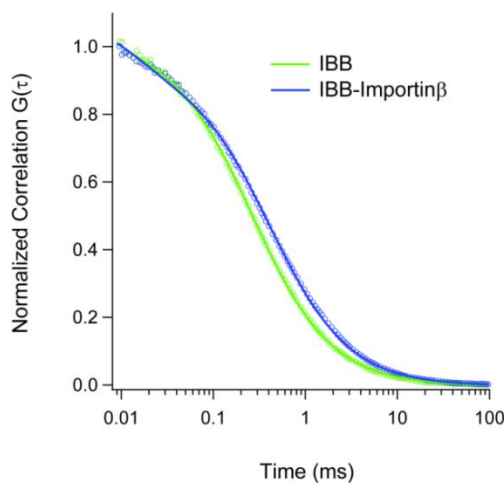


Figure 4.6 FCS of IBB-Importin β recognition: Normalised FCS of IBB (green) and IBB with Importin β (blue). The solid lines represent fits to data with a 2D diffusion model with a triplet state.

4.2.2 Probing IBB-Importin β interaction with acrylodan fluorescence

I generated a single cysteine mutant IBB S24C, where the cysteine was positioned at the base of the helix which is formed upon recognition of IBB by Importin β , to probe the recognition of IBB by a fluorescent probe (Figure 4.7). Acrylodan was conjugated to this single cysteine mutant as an environment sensitive local fluorescent reporter. Acrylodan fluorescence emission is highly

sensitive to local polarity and is thus a very good reporter of the local microenvironment¹⁶⁸. Acrylodan emission on free IBB had its maximum around 527 nm consistent with the location of the probe on a solvent exposed site on an IDP¹⁷¹. Upon Importin β binding the emission spectra showed a dramatic change, undergoing a blue shift of almost 30 nm to a maximum at 501 nm; the intensity of the emission also increased by ~ 3 fold (See Fig 4.7). The blue shift of the emission spectra indicated that upon Importin β binding the IBB-Importin β interface was less polar than the free IBB surface. This reduced polarity likely stemmed from desolvation effects associated with Importin β binding. The desolvation effects also explained the intensity increase upon Importin β binding; desolvation produces a less polar environment and for many solvation sensitive dyes including prodan which is closely related to acrylodan, reduced solvent polarity causes an increased quantum yield^{172,173}.

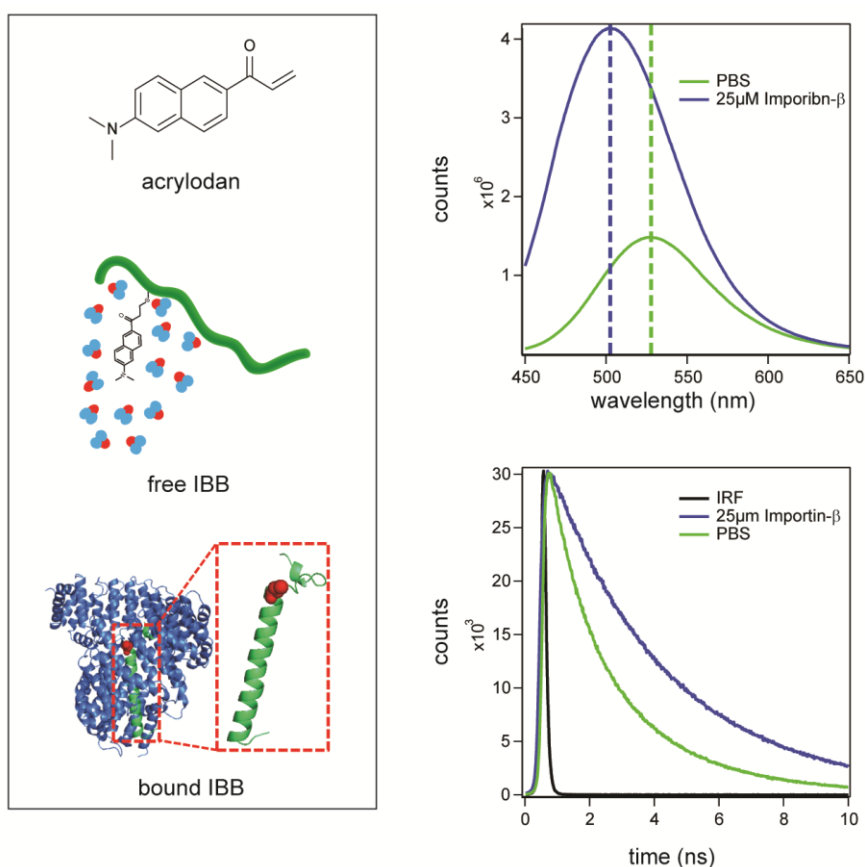


Figure 4.7 Acrylodan emission and lifetime in IBB-Importin β interaction: A schematic of acrylodan, its labelling position in the context of the structure of IBB-Importin β complex is shown (Left). Steady state emission shows the emission spectra in PBS (green) to be blue shifted in presence of Importin β (top right). Lifetime data of acrylodan in presence (blue) and in absence (green) of Importin β (see bottom right).

The average lifetime of acrylodan labelled IBB S24C measured at 535 nm increased 1.5 fold from 2.85 ns to 5.15 ns, upon Importin β binding. The acrylodan lifetime increase also reflected

desolvation at the interface of the IBB-Importin β complex. Desolvation induced lifetime increase corresponded to the steady state intensity increase and suggested a suppression of non-radiative pathways in a less polar milieu, as has been known for other solvation sensitive probes¹⁷³. The precise molecular mechanisms responsible for suppression of non-radiative pathways in less polar environments can be complex and is usually idiosyncratic of the probe photophysics in question¹⁷³.

To get a more qualitative picture of the extent of desolvation that IBB underwent upon Importin β binding, I tried to estimate the local polarity quantitatively by assessing the local relative permittivity change upon Importin β binding. Taking spectral data from literature for acrylodan-

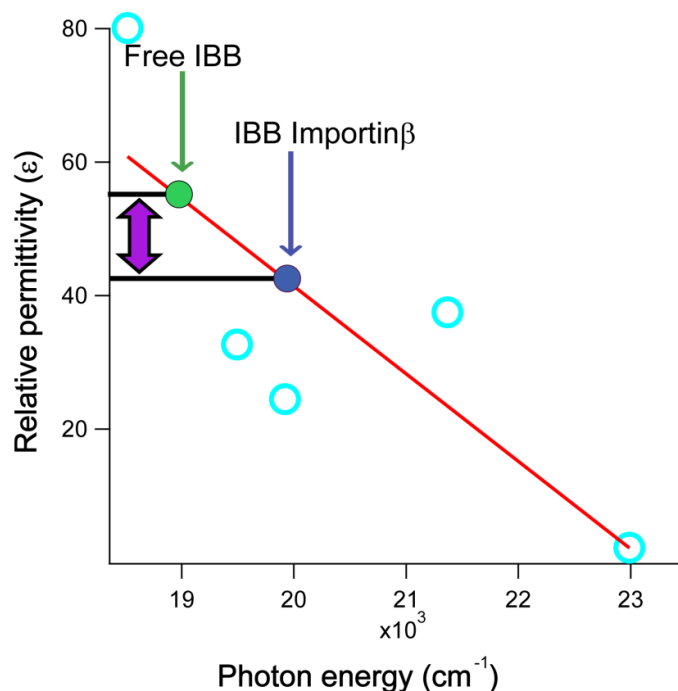


Figure 4.8 Relative permittivity for IBB in presence and absence of Importin β : The peak frequencies (cyan open circles) of acrylodan-2-mercaptoethanol conjugate in different solvents [from ref 168] is plotted against the relative permittivity of those samples. The red line represents a linear fit through the data. The relative permittivity experienced by acrylodan in unbound IBB (green solid circle) and in presence of Importin β (blue solid circle) is obtained from the emission peak frequencies using the equation for the linear fit of the relative permittivity vs emission frequency of acrylodan-2-mercaptoethanol ($\epsilon_r = -0.013\nu_{\max} + 304$ where ϵ_r and ν_{\max} are the relative permittivity and emission maximum frequency in cm^{-1} respectively). The data shows decreased relative permittivity of IBB bound to Importin β compared to free IBB.

2-mercaptoethanol conjugate in different solvents¹⁶⁸, I found that acrylodan emission peak frequency maximum showed a nice correlation with the polarity of the solvent (See Figure 4.8),

expressed through the relative permittivity with lower emission frequencies for more polar solvents (higher relative permittivity). Comparison of the emission frequencies of free IBB and IBB in presence of Importin β with that of acrylodan-2-mercaptoethanol in different solvents provided a rough estimate of relative permittivity and consequently polarity; with higher relative permittivity indicating a more polar environment and lower relative permittivity indicating a less polar environment. A similar approach was used to estimate local relative permittivities for an ATPase in different membrane environments with a local probe badan which is similar to acrylodan¹⁶⁷. Acrylodan-2-mercaptoethanol conjugate is most closely related to cysteine-acrylodan in a protein environment. From such an analysis a rough estimate of relative permittivity was obtained for free IBB and in the presence of Importin β ; for the latter there was a decrease of relative permittivity by ~ 11 units to 43 from 52 which was the value estimated for free IBB. The decrease in relative permittivity indicated a less polar microenvironment which is in line with a hydrophobic desolvated interface in IBB-Importin β .

4.2.3 Probing solvation dynamics at IBB surface and the IBB-Importin β interface

After having probed the interaction of IBB with Importin β with smFRET, FCS and site selective acrylodan fluorescence, I ventured to measure the solvation dynamics on IBB surface site selectively with IBB S24C labelled with acrylodan. For measurement of solvation dynamics the lifetime decays were measured at several wavelengths spanning the emission spectra. For systems where solvation dynamics occur the lifetime decays show a striking wavelength dependence with decays being very fast at the blue end of the spectrum and becoming progressively longer as one moves towards the red end of the spectrum. This was indeed the case for IBB S24C where the acrylodan decays became progressively longer with the wavelengths (See Figure 4.9). The lifetime data obtained at different wavelengths were used to reconstruct the TRES which showed a progressive shift towards lower frequencies with time. The maximum frequencies of the TRES at different time points were used to construct the solvent response curve (See Fig 4.9).

The solvent response of free IBB appeared to be clearly bimodal with a large part of the stokes shift of the TRES happening in under 500 ps followed by slower relaxation happening in nanosecond timescales. The data was thus fitted to a bi-exponential. The time constants recovered were 43 ps and 1 ns. The faster picosecond component likely originated from surface water dynamics on the IBB surface and the nanosecond component was supposedly from slower modes of relaxation from the protein or even from the dye photophysics¹⁵⁹. This assignment was based on extensive studies on protein solvation dynamics using tryptophan as a probe where it was shown that protein solvation relaxation timescales did not typically go beyond hundreds of picoseconds^{140,137,145,139}. It should however be noted that the 43 ps component is slightly below the time resolution of the TCSPC setup that I used.

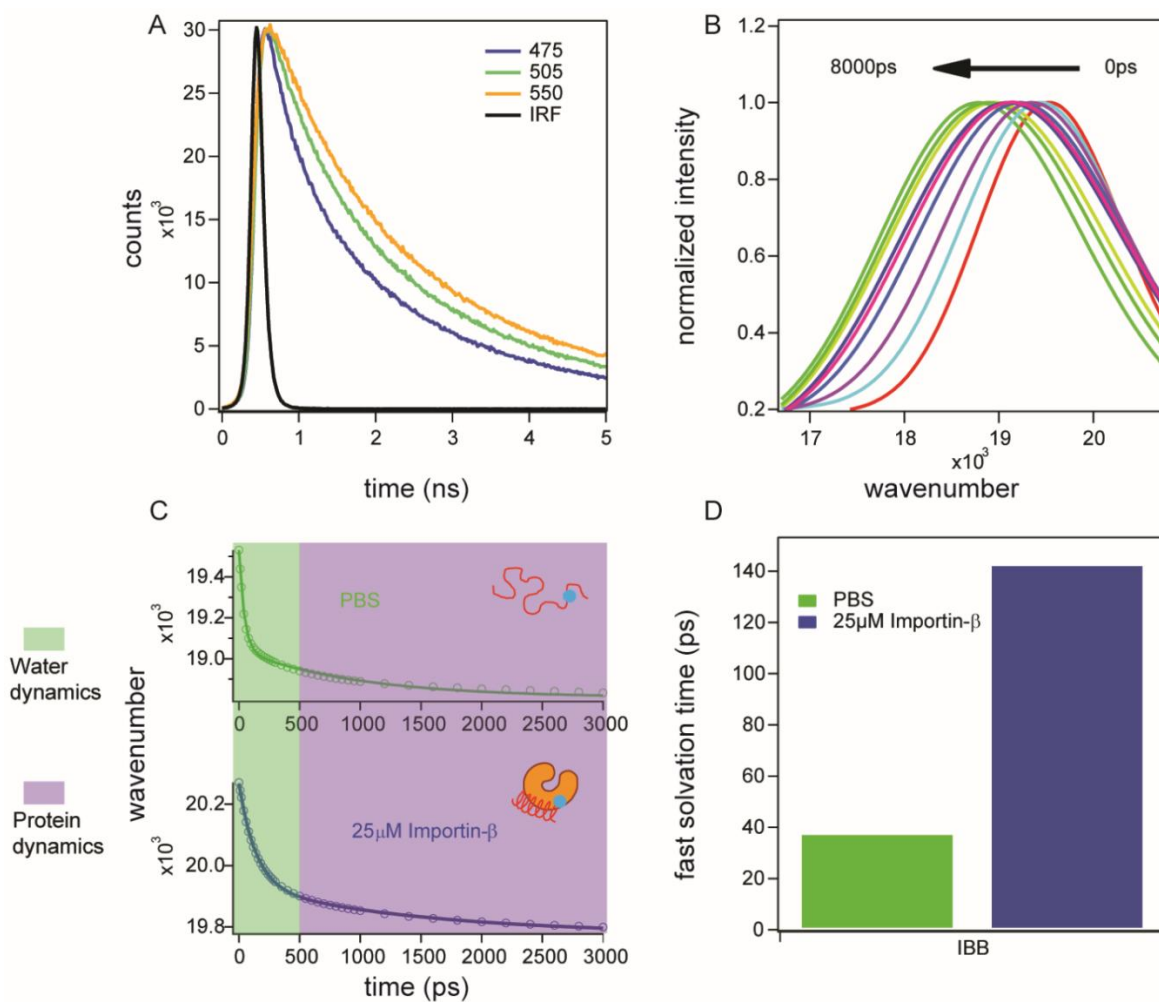


Figure 4.9 Solvation dynamics of IBB in presence and absence of Importin β : The solvation dynamics in IBB is measured by measuring lifetime decays at different wavelengths. The decays for free IBB are wavelength dependent (top left) where representative decays at 475 nm, 505 nm and 550 nm are shown and the decays become longer with increasing wavelengths. TRES is constructed from the fits of the decays. Representative TRES of free IBB is shown (top right) where the spectra progressively moves to lower frequencies with time. The solvent response curve (bottom left) is obtained by plotting the frequency maxima of the TRES obtained at different time points as a function of time. The solvent response curves for free IBB (in green) and IBB-Importin β complex (blue) are shown with the solid lines representing bi-exponential fits. The shaded regions represent parts of the solvent response predominantly originating from water (light green) and protein (purple) dynamics. The fast time component of the solvent response that represents water dynamics is shown for IBB and IBB-Importin β complex (bottom right) as a bar plot. The time constants recovered from two independent measurements were within 15% of each other.

After performing solvation dynamics experiment on free IBB, I performed the same experiments on IBB-Importin β complex. This time the measurements reported on the solvation dynamics at

the IBB-Importin β interface. The solvent response at the IBB-Importin β interface was clearly very different from that in the free IBB (See Figure 4.9). Despite the differences, the solvent response in this case was also fundamentally bi-modal and was thus analysed by a bi-exponential like in the case of free IBB. The fast component of the solvent response arising from water dynamics underwent a ~ 3 fold slowdown compared to free IBB and became 138 ps (See Table 4.1). This slowdown was confirmed from two independent measurements and the values recovered were 15% of each other. The steady state acrylodan fluorescence had revealed that the IBB-Importin β interface is more hydrophobic and desolvated compared to the free IBB surface. The dynamics measurements thus revealed that the water molecules in the IBB-Importin β interface were dynamically constrained and more ordered compared to those on the free IBB surface. This ordering of the water molecules at the interface might have implications for the formation and stability of the IBB-Importin β complex.

Table 4.1: The values obtained from bi-exponential fits of the solvent response curve for IBBS4C

System	τ_1 (ps)	Normalized a_1	τ_2 (ns)	Normalized a_2
IBB	43	0.34	1.0	0.66
IBB S24C+ Importin β	138	0.67	1.5	0.33

4.3 Dynamic characterisation of an IDP complex formed via a fuzzy binding mechanism

For an IDP system that undergoes complex formation via a fuzzy binding mechanism I chose the Nup153FG-Importin β system as an example for FG-Nup-NTR complexes. That Nup153FG forms a fuzzy complex with Importin β had been well established in a previous collaborative study led by our group employing multiple techniques such as smFRET, MD simulations, NMR and stopped flow spectroscopy²⁵. The said study showed that Nup153FG interacts with Importin β forming a fuzzy complex without any conformational change via an ultrafast, diffusion limited binding mechanism. I have first described the characterisation of this complex using site selective acrylodan fluorescence spectroscopy on four Nup153FG cysteine mutants, probing different regions of Nup153FG with different sequence propensities, and characterized the local binding propensities with Importin β and the interfacial environment in the Nup153FG-Importin β complex. Subsequently, I have used time resolved spectroscopy to characterise the time scales of surface solvation on Nup153FG and seen how Importin β binding modulated the nature and the dynamics of solvation by probing the interfacial solvation dynamics in the Nup153FG-Importin β complex.

4.3.1 Probing Nup153-Importin β interaction with acrylodan fluorescence

To probe Nup153FG-importin β interaction using site specific acrylodan fluorescence I used four single cysteine mutants spanning the length of the protein. Nup153FG consists of a PxFG rich region near the C terminal region and a FxFG rich region in the N terminal region. The PxFG rich region is abundant in PxFG motif while the FxFG rich region is abundant in FxFG motif. The mutants used were 883C, 990C in the FxFG region and 1330 and 1355 in the PxFG region. In a previous study from our lab, these two regions had been probed extensively using experimental approaches such as smFRET and stopped-flow spectroscopy establishing fuzzy complex formation with NTRs²⁵. Acrylodan labelled single cysteine mutants of Nup153FG in unbound state showed an emission maxima centered around ~530 nm indicating solvent exposure of the probe (See Fig 4.10). This is expected for a fluorophore on a free IDP surface and it also highlighted that the microenvironment in different stretches of Nup153FG were rather similar. In the presence of Importin β the emission spectra of Nup153FG changed remarkably showing an intensity increase of ~2 fold and a blue shift of ~25 nm. The nature of the spectral shift of Nup153FG mutants upon binding Importin β was similar to the spectral shift obtained when Importin β formed a complex with acrylodan labelled IBBS24C. Acrylodan emission is very sensitive to microenvironment polarity; the emission becomes progressively blue shifted with reduction in environment polarity. Thus the blue shift of acrylodan emission in Nup153FG mutants upon Importin β binding suggested that recognition of Importin β by Nup153 led to the formation of a less polar and hydrophobic interface. Such hydrophobic interfaces in Nup153FG, seen to be formed at all the labelling sites upon Importin β binding, were likely due to desolvation at those sites upon interaction with Importin β . Desolvation of the binding interface in Nup153FG-Importin β complex would also explain the increased acrylodan fluorescence intensity upon Importin β binding; suppression of non-radiative pathways of the excited state in a hydrophobic environment would explain the intensity increase. The reflection of this desolvation was also observed in the acrylodan fluorescence lifetime which typically underwent a 1.5 fold increase upon Importin β binding (See Fig 4.10). The increased lifetime directly demonstrated the decrease of non-radiative relaxation pathways of the excited state in a hydrophobic environment and was thus in correspondence with the steady state intensity increase. For probes like acrylodan such intensity and lifetime increase in hydrophobic environment is known¹⁷².

To have a more quantitative insight into the extent of desolvation upon Importin β binding to Nup153FG I estimated the local relative permittivity values for the different sites in Nup153FG, in free and in Importin β bound conditions (See Figure 4.11). The approach I used was similar to

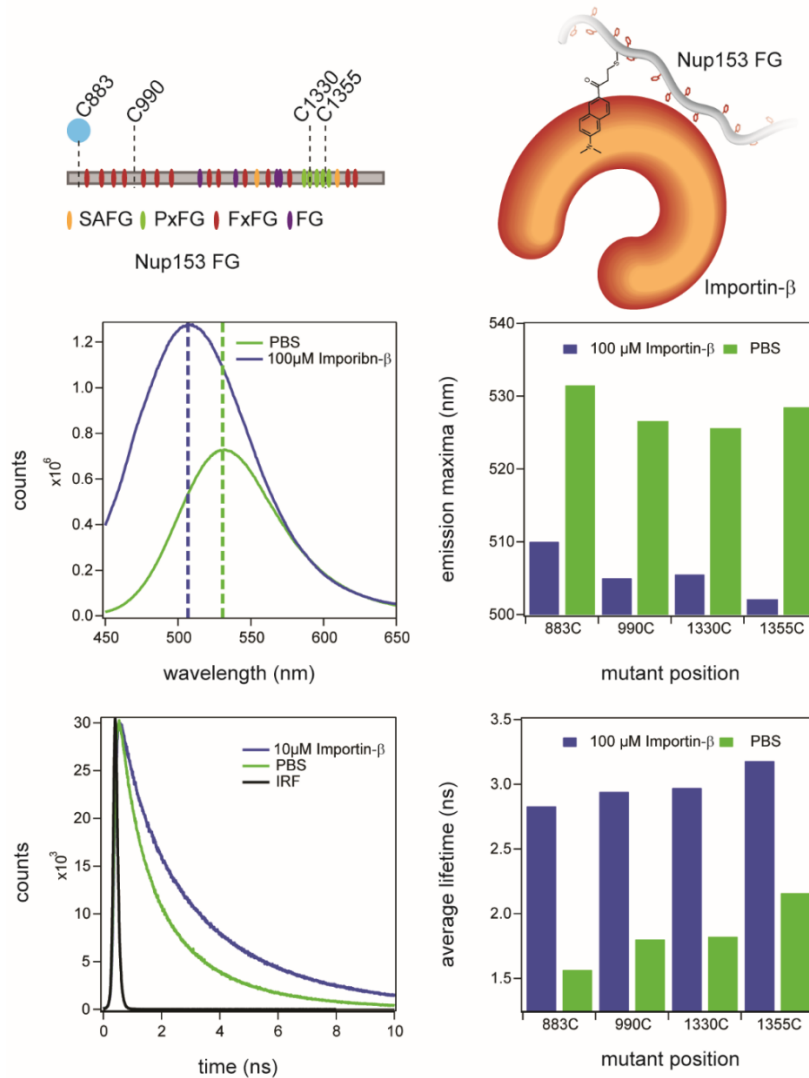


Figure 4.10 Acrylodan emission and lifetime in Nup153FG-Importin β interaction: A schematic showing the labelling position of acrylodan in the context of the sequence of Nup153FG (top left). A schematic showing acrylodan probing the interface of Nup153FG and Importin β (top right). Representative steady state emission for Nup153FG 883C shows the emission spectra in PBS (green line) to be blue shifted in presence of Importin β (middle left). The emission maxima for all the Nup153FG mutants in presence and absence of Importin β shown as a bar plot (bottom right). Representative lifetime decays at 535 nm for Nup153FG 883C in presence and absence of Importin β showing longer lifetime in presence of Importin β (bottom left). The average lifetime for all the Nup153FG mutants in presence and absence of Importin β shown as a bar plot (bottom right).

to that used for IBB where relative permittivity from acrylodan fluorescence was estimated by comparison with frequency maxima of acrylodan-2-mercaptoethanol conjugate in solvents having different relative permittivity values and consequently different polarities.

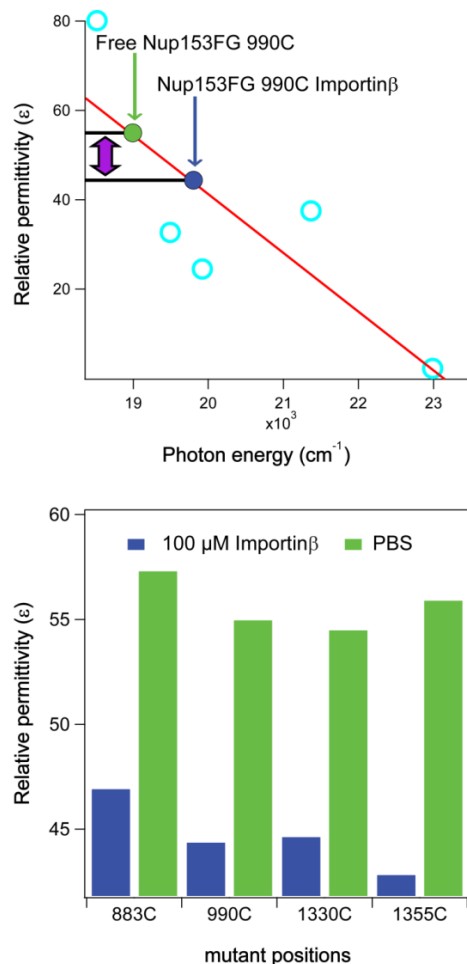


Figure 4.11 Relative permittivity for Nup153FG in presence and absence of Importin β : The peak frequencies (cyan open circles) of acrylodan-2-mercaptoethanol conjugate in different solvents are plotted against the relative permittivity values of those samples (top panel). The red line represents a linear fit through the data. The relative permittivity experienced by acrylodan in unbound 990C (green solid circle) and in presence of Importin β (blue solid circle) is obtained from the emission peak frequencies using the equation ($\epsilon_r = -0.013v_{\text{max}} + 304$ where ϵ_r and v_{max} are the relative permittivity and emission maximum frequency in cm^{-1} respectively) for the linear fit of the relative permittivity vs emission frequency of acrylodan-2-mercaptoethanol, (top panel). The relative permittivity values of all sites in presence and absence of Importin β is shown as a bar plot (bottom panel). The data shows decreased relative permittivity of IBB bound to Importin β compared to free IBB.

The relative permittivity values at different sites showed a typical drop of 10-13 units, depending on the mutants, upon Importin β binding suggesting a less polar interface in the Nup153FG-Importin β complex (See Fig 4.8 and Table 4.2 which tabulates relative permittivity values for the all the mutants).

Table 4.2: The relative permittivity values for the all the Nup153FG mutants with or without Importin β

Systems	Relative permittivity (ϵ)
883C	57
883C + Importin β	47
990C	55
990C + Importin β	44
1330C	55
1330C + Importin β	45
1355C	56
1355C + Importin β	43

Considering the change in relative permittivity to be a reasonably approximate marker for change in polarity, and consequently the extent of desolvation upon partner binding, I could say that the desolvation experienced by both IBB and Nup153FG upon Importin β were quite similar. For Nup153FG Brownian dynamics simulations showed apolar desolvation to be a major driving force for binding²⁵. The Brownian dynamics simulations showed that when the contribution from apolar desolvation was turned off, the association rate constants dramatically dropped indicating energetic gain from desolvation that is release of water molecules to be a driving force for the binding. The experimental evidence for desolvation upon Importin β binding is thus in line with the Brownian dynamics simulation.

4.3.2 Local disassociation constants (K_D) for Nup153FG-Importin β interaction

Unlike most coupled-folding binding IDP systems which involve primarily one to one type of interactions, the interaction of Nup153FG with Importin β is multivalent from the perspective of both Nup153FG and Importin β ; many FG motifs in Nup153FG can engage with different Importin β molecules while Importin β can bind numerous FG motifs on different Nups. Thus the concept of K_D (disassociation constants) for interactions with defined stoichiometry and thus a well-defined equilibrium for the binding, breaks down for this type of a multivalent fuzzy complex. Instead what can be measured is apparent K_D using any observable that changes upon binding of Nup153FG to Importin β . Such apparent K_D is informative about the concentration dependence of binding propensity close to the site being probed. I found that the average fluorescence lifetime increase upon Importin β binding in all the Nup153FG mutants labelled with acrylodan titrated nicely with Importin β concentration. Hence, I titrated acrylodan labelled Nup153FG mutants with Importin β and obtained apparent K_D for the different sites (See Figure 4.12).

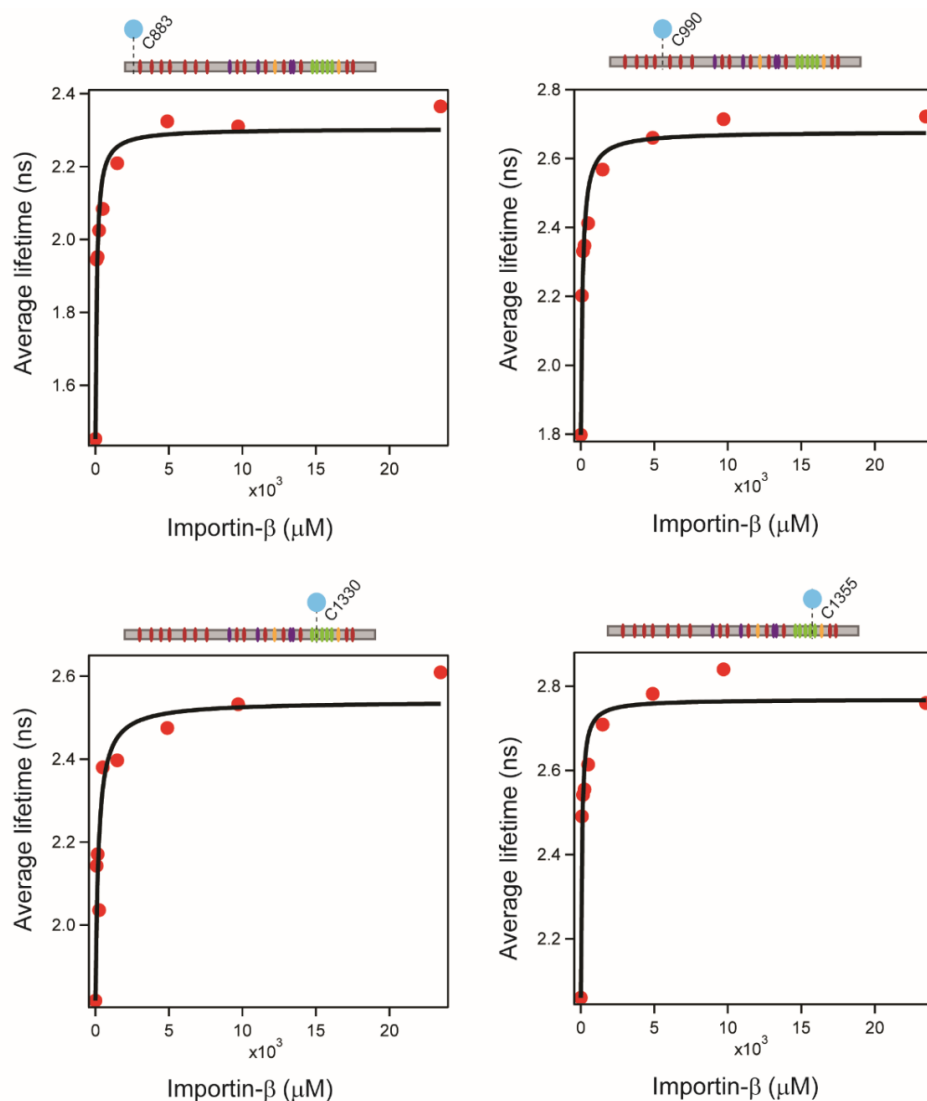


Figure 4.12 Titration of acrylodan labelled Nup153FG mutants with Importin β : Average fluorescence lifetime at 535 nm as a function of Importin β concentration for different acrylodan labelled mutants of Nup153FG mutants, 883C (top left), 990C (top right), 1330C (bottom left) and 1355C (bottom right). A schematic of the Nup153 sequence with the position of the label is shown for each of the titrations. The solid lines represent fit to a binding equation (Equation 3.22) yielding an apparent K_D and absence of Importin β is shown as a bar plot (bottom). The x axis of all the plots have different ranges such that the binding curve is shown clearly; this is to accommodate variations in absolute lifetimes for the different mutants.

The K_D showed a small variation maximum ~ 2 fold between mutants and was in the submicromolar range within ~ 100 - 200 nM (See Table 4.3). Table 4.3 shows the apparent K_D values for the different sites. It has to be noted that owing to the multivalency of the system such low apparent K_D values did not necessarily mean binding interaction was saturated at

concentration when lifetime increase saturated; instead it indicated the concentration where the effect that caused the lifetime changes, likely desolvation effect, saturated.

Table 4.3: The values for apparent K_D s for the all the mutants of Nup153FG

Mutants	K_D (nM)
883C	93 ± 21
990C	120 ± 24
1330C	207 ± 74
1355C	71 ± 17

4.3.3 Site selective chain motions of Nup153FG in the fuzzy complex using time resolved anisotropy measurements.

Considering that in a FG_{Nup}-NTR fuzzy complex there is no conformational change in the IDP, which is the FG_{Nup}, upon partner binding, one indirect way of probing the dynamics of the IDP bound to a partner in a fuzzy complex is via direct interrogation of its local chain dynamics. A very good probe for local chain dynamics or segmental motion of an IDP either by itself or complexed with a partner is time resolved fluorescence anisotropy^{100,174}. Time resolved fluorescence anisotropy measures the kinetics of depolarization of a fluorophore following polarized excitation. It reports on the rotational mobility of a fluorophore in a given environment. For a probe located on an IDP surface time resolved anisotropy typically reports on the local mobility of the fluorophore as well as the time scale of segmental motion arising from rotational dynamics of a segment of the IDP¹⁰⁰ around the fluorophore to which rotational mobility of the fluorophore remains intimately coupled (See Figure 4.13).

Time resolved anisotropy decays were measured for Nup153FG cysteine mutants labelled with acrylodan (See Figure 4.13). For unbound Nup153FG anisotropy decays for all the mutants showed primarily bi-exponential behaviour with a fast component of ~500 ps and a slower nanosecond component of ~5 nanosecond. The fast picosecond component was attributed to free rotation of the fluorophore while the slower nanosecond component was attributed to the segmental motion of the IDP. The effective time window for a given time resolved anisotropy experiment is governed by the lifetime of the fluorophore; this is because anisotropy decays are calculated from fluorescence decays detected at parallel and perpendicular polarization. For acrylodan labelled Nup153FG mutants average fluorescence lifetimes were ~2.5 ns and thus after 10 ns the fluorescence intensity became >10% of the initial value; consequently the time resolved anisotropy signals could be measured only up to ~10 ns after which the data became very noisy. This limited time window often led to some residual anisotropy where the fluorophore did not have sufficient time to undergo complete rotational relaxation during its excited state lifetime. For unbound Nup153FG the residual anisotropy was fairly low (~0.05).

Next I performed anisotropy experiments by adding Importin β which caused a visibly marked change in the anisotropy decays (See Figure 4.13). The decays in this case were also

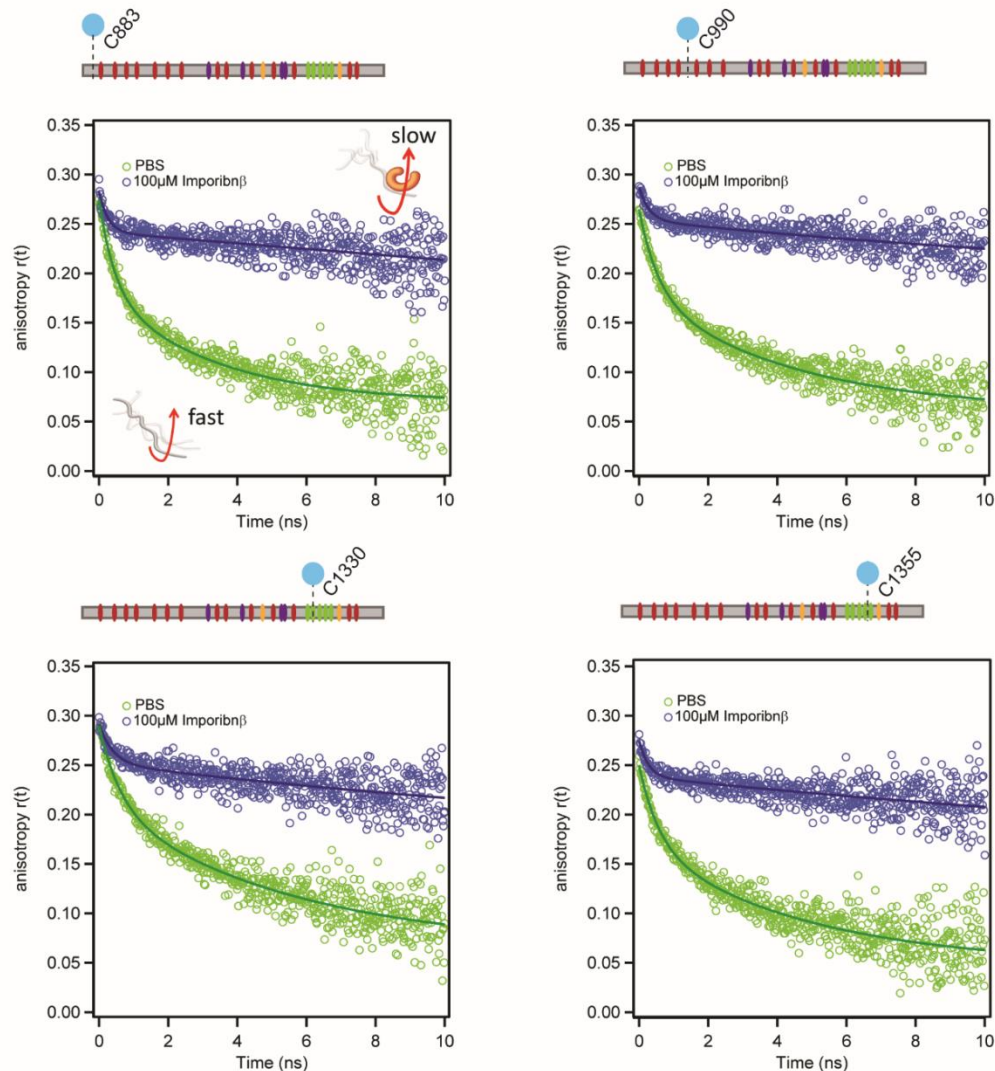


Figure 4.13 Time resolved anisotropy decay of Nup153FG: Time resolved anisotropy decay of acrylodan labelled mutants of Nup153FG mutants, 883C and a schematic showing how binding of a partner suppresses chain dynamics (top left), 990C (top right), 1330C (bottom left) and 1355C (bottom right), in free state (green) and bound state (blue). A schematic of the Nup153 sequence with the position of the label is shown for each of the dataset. The solid lines represent fit to a bi-exponential.

bi-exponential and yielded a component of ~ 300 ps representing rotational motion of the fluorophore and the longer nanosecond component representing segmental motion of the chain. The longer nanosecond component in case of bound Nup153FG increased 4 fold to ~ 20 ns from

5 ns in case of the unbound Nup153FG (See Table 4.4). It has to be noted that in reality the longer nanosecond component could actually be longer than 20 ns but not resolved due to the limited time window of the anisotropy decays (10 ns). This suggested an acute slowing down of the segmental motion of the chain due to Importin β binding. The most striking feature of the anisotropy decays with bound Importin β was a substantially increased residual anisotropy of 0.2 compared to 0.05 in the unbound state. These results suggested that in presence of Importin β local motions of Nup153FG had slowed down due to the binding interaction. This observation is also consistent with a previous segmental motion study of Nup153FG-Importin β interaction done in our lab¹⁰⁰.

Table 4.4: The values for the parameters of the anisotropy decay for all the mutants fitted to Equation 3.4.

Systems	ϕ_1 (ns)	Normalized a_1	ϕ_2 (ns)	Normalized a_2	r_∞
883C	0.44	0.44	3.26	0.66	0.07
883C + Importin β	0.24	0.31	23.3	0.69	0.16
990C	0.55	0.40	4.39	0.60	0.06
990C + Importin β	0.28	0.36	17.85	0.64	0.19
1330C	0.56	0.39	4.73	0.61	0.05
1330C + Importin β	0.28	0.27	27	0.73	0.14
1355C	0.61	0.35	5.5	0.65	0.07
1355C + Importin β	0.39	0.29	22.7	0.71	0.15

4.3.4 Site selective solvation dynamics in free Nup153FG and Nup153FG in the fuzzy complex with Importin β

After characterising the nature of the Nup153FG-Importin β interface at different sites using acrylodan steady state and time-resolved fluorescence and time resolved anisotropy, I measured the solvent response on Nup153FG at multiple sites using acrylodan labelled Nup153FG cysteine mutants. Solvation dynamics experiments needed measurement of lifetime across the emission spectrum. All the mutants showed wavelength dependent lifetime decays with lifetime decays at redder wavelengths becoming longer, as is expected when solvation dynamics occur. The TRES obtained via reconstruction from the lifetime data showed a progressive time dependant shift towards lower frequencies. Representative examples of wavelength dependent decays and reconstructed TRES for 1355C are shown in Fig 4.14. The maximum frequencies of the TRES at different time points were used to construct the solvent response curve (See Fig 4.14).

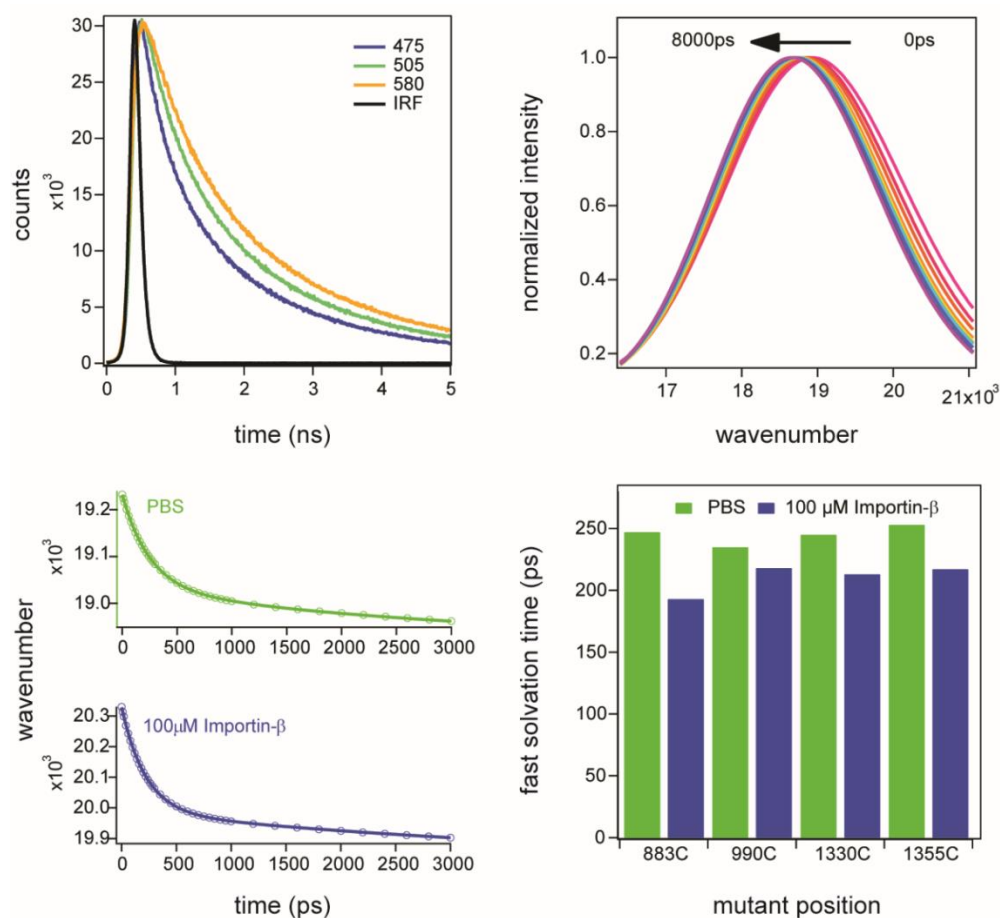


Figure 4.14 Solvation dynamics of Nup153FG mutants in presence and absence of Importin β : The solvation dynamics in Nup153 is measured by measuring lifetime decays at different wavelengths. A representative set of decays at 475 nm, 505 nm and 545 nm for Nup153FG 883C are shown (top left) where the decays become longer with increasing wavelengths. TRES is constructed from the fits of the decays. Representative TRES of Nup153FG 883C shown (top right) where the spectra progressively moves to lower frequencies with time. The solvent response curve (bottom left) is obtained by plotting the frequency maxima of the TRES obtained at different time points as a function of time. The representative solvent response curves for free Nup153FG 883C (in green) and IBB-Importin β complex (blue) are shown with the solid lines representing bi-exponential fits. The fast time component of the solvent response of the different mutants that represents water dynamics is shown for the free Nup153FG as well as in the fuzzy complex with Importin β complex (bottom right) as a bar plot. Two independent experiments recovered time constants within 15% of each other.

The solvent response for the free Nup153FG was found to be bimodal with a lot of the stokes shift of the TRES happening in under 500 ps followed by slower nanosecond relaxation, as was the case for the IBB systems. The data was thus analysed with bi-exponentials. The time

components recovered were ~200 ps and a longer nanosecond component of ~2-3 ns depending on the mutant. These components were interpreted in a way similar to that of IBB solvation dynamics data, the picosecond component assigned to surface water dynamics on the IBB and the nanosecond component attributed to slower protein dynamics or dye photophysics¹⁵⁹. The data thus suggested minimal changes (>15%) of the water dynamics on the Nup153FG surface when one moved from one site to another having different local sequence propensities.

After probing solvation dynamics on free Nup153FG I repeated the experiments in Nup153FG - Importin β to probe the water dynamics at the interface of the Nup153FG and Importin β . The solvent response curves for Nup153FG and Importin β were also bimodal and analysed with bi-exponentials yielding a picosecond component representing surface solvation dynamics and a longer component representing slower relaxation processes. To my surprise I found that unlike IBB, Nup153FG despite forming a desolvated interface upon complex formation with Importin β as seen from acrylodan fluorescence emission and lifetime, did not show any retardation of surface solvation at any of the sites. All the mutants showed a picosecond component of the solvent response arising from water dynamics to be ~200 ps (See Fig 4.14 and Table 4.5 for details of the fit). This invariance of the fast time component in Nup153FG upon Importin β binding was confirmed from two independent sets of experiments where the recovered time constants were within 15% of each other. This indicated that the interfaces of Nup153FG and Importin β were very labile and not rigid and hence the dynamics of water could remain unaltered compared to the free protein. Such unaltered dynamics of interfacial water might be related to presence and maintenance of the dynamic nature of the IDP in fuzzy complexes.

Table 4.5: The values obtained from bi-exponential fits of the solvent response curve for Nup153FG mutants

System	τ_1 (ps)	Normalized a_1	τ_2 (ns)	Normalized a_2
Nup153FG 883C	247	0.60	2.3	0.40
Nup153FG 883C + Importin β	192	0.82	6.8	0.18
Nup153FG 990C	235	0.73	2.4	0.27
Nup153FG 990C + Importin β	218	0.84	5.2	0.16
Nup153FG 1330C	245	0.66	3.4	0.34
Nup153FG 1330C + Importin β	213	0.73	7.4	0.27
Nup153FG 1355C	253	0.63	3.2	0.37
Nup153FG 1355C + Importin β	217	0.66	4.6	0.34

4.4 Dynamic characterization of a fuzzy complex NSP1FG and Importin β

To establish the generality of the observations on the FGNup-NTR fuzzy complex (Nup153FG and Importin β) I used another FGNup from Yeast, NSP1FG which had been reported to form a fuzzy complex with the NTR Kap95 (the Yeast homologue of human Importin β) using NMR spectroscopy¹⁰⁵. I first established fuzzy complex formation of NSP1FG with Importin β using single molecule FRET and FCS. Next, I used site selective acrylodan fluorescence to characterize interfacial environment in NSP1FG-Importin β complex. Finally, I measured solvent response on NSP1FG surface and at the interface of NSP1FG and Importin β to see if the results described in the previous sections on Nup153FG-Importin β were general for FGNup-NTR complexes and applied to other FGNup-NTR fuzzy complexes as well.

4.4.1 Single molecule characterisation of fuzzy complex formation by NSP1FG.

A hallmark of FGNup-NTR fuzzy complexes is binding without conformational change. Thus, to establish that NSP1FG forms a fuzzy complex with Importin β , binding and lack of conformational change of NSP1FG in the bound state had to be established.

First, to assess if Importin β caused a conformation change in NSP1FG I used smFRET which gives distance information between two points bearing donor and acceptor fluorophores and is thus a very good probe for conformational change. For smFRET experiments I used a NSP1FG fragment (1-175aa of NSP1FG) with a cysteine residue in the second position and the ncAA AcF at the penultimate position. The AcF was incorporated in response to an amber (TAG) codon via an amber suppressor machinery consisting of an orthogonal tRNA and aaRS pair which incorporated AcF. The acceptor dye Alexa488 maleimide was conjugated to the cysteine residue while the donor dye Alexa488 hydroxylamine was conjugated to the AcF residue. This allowed me to directly probe any conformational change in NSP1FG fragment.

I performed multiparameter smFRET experiments with PIE excitation combined with burst wise analysis on double labelled NSP1FG fragment, as I had done for IBBS24C/S55C described in previous sections. In the 2D histograms of S vs E_{FRET} (Fig 4.15) the population, where both the dyes were present and active (at $S \sim 0.5$ and variable E_{FRET}), was identified and monitored for probing FRET changes. Free NSP1FG fragment showed an $E_{\text{FRET}} \sim 0.41$. In presence of Importin β there was no shift in the E_{FRET} and it stayed practically constant at ~ 0.42 (See Fig 4.15). While both the datasets other than having a population having both donor and acceptor dyes contained a population bearing only donor dyes ($E_{\text{FRET}} \sim 0$, $S \sim 1$), the data for free NSP1 also showed a pronounced population of molecules bearing only acceptor dyes ($S \sim 0$). No change in E_{FRET} implied that NSP1FG fragment maintained its conformational ensemble in presence of Importin β . Such indifference of E_{FRET} and thus conformation of NSP1FG fragment indicated either fuzzy complex formation between NSP1FG fragment and Importin β or no interaction

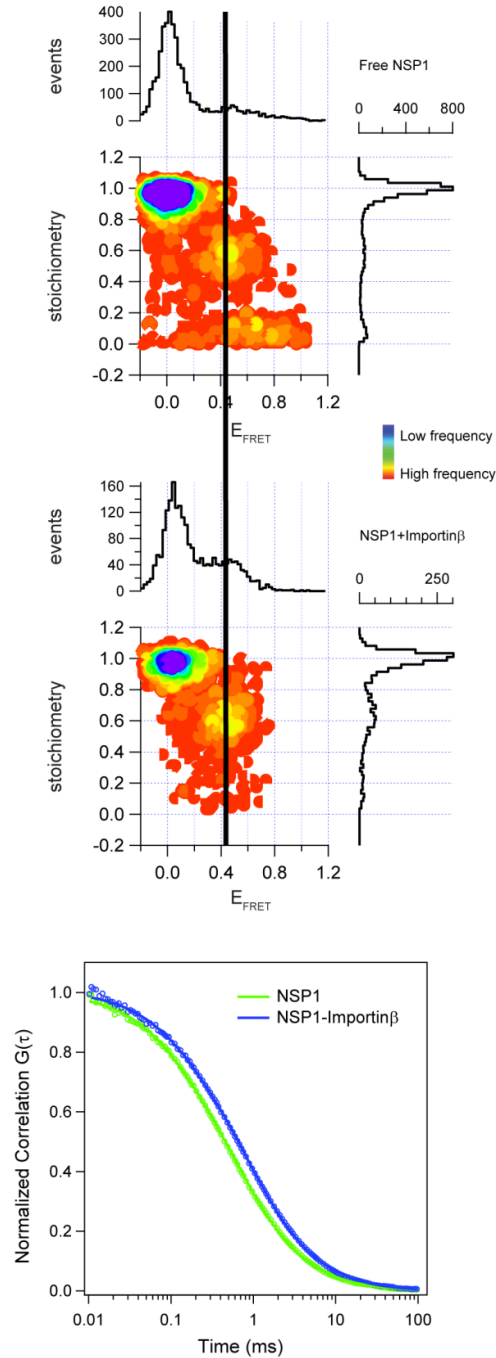


Figure 4.15 smFRET and FCS to probe fuzzy complex formation between NSP1FG fragment and Importinβ: The smFRET data is represented as 2D histograms of S vs E_{FRET} where populations corresponding to $S \sim 0.5$ represent molecules where FRET is happening. In free NSP1 fragment the E_{FRET} is 0.43 (top) and it remained unchanged in presence of Importinβ (middle). FCS data obtained from the smFRET data (bottom) shows the data for free NSP1 fragment (green) an NSP1 fragment in presence of Importinβ (blue) and the solid lines represent fits to 2D diffusion model with a triplet state.

between the two. To check for the presence of binding interactions between NSP1FG fragment and Importin β I used FCS. FCS traces were calculated from the smFRET data (See Figure 4.15). As was the case for IBB, for FCS data only the acceptor signal resulting from the acceptor laser pulse was used. FCS traces were fitted to a 2D diffusion model with a triplet state. Free NSP1FG fragment had a diffusion time of ~ 0.59 ms. In presence of Importin β the diffusion time increased to ~ 0.82 . A ~ 1.4 fold increased diffusion time indicated a large change in molecular weight and thus confirmed that NSP1FG fragment formed a complex with Importin β . From the combined smFRET and FCS results I could conclude that NSP1FG formed a fuzzy complex with Importin β where binding without any conformational change occurred. This was also somewhat expected as NSP1FG is known to form a fuzzy complex with the Yeast homologue of Importin β , Kap95.

4.4.2 Site specific acrylodan fluorescence to characterise NSP1FG-Importin β interface

After having characterised the NSP1FG-Importin β interaction to be that of fuzzy type, I engineered a single cysteine mutant NSP1FG 101C where the cysteine residue was placed in the region which I confirmed with smFRET to be interacting via a fuzzy mechanism with Importin β . NSP1FG 101C was site specifically labelled with acrylodan to characterise the binding interface of NSP1FG and Importin β in the fuzzy complex formed. Acrylodan labelled NSP1FG 101C showed an emission around ~ 535 nm, like acrylodan labelled IBBS24C and Nup153FG mutants, as expected for a solvent exposed site on an IDP surface lifetime (See Figure 4.16)

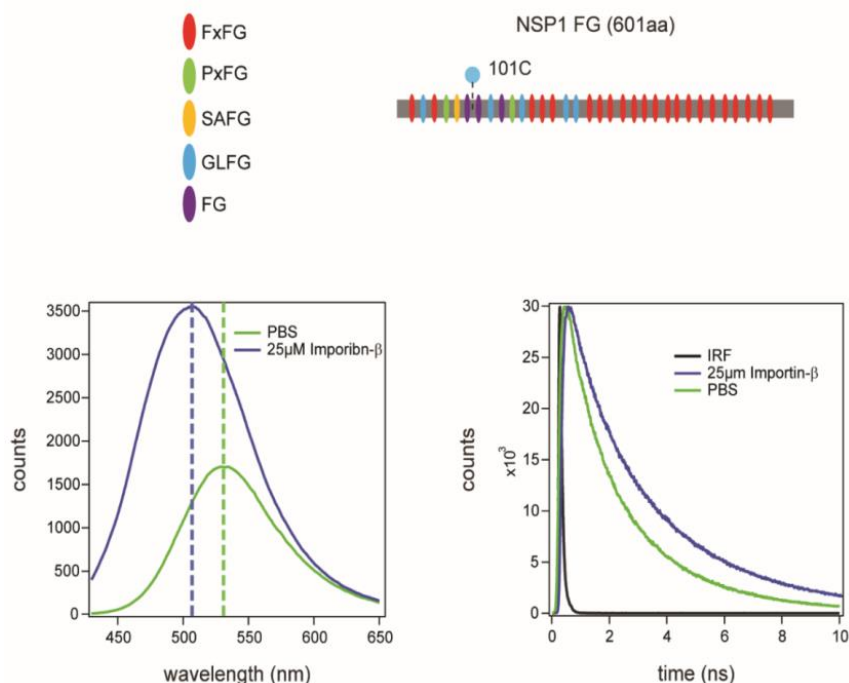


Figure 4.16 Acrylodan emission and lifetime in NSP1-Importin β interaction: A schematic showing the labelling position of acrylodan in the context of the sequence of NSP1 (top). Steady state emission for NSP1 101C (bottom left) shows the emission spectra in PBS (green line) to be blue shifted in presence of Importin β (blue line). The lifetime decay of acrylodan labelled NSP1 101C at 535 nm (bottom right) for NSP1 101C in free state (green line) and in presence of Importin β (blue line) showing increased lifetime in presence of Importin β .

Upon addition of Importin β the spectral maxima underwent a 30 nm shift to 505 nm from 535 nm in the free protein; this was also accompanied by a ~2.5 fold increase in intensity and 1.5 fold increase in average lifetime (See Figure 4.16). Acrylodan's emission is strongly polarity dependent and blue shift indicated decreased local polarity around the fluorophore. This spectral behaviour was very similar to that observed during binding of both IBB and Nup153 to Importin β and resulted very likely from the desolvation of the IDP surface upon binding. The intensity and lifetime increase observed for NSP1FG 101C was also seen when Nup153FG and IBB bound Importin β and this effect could also be explained via desolvation near the fluorophore resulting in decrease of the amplitude of non-radiative processes contributing to depopulating the excited state. To quantitate the extent of the desolvation I estimated local relative permittivity sensed by acrylodan on NSP1 101C by itself and in presence of Importin β as was done for acrylodan labelled Nup153FG cysteine mutants and IBBS24C by comparing emission spectral maxima with spectral data for acrylodan-2-mercaptoethanol in different solvents (See Figure 4.17).

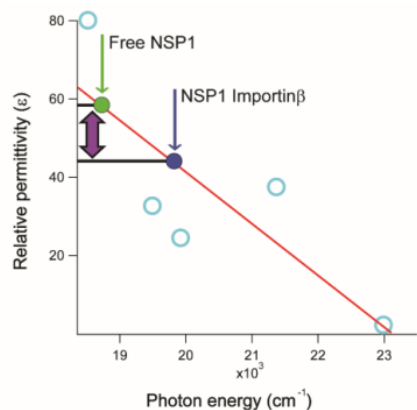


Figure 4.17 Relative permittivity for NSP1 in presence and absence of Importin β : The peak frequencies (cyan open circles) of acrylodan- β conjugate in different solvents is plotted against the relative permittivity of those samples. The red line represents a linear fit through the data. The relative permittivity experienced by acrylodan in unbound NSP1 (green solid circle) and in presence of Importin β (blue solid circle) is obtained from the emission peak frequencies using the equation ($\epsilon_r = -0.013\nu_{\max} + 304$ where ϵ_r and ν_{\max} are the relative permittivity and emission maximum frequency in cm^{-1} respectively) for the linear fit of the relative permittivity vs emission frequency of acrylodan-2-mercaptoethanol. The data shows decreased relative permittivity of IBB bound to Importin β compared to free IBB

The local relative permittivity in unbound NSP1FG 101C was 58.5 which decreased by ~15 units to 44.1 in presence of Importin β (See Fig 4.17). Relative permittivity served as a proxy for local polarity, with a reduction in polarity reducing relative permittivity. The extent of the drop in relative permittivity for NSP1FG upon Importin β binding was similar to that of IBB and Nup153FG; thus the amount of reduction in polarity stemming from desolvation for NSP1FG upon partner binding was similar to those of IBB and Nup153FG.

4.4.3 Site specific solvation dynamics of NSP1FG and the NSP1FG-Importin β interface

After having characterized the nature of the NSP1FG-Importin β interface using acrylodan steady state and time-resolved fluorescence, I measured the solvent response on NSP1FG using acrylodan labelled NSP1FG 101C. Lifetime decays across the emission spectra were collected. The decays showed wavelength dependence, the decays became longer with increasing wavelength as is expected when solvation dynamics occur (See Figure 4.18). The fitting parameters obtained from the fluorescence decays were used to reconstruct the TRES which showed a continuous time dependent shift towards lower frequencies. Wavelength dependent decays and reconstructed TRES for NSP1FG 101C is shown in Figure 4.18. The maximum frequencies obtained from the TRES at different time points were used to construct the solvent response curve (See Figure 4.18).

The solvent response of free NSP1FG 101C was clearly bimodal, as was the case for all the previous systems. The data was thus analysed with bi-exponentials. The time components recovered were ~100 ps and a longer nanosecond component of ~1.7. The components were interpreted in a way similar to that of IBB and Nup153FG solvation dynamics data, the picosecond component originated from surface water dynamics on NSP1FG and the nanosecond component probably originated from slower protein dynamics or dye photophysics¹⁵⁹.

Having characterised the solvent response on NSP1FG surface I performed the experiment to probe the solvent response in presence of Importin β and see how Importin β binding modulated the solvent response. The solvent response at the NSP1FG-Importin β interface was also bimodal and analysed with bi-exponential. The time components recovered were 100 ps and 3.3 ns. Thus, the fast picosecond component arising from surface water dynamics remained unchanged at ~100 ps in comparison to the free protein (See Table 4.6). This indicated that despite forming a solvent excluded hydrophobic interface with Importin β , the binding did not perturb the dynamics of the water molecules. This behaviour was qualitatively very similar to that seen for Nup153FG where the presence of Importin β did not affect the dynamics of water molecules on the surface of the IDP. The most crucial aspect of this experiment was that it strongly supported the fact that

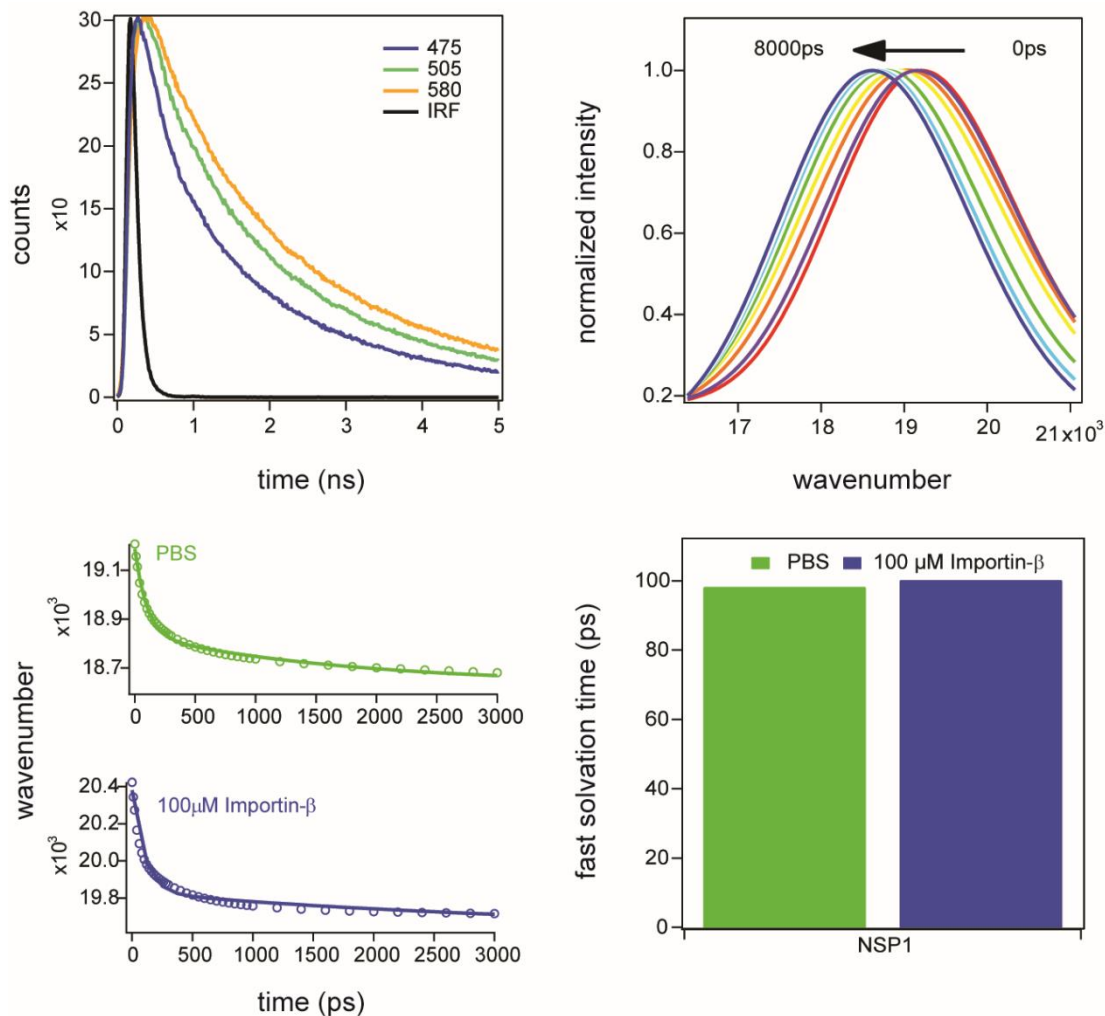


Figure 4.18 Solvation dynamics of NSP1 101C in presence and absence of Importin β : The solvation dynamics in NSP1 101C is measured by measuring lifetime decays at different wavelengths. Representative decays at 475 nm, 505 nm and 545 nm for NSP1 101C are shown (top left) where the decays become longer with increasing wavelengths. TRES (top right) is constructed from the fits of the decays shown where the spectra progressively moves to lower frequencies with time. The solvent response curve (bottom left) is obtained by plotting the frequency maxima of the TRES obtained at different time points as a function of time. The solvent response curves for free NSP1FG 101C (in green) and IBB-Importin β complex (blue) are shown with the solid lines representing bi-exponential fits. The fast time component of the solvent response representing water dynamics is shown for the free NSP1 as well as in the fuzzy complex with Importin β complex (bottom right) as a bar plot. The time components recovered from two independent experiments were within $\sim 15\%$ of each other.

the observed unchanged solvation dynamics after binding partner protein, is general to Nup-NTR interactions or probably even fuzzy interactions at large. Biologically for NSP1 the implications of having unperturbed water dynamics upon binding partner proteins might have a role in the formation and dynamics of these fuzzy complexes, as might have been the case for Nup153FG.

Table 4.6: The values obtained from bi-exponential fits of the solvent response curve

System	τ_1 (ps)	Normalized a_1	τ_2 (ns)	Normalized a_2
NSP1 101C	98	0.63	1.7	0.37
NSP1 101C + Importin β	101	0.77	3.3	0.23

Chapter 5

5 Discussion

In this section, I will first describe the comparison of the implications of my spectroscopy experiments on solvation; I will construct a simple energy barrier based argument to explain how differential modulation of solvation dynamics is related to different binding mechanisms. Subsequently, I will explain some of the challenges in the experiment and complementation of my data with MD simulations, which provide a complementary perspective on solvation dynamics in IDPs and IDP complexes and discuss the limitations of both the techniques. Finally, I will discuss the general biological implications of my results in the context of IDP biology with major emphasis on the nucleocytoplasmic transport.

5.1 Implications of interfacial solvation dynamics in the plasticity of IDP-protein complexes

My spectroscopic experiments can be summarized by two general observations:

- 1) When an IDP binds a partner the interface formed is more hydrophobic and desolvated compared to the free IDP surface. This happens irrespective of whether the binding mechanism is coupled folding-binding or fuzzy complex formation.
- 2) The interfacial solvation dynamics in an IDP complex compared to solvation dynamics on the IDP surface is dependent on the binding mechanism. For fuzzy complexes interfacial solvation dynamics is not retarded compared to the free IDP, while in complexes formed by coupled folding-binding mechanism there is a retardation of interfacial solvation dynamics compared to the free IDP.

I have shown formation of a desolvated hydrophobic interface in IBB-Importin β complex (See Figure 4.7 and Figure 4.8), Nup153FG-Importin β complex (See Figure 4.10 and Figure 4.11) and NSP1FG-Importin β complex (See Figure 4.16 and Figure 4.17) using steady state and time resolved acrylodan fluorescence. The desolvation upon partner binding likely favours binding interactions by an entropic gain from release of bound water molecules. This effect is akin to the hydrophobic effect and applies to most bimolecular recognition processes in general. The change in interfacial solvation upon binding is however very much dependent on the mechanism (See Figure 5.1). There is a general difference between complexes of IDPs formed by a fuzzy binding mechanism and those formed by coupled folding-binding mechanism from the standpoint of interfacial solvation dynamics. I have shown that interfacial solvation is slowed down in case of IBB-Importin β complex which is formed by coupled folding-binding mechanism (See Figure 4.9). I have also shown that in Nup153FG-Importin β (See Figure 4.14) and NSP1FG-Importin β (See Figure 4.18), which are fuzzy complexes, interfacial solvation remains largely unperturbed

contrasting to my observations for IBB-Importin β . The fold change in the timescales of solvation dynamics of the IDPs upon partner binding clearly demonstrates this binding mechanism dependent modulation of solvation dynamics (See Figure 5.1). This lets one associate distinct dynamical fingerprints with distinct binding mechanisms in IDPs and allows classification of IDP complexes solely from a solvation dynamics standpoint. The two types of complexes studied differ greatly in terms of the plasticity of the IDP in the complex; in a complex formed by a coupled folding-binding interaction the IDP assumes a folded structure with stable secondary structural elements while in a fuzzy complex an IDP retains its disorder in the bound state and thus retains fast conformational dynamics owing to lack of any persistent secondary structural elements. Considering that IDPs lack structural motifs to guide recognition, my finding that different IDP binding mechanisms are correlated with different types of interfacial water dynamics, necessitates some deliberation about the role water dynamics may play in distinct modalities of IDP recognition.

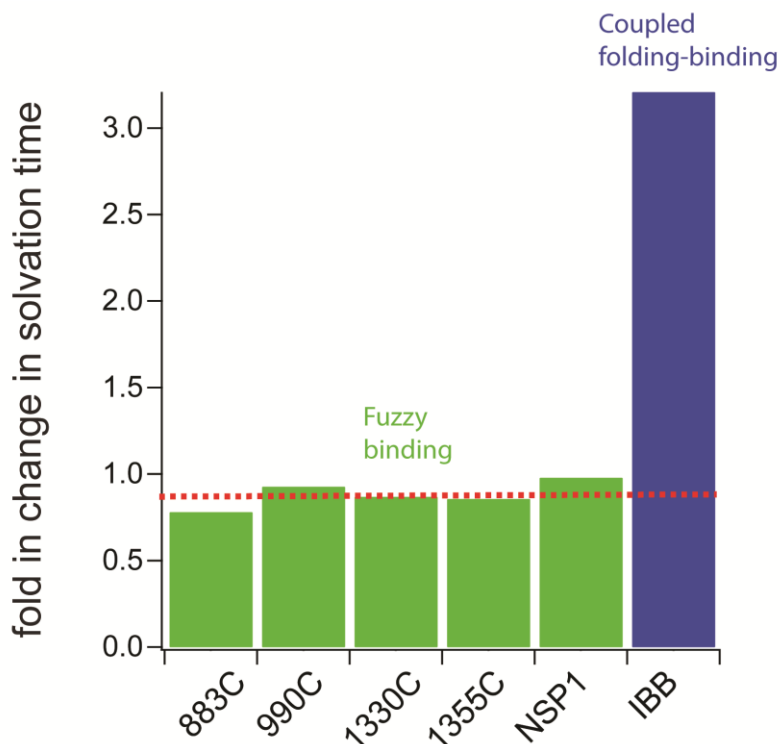


Figure 5.1 Comparison of solvation dynamics modulation upon partner binding in IDPs; fuzzy complex formation vs coupled folding-binding: Relative change of the 10-100ps component of solvation dynamics of Nup153FG mutants (green), NSP1FG (green) and IBB (blue) upon binding Importin β from spectroscopy experiments. All Nup153 mutants and NSP1FG show minimal perturbation of solvation dynamics while IBB shows a dramatic slowdown in solvation by ~3-fold, upon binding Importin β . The red dashed lines represent the average values of fold changes in solvation when Nup153 mutants and NSP1FG bind Importin β .

For a coupled folding-binding system, the interface formed between the IDP and the partner is a ‘folded-folded’ interface; this type of interface essentially constitutes the interfaces in all complexes formed by folded proteins and has been studied extensively. There is evidence that water dynamics at ‘folded-folded’ interfaces of protein complexes is retarded compared to the surface; for example a MD study systematically analyzed the dynamically retarded features of interfacial water in 17 protein complexes¹⁷⁵ and a recent computational study demonstrated the role of slow dynamics of ~10 interfacial water molecules in stabilizing the insulin hexamer structure¹⁷⁶. There is also evidence that a folding transition is associated with slowing down of solvation as seen for HSA^{137,135} and the slowed dynamics help in stabilization of the folded structure. Based on these arguments it is reasonable to assume that the ‘folded-folded’ interface formed by a disordered IDP upon recognition of its partner in a complex formed by coupled-folding binding would have slower water dynamics compared to the free IDP. The slowed down dynamics is likely involved in the stabilization of the interface and subsequently the complex.

In a fuzzy complex, the interface between the partner and IDP is typically a ‘disordered-folded’ interface where the interface constitutes folded elements of the partner and disordered elements from the IDP. Unlike a ‘folded-folded’ interface, little is known about the water dynamics in a ‘disordered-folded’ interface. In the ‘disordered-folded’ interface there is substantially more dynamics compared to a ‘folded-folded’ interface. If retarded water dynamics is likely linked to stabilization of ‘folded-folded’ interface, unperturbed water dynamics might be linked to the plasticity of a ‘disordered-folded’ interface, facilitating fast dynamics of the IDP in the bound state. Recent studies that indicate direct slaving of protein dynamics by solvent dynamics^{140,144,145} also support the fact that maintenance of fast dynamics of the IDP at the interface in a fuzzy complex would require water dynamics to remain as fast as in the free IDP. Also fast and dynamic processes have been associated with non-retarded interfacial solvation dynamics; for example a fast DNA polymerase does not experience substantial slowing down of water dynamics at the active site and DNA interface while a slow polymerase does^{141,142}.

I have finally come up with a physical schematic model to explain how differential interfacial solvation dynamics may be related to and probably be the driving force behind differential plasticity in different IDP complexes formed by different mechanisms (See Fig 5.2). The essential idea behind this model is the fact that solvent reorganization poses energy barriers. Thus in a scenario where interfacial solvation in the bound state is slower than in the free state of an IDP, as seen in coupled-folding binding complexes, conformational fluctuations are impeded by free energy barriers arising from solvent reorganization when transitioning from bound to free state occurs or vice-versa. However, when solvation dynamics remain unperturbed in the bound state, as seen for fuzzy complexes, free energy barrier from solvent reorganization does not arise, facilitating unimpeded dynamics. This would explain why coupled folding-binding systems show greater kinetic stability and lesser dynamics than fuzzy systems. While ‘Aristotelian

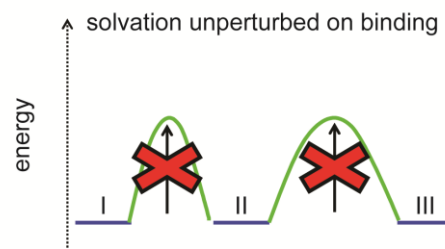
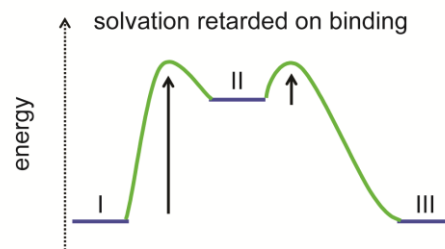
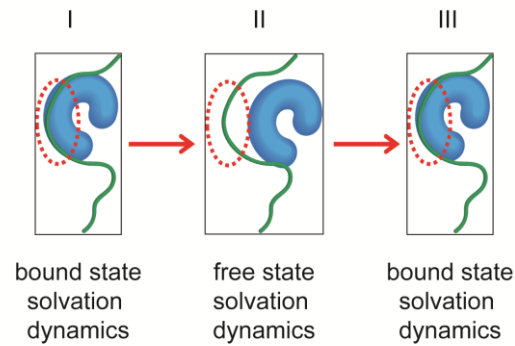


Figure 5.2 A model highlighting potential regulatory roles of solvation dynamics in governing plasticity of IDP in a complex: A schematic showing an IDP bound to its partner performing conformational fluctuations (top). The circled area represents a portion of the IDP that transiently disassociates and reassociates with the partner. This conformational fluctuation is captured in three distinct molecular states, I, II and III. A schematic showing the energy barrier during conformational fluctuations of an IDP, when solvation dynamics in the bound state is slower than that in the unbound state (middle). The three states described in the top schematic are represented in terms of energy and are at different free energy levels due to the solvation retardation which results in formation of energy barriers that kinetically impede conformational fluctuations. A schematic similar to the middle schematic showing energy barriers in conformational fluctuation of an IDP when solvation dynamics remains unperturbed upon binding (bottom). These result in minimal energy difference between the states during the conformational fluctuation with barriers from solvent reorganization eliminated and thus the process can be very fast.

teleology, might spur one to promptly infer based on this discussion that interfacial dynamics dictates plasticity of IDP complexes and consequently binding mechanisms, such interpretations should be made with due caution. This is because in this scenario it is not straightforward to establish causality as one cannot very easily modulate solvation in a predictable fashion and see its effects on dynamics. However, what can be said with certainty is that the different IDP complexes formed by the different mechanisms of coupled folding binding and fuzzy complex formation, are associated with differential modulation of interfacial solvation dynamics and this differential modulation of solvation dynamics certainly contributes to facilitating dynamics in fuzzy complexes and kinetic stability in coupled-folding binding based complexes. This underscores the role of water as a major stakeholder in IDP recognition and hints at the possibility that in the absence of structural motifs IDPs may employ solvation dynamics to attenuate the plasticity of IDP complexes for achieving diverse functionality.

5.2 Complementation of solvation dynamics spectroscopic experiments with MD (Molecular Dynamics) Simulation

5.2.1 Challenges of monitoring solvation dynamics

Solvation dynamics in the experiments I performed was monitored by using dipolar relaxation probes. This approach provides the advantages of site specificity; however, it also suffers from several limitations like potential invasiveness of the probe, entanglement of slower relaxations like protein dynamics with solvent response and limited time resolution.

The site-specific incorporation of a fluorescent probe to investigate solvation dynamics brings the question of invasiveness of the fluorescent probe. I performed required control experiments to ensure that this should not be the case for all the systems I have studied, and established that interaction of the labelled proteins with its partner would still be happening. Specifically, I showed for FGNups that acrylodan labelling at multiple sites did not interfere with NTR binding (See Figure 4.12) and for IBB I showed that labelling the site used for acrylodan conjugation did not impede disorder to helix transition (See Figure 4.4 and Figure 4.5). While these observations largely exonerate dye labelling to be a source of potential artefacts, another issue with probes is that in situations where the actual binding motif is minimal, such as FG motifs in FGNups, using a label makes it impossible to probe those motifs directly.

The measurement of solvation dynamics via a spectroscopic approach, due to the physics of dipolar relaxation, will report on any dipolar entities other than water such as protein backbone and side-chains around the fluorophore which would also lead to this relaxation process, hence one cannot exclusively probe water dynamics. Usually dynamic processes other than solvation

are significantly slower than water dynamics and it is thus possible to separate the components of a solvent response based on the timescales of the recovered time components from the solvation response. While this is a modestly reasonable approach, such analysis suffers from the risk of misinterpretation in case of extremely complex systems such as IDPs.

A technical limitation of the current measurements, I presented in previous sections, is the fact that with the current time resolution of ~ 100 ps I missed a significant part of the solvation dynamics happening in under 10ps. While biological recognition is mainly related to modulation of slower components of solvation dynamics^{152,142} which was resolvable in my experiments, it can still be insightful to explore the fast dynamics. From the experimental side this can be addressed using advanced spectroscopic techniques such as femtosecond resolved transient absorption spectroscopy and that is what I am currently pursuing (Outlook section).

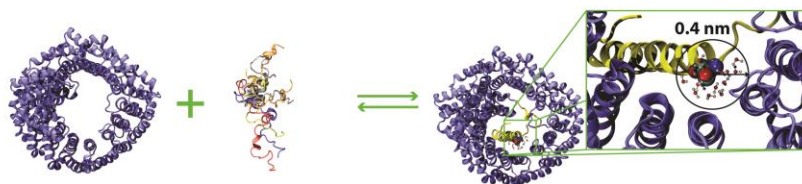
5.2.2 Correspondence of the MD simulations with spectroscopy; insights from the combined approach

Atomistic MD simulations have the potential to alleviate some of the issues mentioned in the previous sections. MD simulations can directly probe solvation or protein dynamics for a given system in its indigenous form with atomistic resolution in any region of interest without the need for a label, thus eliminating all potential concerns about invasiveness of fluorescent labels and the failure of fluorescent labels to directly probe minimal motif based interactions. Additionally, atomistic MD simulations provide direct access to the water molecules and thus an opportunity to probe exclusively the dynamics of water molecules, unlike experiments where the solvent response might be entangled with other dynamical process. Finally MD simulations offer an unprecedented time resolution and can help investigate if any dynamics faster than what I could have measured spectroscopically contribute to the dynamics and interaction of a system. Hence, while MD has its own sets of limitations discussed later, it seems to be a powerful tool with the potential to offer complementary information about solvation in IDPs which would help overcome some of the shortcomings of my current experiments. Thus a combined MD simulation and spectroscopy approach would provide more complete and holistic information about solvation dynamics in IDPs and its molecular role in IDP dynamics and interactions; even qualitative correspondence between observations made using MD simulation and spectroscopy would serve as a more rigorous validation of the observations. To this end I collaborated with Prof. Frauke Gräter in the HITS Institute and her postdoctoral student Davide Mercadante who performed MD analysis of solvation dynamics in some of the systems that I studied spectroscopically.

To investigate solvation dynamics by MD simulations a sphere of 4\AA radius was constructed around the regions of interest. For IBB the region of interest was the S24C residue, the same residue that I mutated to a cysteine residue in my experiments (See Figure 5.3). For Nup153FG,

MD simulations were performed on the FxFG (1310-1391 of Nup153FG) fragment of Nup153FG; the region of interest was defined around an F residue in a PxFG motif to directly probe the solvation on the actual binding motif (See Figure 5.3). All the water molecules in the mentioned 4Å radius sphere were analyzed over the entire trajectory of the simulation. This allowed exclusive analysis of water dynamics close to the IDP surface in the free IDP and in complex with the partner Importinβ.

MD simulations on IBB recognition



MD simulations on Nup153FG
PxFG recognition

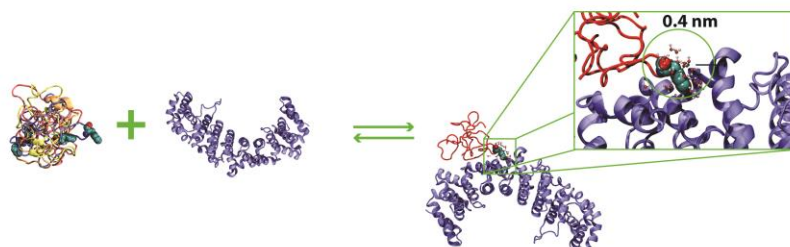


Figure 5.3 Regions of interest defined for solvation dynamics analysis by MD simulations: This figure has been provided by Dr. Davide Mercadante. Importinβ and IBB in isolation and in complex (top). The structures are shown using cartoon representation and coloured light blue for Importinβ and with different colours for IBB in its unstructured ensemble. After complex formation, IBB is fully helical and is shown in yellow. S24 used to tag the protein with acrylodan is shown using the vdW surface and coloured by atom type. Importinβ and the water molecules at the binding interface, within the considered cutoff of 0.4 nm are shown as balls and sticks and coloured by atom type. Nup153FG conformers unbound and bound to Importinβ (bottom). Unlike IBB, FG-Nups retain a disordered state when they bind to NTRs. FG repeats along the sequence of the intrinsically disordered nucleoporin are shown by vdW surface and coloured by atom type. In the zoom-in windows at the right-end side of the figure, water molecules at the binding interface, within the considered cutoff of 0.4 nm are shown as balls and sticks and coloured by atom type.

For analysis of solvation dynamics the residence times of the water molecules in the defined regions of interest were analyzed over an entire MD trajectory. Analysis of residence times provides a very direct handle on solvation dynamics as it interrogates directly how dynamically constrained water molecules are on a molecule by molecule basis in a given region of interest. This analysis would thus be a very good approach to corroborate my experimental data; this is because this would be complimentary to my experiments which measured dipolar relaxation, that reports the overall collective response of the water and the environment to a perturbation.

The residence time distribution of the water molecules in the defined regions of interest were analyzed with biexponentials and typically yielded two components, a short picosecond component under 10 ps (~5 ps) and another long picosecond component in tens of picoseconds (See Figure 5.4). The order of these time scales are in perfect alignment with time scales of solvation measured in several proteins spectroscopically using dipolar relaxation of tryptophan^{145,177}; this establishes a direct phenomenological link between solvation dynamics analyzed from residence times of water using MD simulations and that obtained from dipolar relaxation spectroscopy.

The short picosecond component obtained from MD simulations is inaccessible with our time resolution. However, the MD data also showed that this short picosecond component remained constant across the various systems indicating that this component of water dynamics might not be super critical for biological recognition. This is also evidenced by few spectroscopic studies of protein solvation in the context of molecular recognition where the sub-10 picosecond component shows minimal change in different conditions; for example, when a polymerase binds DNA¹⁴² or an IDP undergoes an amyloid transition¹⁵² the timescale of the sub-10 picosecond component of solvation dynamics remains practically unchanged. This means that experimentally the part of the solvent response we missed in all likelihood did not contain any dynamic information, which is related to molecular recognition.

The long picosecond component obtained from MD was on the same timescale as the picosecond component observed in my spectroscopic experiments, in the order of 10s to 100s of picoseconds. This parity in the order of the timescale also assured me that the assignment of the picosecond component of the spectroscopically obtained solvent response as surface water dynamics was correct. Each MD trajectory was run for 20 ns, hence in case solvation dynamics was associated with additional slower nanosecond timescales, their presence would have been apparent in the MD data. The absence of any prominent nanosecond component in the decay of water residence time from MD simulations also ascertains that the nanosecond component of the solvent response that I obtained from spectroscopy, were possibly artefacts originating from slower relaxation processes as I had interpreted.

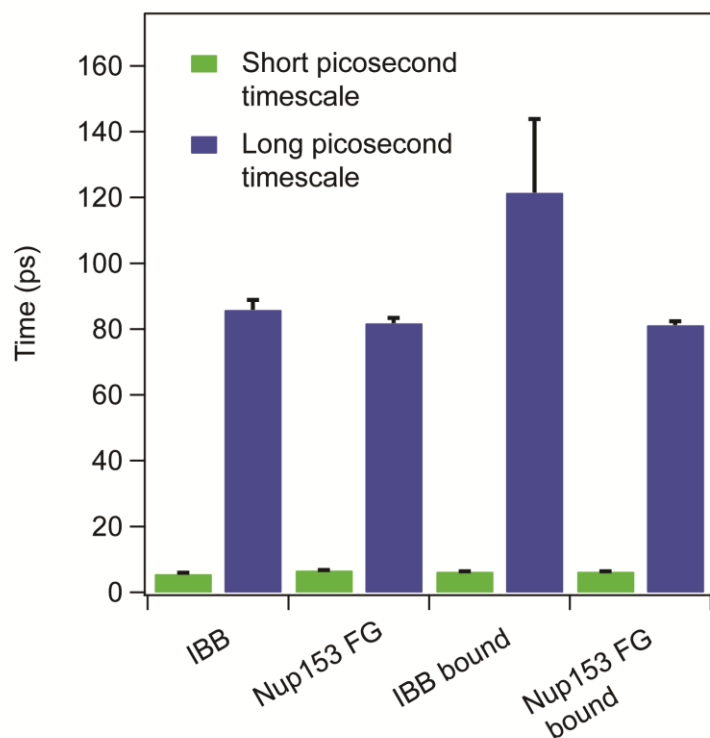


Figure 5.4 Analysis of solvation dynamics from MD simulations: The residence times of water obtained from MD in the different regions of interest in the different protein systems are analysed with a bi-exponential. The data is shown as a bar plot showing the fast picosecond time component (green) and slow picosecond time component (blue) for Nup153FG and IBB in free state and in bound state. The error bars represent standard error of the mean. The data plotted in this figure is from Dr. Davide Mercadante.

The MD data showed good qualitative correspondence with the spectroscopic experiments. Unlike the short picosecond component, the longer picosecond residence time component obtained from the MD simulations changed depending on the system studied. For the Nup153PxFG segment, the long picosecond residence time obtained from MD (~80 ps) was completely agnostic about whether the IDP was in a free state or bound to its partner Importin β (See Fig 5.5). This finding is not only in line with the spectroscopic observation but also extends the realm of our understanding of solvation dynamics in FG Nup-NTR complexes based on spectroscopic measurements. Unlike in the spectroscopic experiments, in MD simulations the water dynamics is probed around a F residue in an FG motif that constitutes the actual binding epitope. For IBB, MD simulations revealed a ~1,4 fold slowdown of the long picosecond water residence time around the S24 residue, evolving from ~80ps in the unbound state to ~125ps in the Importin β bound state (See Fig 5.5); this is again in perfect qualitative agreement with my spectroscopic observation.

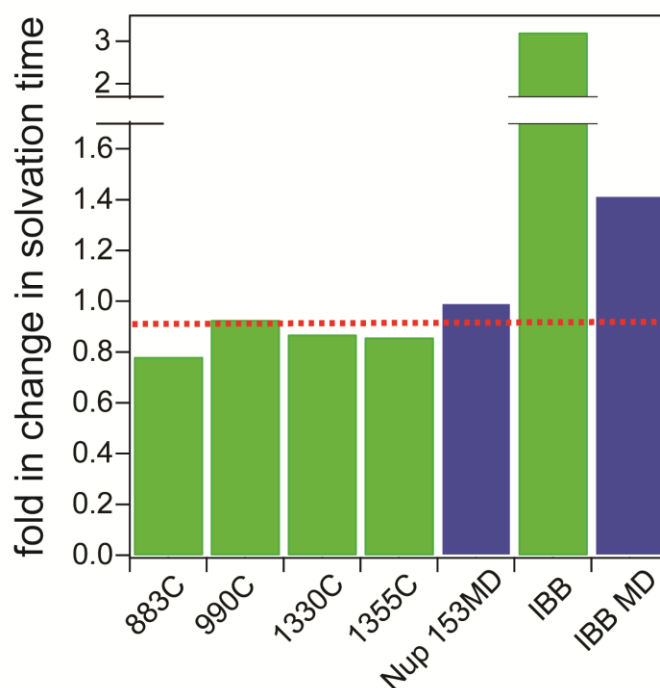


Figure 5.5 Comparison of solvation dynamics from MD simulations and spectroscopy: Relative change of the 10-100ps component of solvation dynamics of Nup153FG and IBB upon binding Importin β from both spectroscopy and MD simulations. All Nup153 mutants show minimal perturbation of solvation dynamics while IBB shows a dramatic slowdown in solvation by \sim 3-fold from experiment and \sim 1.5-fold from simulations upon binding Importin β . The red dashed lines represent the average values of fold changes in solvation when Nup153FG binds Importin β . The MD data used in this figure is from Dr. Davide Mercadante.

While MD simulations and spectroscopic experiments are consistent in qualitatively sensing relative retardation of solvation dynamics between protein pairs, when comparing absolute numbers between FG Nup-NTR vs IBB-NTR, there is a twofold discrepancy. The primary source of discrepancy arises from the fact that MD simulations and spectroscopic experiments probe two different observables of solvation dynamics namely residence time and dipolar relaxation as mentioned earlier; dipolar relaxation probes the collective response of water molecules to a perturbation while residence times probe the time spent by individual water molecules in a defined region of interest and this makes these two quantities complementary but not formally related. Hence, in some sense attempting to make qualitative comparisons between these two observables is not valid. Additional sources of this discrepancy likely lie in inaccuracies of the protein as well as the water force field¹⁷⁸, the effect is more pronounced in the cases where the systems studied are IDPs as IDP dynamics are extremely sensitive towards the choice of the force field^{179,180,181}. One should also note that a similar discrepancy with experiments existed

even for previous MD simulation studies that probed solvation by computing an observable that was measured directly by experiments^{177,149}.

To summarize, a combination of spectroscopic and MD studies offers a unique perspective on IDP solvation dynamics in the context of binding interaction. Both simulations and spectroscopy unambiguously demonstrate stark differences in the relative retardation of solvation dynamics at the interface of an IDP and a partner protein, depending on the binding mechanism of the IDP. For IBB, which undergoes a coil to helix folding transition upon binding its partner Importin β , there is a slowing down of solvation; while solvation remains unperturbed around Nup153FG upon formation of a fuzzy complex with Importin β where Nup153 retains its disorder. Both technologies, spectroscopy and MD simulations, capture this phenomenon reporting a change of ~ 0.9 and ~ 1 - fold for Nup153FG, and ~ 1.5 and ~ 3.2 fold change for IBB respectively (See Fig 5.5). Thus, one can conclude that both spectroscopy experiments and MD simulations capture the same trend in solvation dynamics associated with different binding mechanisms of IDPs, validating the combined MD and spectroscopic approach and subsequently validating the proposed molecular mechanism by which solvation modulation governs binding plasticity.

5.3 Implications of interfacial solvation dynamics in the plasticity of IDP-protein complexes

The biological implications of differential solvation dynamics in different types of IDP complexes can be far reaching. My results help explain the functionality of IDPs involved in the nucleocytoplasmic transport pathway I studied, IBB and FG Nups, from a dynamic standpoint.

Recognition of IBB by Importin β leads to the formation of the import complex⁷⁷. For a successful transport event across the NPC it is imperative that the import complex is stable during transit across the NPC which typically happens on a millisecond timescale^{96,94}. I believe that the slow water dynamics at the interface is key to the kinetic stability of the complex and is associated with strong energy barriers preventing conformational plasticity and subsequent disassociation. Biochemical and MD simulation studies support this notion. MD simulations showed very stable secondary structure in IBB bound to Importin β over a 40 ns MD trajectory showing minimum conformational fluctuation¹⁸² and SPR experiments showed a low k_{off} of $\sim 10^{-5}$ s⁻¹ suggesting high kinetic stability¹⁸³.

For the FG Nup-NTR system, a recent detailed investigation spearheaded by our lab²⁵ revealed a novel ultrafast binding mechanism where a disordered FG Nup binds a NTR retaining its disorder through a set of multivalent fast low affinity interactions forming an archetypal fuzzy complex²⁵. This allows fast yet selective transport across the NPC where multivalency ensures overall affinity between the FG Nup and the NTR while low affinities of individual FG motifs facilitate

fast dynamics and fuzziness in the complex (See Transport paradox section in Introduction). A recent computational study afforded a visual description of how FGNup-NTR interaction might facilitate fast transport¹⁰⁶; the said study demonstrated the FGNup-NTR interface to be labile on a picosecond-nanosecond timescale allowing a 2D slide of transporter along the FGNup to facilitate fast transport. An important question that came out of the study is: what are the barrier reducing mechanisms, which facilitate such ultrafast dynamics at the FGNup-NTR interface? While it is experimentally very challenging if not impossible to pinpoint all barrier reducing mechanisms, from my data it is clear that non-retardation of solvation dynamics in FGNups upon NTR binding contributes to reducing the barrier toward fast conformational fluctuations. Hence my results add a new perspective to this novel binding mechanism.

The implications of interfacial solvation dynamics modulation is not limited to NPC biology only and can play a crucial role in IDP biology. For example, solvation dynamics in amyloid fibrils formed from an amyloidogenic IDP κ -casein is substantially retarded compared to the free IDP¹⁵²; this might explain the extreme kinetic stability of amyloids in general. Solvation dynamics might also play a role in the retention of dynamics, disorder and lability in liquid-liquid phase separated states for IDPs, which is subject to investigation though. In summary, solvation modulations have strong implications in IDP complex dynamics leading to a spectrum of plasticity ranging from fast and dynamic to stable, tightly bound, and subsequently leading to a variety of functions ranging from transient dynamic interaction to long lived interactions.

Chapter 6

6 Outlook

In this section I will discuss how I have tried to overcome the limited time resolution of my current experiments, with new measurements based on femtosecond transient absorption (fsTA) spectroscopy in collaboration with Professor. Nikolaus. P. Ernsting and Dr. Sergey Kovalenko in his group at the Humboldt University of Berlin. I will then talk about some preliminary data obtained for IBB and the IBB-Importin β complex, where by combining the data from fsTA spectroscopy and my TCSPC based picosecond measurements I can see dynamics from 100 fs to >20 ns thus covering over 5 orders of magnitude in time.

6.1 Principles of measuring TDFSS using fsTA spectroscopy and its advantages

6.1.1 Basics of fsTA principles and schematic representation of data

In a fsTA setup a femtosecond laser (pump) pulse at a given wavelength is used to produce an electronic transition. The pump pulse is focused onto a diffraction limited spot in the sample. A femtosecond supercontinuum pulse (probe) covering a continuous broad range of wavelengths interrogates the sample and measures absorption spectra at different times relative to the pump pulse. A simplified schematic is presented in Figure 6.1. The probe pulse is focused on an overlapping diffraction limited spot on the sample with an angle (in this case 5 degrees) with the pump pulse¹⁸⁴.

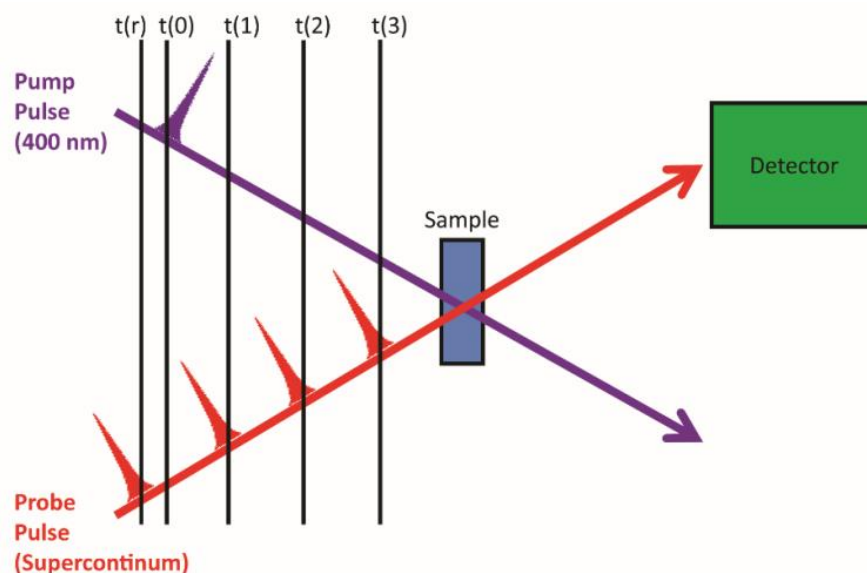


Figure 6.1 A schematic of fsTA spectroscopy: A femtosecond probe pulse (in our case 400 nm) excites a sample at time $t(0)$, defining the zero time of the experiment. A pump pulse interrogates the sample at time $t(r)$ which is before $t(0)$ and at different times $t(1)$, $t(2)$ and $t(3)$ after $t(0)$. The measurement from the probe pulse at $t(r)$ serves as a reference to which measurements from probe pulses at subsequent times are compared.

The data is usually presented as a difference spectra at different time point where the absorption spectra at a given time point is subtracted from the absorption spectra taken at a time before the pump pulse, which serves as the reference spectra¹⁸⁴. A schematic of a typical fsTA data at a given time point is shown in Figure 6.2. Since a fsTA spectra is a difference spectra, species generated that are not present prior to excitation (pump pulse) or species that increase in concentration show up as a spectral feature with a positive amplitude. Similarly, species present before but reducing in concentration or species disappearing after excitation shows a spectral feature with a negative amplitude. Fluorescence spectra at different times after excitation can also be probed by fsTA spectroscopy utilizing the phenomenon of stimulated emission. Stimulated emission is the phenomenon of photon emission from an excited molecule induced by an incident photon with an energy matching the energy difference of the excited state and ground state (See Figure 6.2).

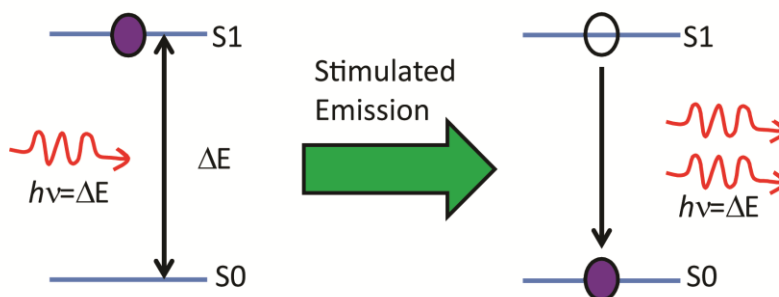


Figure 6.2 Schematic of stimulated emission: A molecule occupying the first excited state (S1) is hit by an incident photon (left panel). The occupancy of the S1 state is represented by a violet circle. This results in stimulated emission when the molecule returns to the S0 state accompanied by emitting a photon that matches the energy difference between S1 and the ground (S0) state and thus is identical to the incident photon (right panel). The occupancy of the S0 state is represented by a violet circle and that the S1 state is not occupied anymore is represented by a transparent circle.

Extrapolating the idea of stimulated emission in the context of fsTA measurement would mean that for frequencies where the energy of the probe pulse photons matches the energy gap between excited state and ground state of the system under investigation, there would be stimulated emission. Due to stimulated emission there would be more photons detected than were in the probe pulse and hence in an fsTA the stimulated emission shows up as a negative spectral feature and corresponds to the fluorescent spectra of the molecule.

A typical fsTA spectra can be described by three primary features, ESA (excited state absorption), BL (ground state bleach) and SE (stimulated emission) (See Figure 6.3)¹⁸⁵. ESA appears as a positive feature describing absorption spectra of the excited state, the BL shows up as a negative feature near the probe pulse describing the decrease in the ground state concentration after excitation and SE shows up as a negative feature describing the fluorescence of the sample.

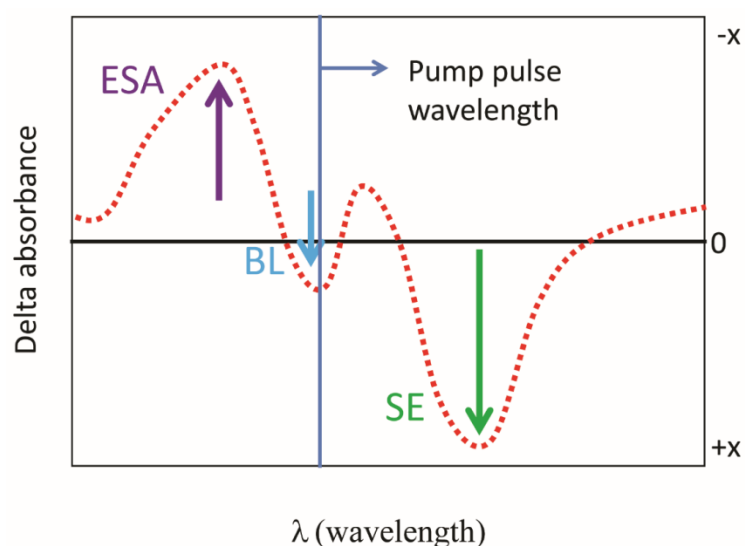


Figure 6.3 Schematic of fsTA spectra: The fsTA data is presented as a difference in absorption over wavelength (delta absorbance) between a spectra taken at a given time after the probe pulse and a reference spectra prior to the probe pulse. Three features are usually identified, ESA (excited state absorption), BL (ground state bleach) and SE (stimulated emission).

6.1.2 TDFSS measurement from SE band from fsTA spectroscopy

Since the SE band in fsTA spectra represents fluorescence emission, one can follow the SE maxima in time and thus follow the TDFSS and measure solvation dynamics. The SE band is not often well resolved in fsTA spectra due to overlap with the BL and ESA band needing complex deconvolution of the spectra¹²³. Hence, it was first necessary to measure a control sample to obtain TDFSS from the SE band of fsTA spectra. For this, I used acrylodan labelled BSA (Bovine Serum Albumin). BSA has a single non oxidized reactive cysteine (Cys-34)¹⁸⁶ residue which I site-specifically conjugated to acrylodan and fsTA spectroscopy was performed on this sample. The fsTA spectra showed a very prominent SE band that showed progressive red shift due to solvation dynamics (See Figure 6.4).

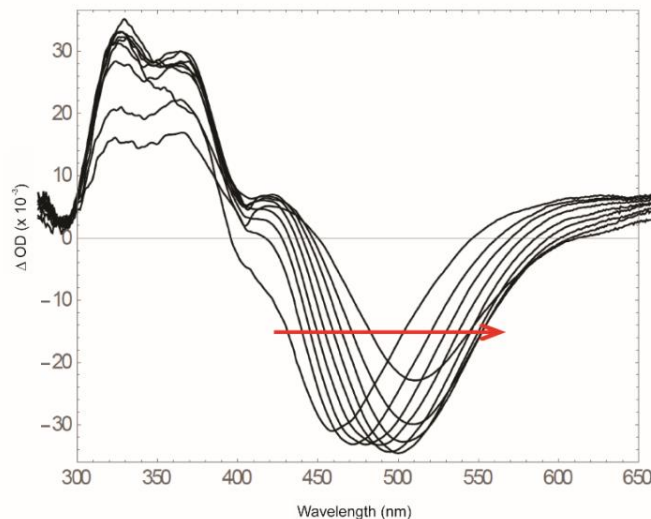


Figure 6.4 fsTA spectra for acrylodan labelled BSA: This experiment was performed by Dr.Kovalenko and Prof.Dr.Ernsting. The fsTA spectra for acrylodan labelled BSA at 0.1 ps, 0.3 ps, 1.0 ps, 3.0 ps, 10 ps, 30 ps, 100 ps, 300 ps and 1000 ps after pump pulse. The spectra shows a well resolved SE band undergoing constant red shift with time (see red arrow).

At each time point the SE band was readily identified in wavelengths near the emission spectra of the molecule. The fsTA spectra was plotted as oscillator distributions ($\Delta OD/\text{wavenumbers}$) and the SE band was fitted to a lognormal line shape with a constant linear background. The relation between fluorescence spectra and oscillator distribution for a given frequency ν , is that fluorescence intensity/ ν^5 is proportional to oscillator strength at ν . The emission frequency at each time point was taken to be an average of frequencies i and ii where they represent the following: i) maxima of the lognormal lineshape fit of the SE band, ii) average of the two half-frequencies where the lognormal lineshape has a value that is half of the maximal value. An example of frequency estimation is shown in Figure 6.5 using a schematic.

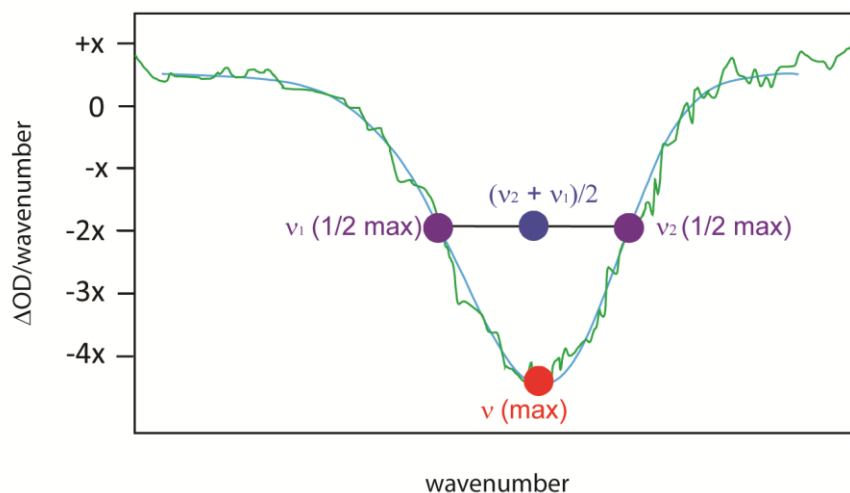


Figure 6.5 Schematic for frequency determination of an SE band of an fsTA spectra: The SE band of an fsTA spectra is plotted as an oscillator distribution ($\Delta OD/\text{wavenumber}$) over wavenumber. The cyan line is a lognormal fit to the data (green line) with a linear background, and the bottom red dot represents the peak value for the log normal while the other two violet dots show the two half points, that is frequencies having half the maximal values. The frequency for each such spectra was taken to be an average of the i) lognormal peak value frequency of the SE band and the ii) average frequency of the two half-points of the spectra shown with a blue dot. Note this is a schematic and not real data.

The frequency obtained at each time points from 100 fs to ~2 ns showed a constant shift of frequency to lower values as shown in Figure 6.6. This showed that the SE band from fsTA spectroscopy of acrylodan labelled samples could be readily used to measure TDFSS without the need for any complex decomposition of the fsTA spectra. In terms of time resolution the addition of fsTA spectroscopy offers 3 orders of magnitude improvement, from ~100 ps (which is close to the typical time resolution from my TCSPC data) to 0.1 ps or 100 fs. However, it was also readily seen that the frequency had a decreasing trend even at the last time points measured using fsTA spectroscopy suggesting that the stokes shift did not converge in the time window of fsTA spectroscopy (~2 ns). This indicated the need for another technique like TCSPC to complement fsTA measurements at longer times to obtain TDFSS data from femtoseconds to nanoseconds.

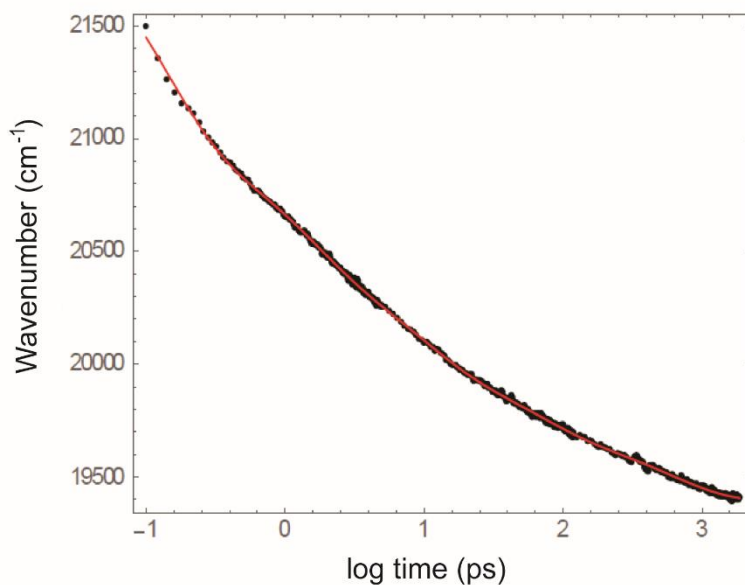


Figure 6.6 TDFSS measured with fsTA spectroscopy on BSA labelled acrylodan: This figure is from Prof.Dr.Ernsting and the experiments were performed by Dr.Kovalenko and Prof.Dr.Ernsting. TDFSS data from the SE band from fsTA spectroscopy on acrylodan labelled BSA (black dots). The red line is a multiexponential fit for a guide to the eye.

6.2 Femtosecond resolved solvation dynamics of IBB and IBB-Importin β

6.2.1 Obtaining TDFSS data from 100 fs to ~15 ns for IBB and IBB-Importin β using a combination of fsTA data and TCSPC data.

After having found that the SE band was very prominently resolved in fsTA spectra of acrylodan labelled BSA and that it was possible to measure TDFSS on such a sample using fsTA spectroscopy by following the shift of the SE band, I performed fsTA experiments on acrylodan labelled IBBS24C in its free disordered state and Importin β bound helical state. The TDFSS was obtained from the SE band, just as was done in the case of BSA (described in the previous section). The TDFSS data clearly showed that the stokes shift was not complete in the time window of fsTA spectroscopy from a declining trend even near the last measured time points (See Figure 6.7). However, some general observations could readily be made. The TDFSS data for free IBBS24C at all times was shifted to lower frequencies compared to that for IBBS4C bound to Importin β . This is in agreement with the spectral blue shift observed in acrylodan labelled IBBS24C upon Importin β binding. The total frequency shift observed for IBBS4C was also more than that observed in presence of Importin β . This is also in consonance with the desolvation of IBB upon Importin β binding as previously described; this is because the total stokes shift reflects the extent of stabilization of the excited state due to solvation dynamics and is directly related to the number of solvating water molecules, with more water molecules in the vicinity causing a larger total shift.

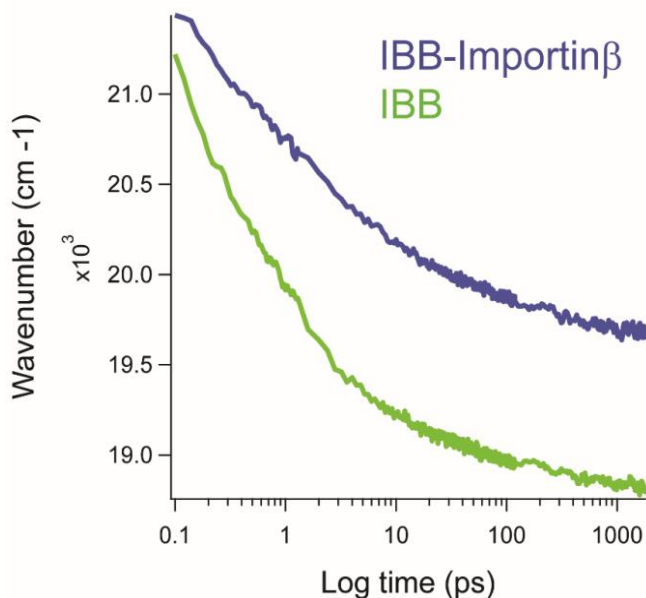


Figure 6.7 TDFSS measured with fsTA spectroscopy on IBB and IBB-Importin β : I performed these experiments in Prof.Dr.Ernsting's Laboratory with Prof.Dr.Ernsting and Dr.Kovalenko. TDFSS data from the SE band from fsTA spectroscopy on acrylodan labelled IBBS4C in its free state (green) and in complex with Importin β (blue).

To extend the time window of the TDFSS to longer times it was essential to complement the fsTA spectroscopy data with the TCSPC data which offers a time window of ~ 20 ns. The TCSPC traces at each wavelength directly describe the rate of intensity decay at wavelengths at longer times where convolution of the IRF does not significantly affect the trace. Thus the raw TCSPC traces at multiple wavelengths contain the information about the rate of fluorescence decays at different wavelengths. However, this information by itself is not sufficient to reconstruct the spectra at different time points without appropriate normalization of the TCSPC traces. fsTA spectroscopy provides the fluorescence oscillator distribution at different times. If a TCSPC trace at a given wavelength λ is normalized at a given time point t to the oscillator strength value at λ using the oscillator strength distribution at time t obtained from fsTA spectroscopy, then the normalized TCSPC trace intensity at any time point is proportional to the fluorescence oscillator strength at λ at that time point. Thus, if a set of TCSPC traces are normalized in this way using fsTA obtained fluorescence oscillator distribution, then all such normalized traces would be proportional to the oscillator strengths at the corresponding wavelengths at any given time. Thus, from such a set of normalized TCSPC traces the oscillator strength distribution and thus the fluorescence spectra can be recovered. The oscillator strength distribution obtained from the normalized TCSPC traces were fitted to a lognormal lineshape and the frequency maxima of such oscillator distributions as a function of time provided the TDFSS at longer times. The process with representative examples are shown in Figure 6.8.

The TDFSS for IBBS24C in presence and absence of Importin β obtained by normalization of TCSPC traces to fsTA spectroscopy obtained oscillator distributions at different times 1000 ps, 1500 ps and 2000 ps, shows almost identical patterns albeit with small (>100 cm^{-1}) systematic offsets in absolute wavenumbers (See Figure 6.8). What we primarily want to learn from TDFSS is the rate of change of frequency with time; thus if the TDFSS data has almost identical patterns irrespective of the time point used for normalization of the TCSPC traces it means that the rate of change of frequency is independent of the time point used for normalization, the vertical offsets could just be corrected. This approach of obtaining TDFSS data from TCSPC traces does not involve fitting the traces to multiexponentials as described in previous sections and is thus comparatively more model free. However, if obtaining TDFSS data only from TCSPC such multiexponentials fittings have to be used as TCSPC traces correspond to intensity decays only at longer times where the IRF convolution can be ignored and hence when solely relying on TCSPC data such an analysis would limit time resolution significantly. However, in this case this is the approach of choice as at earlier times I used the fsTA spectroscopy data.

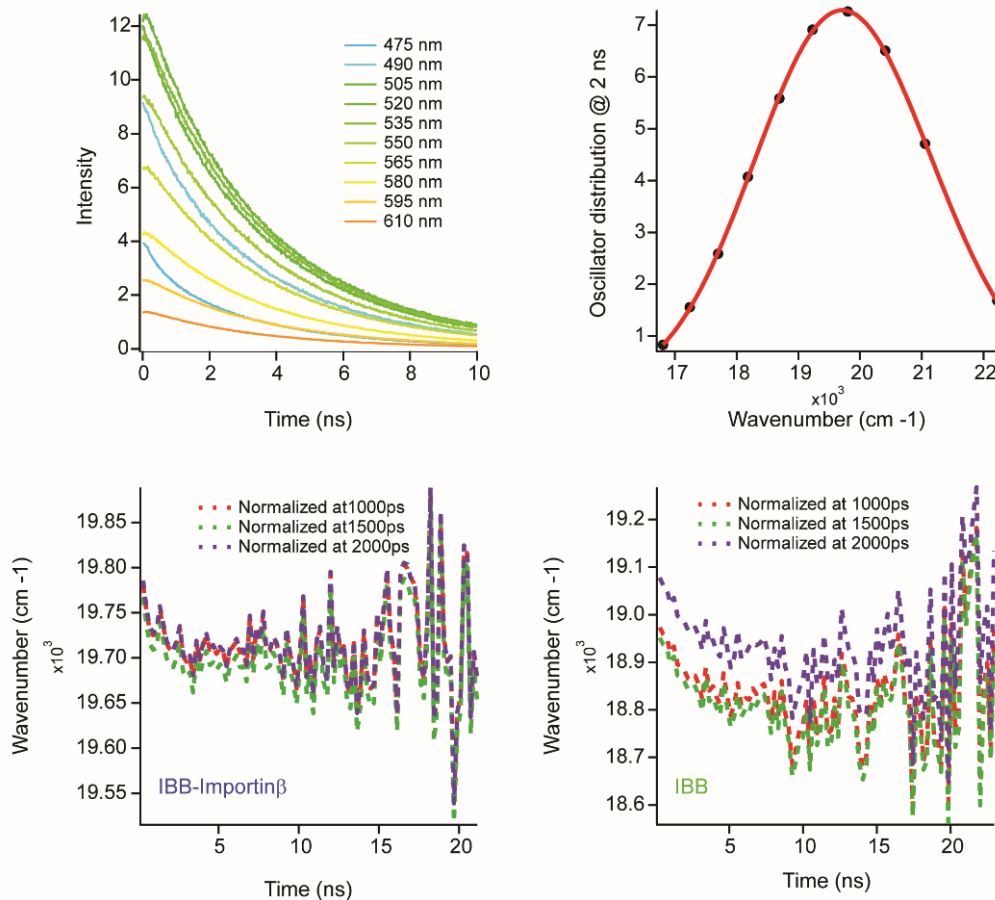


Figure 6.8 TDFSS measured from TCSPC traces normalized to fluorescence oscillator distribution obtained from fsTA spectroscopy: Representative TCSPC traces of IBBS24C in presence of Importin β normalized to the oscillator strength distribution at 1000 ps obtained from fsTA spectroscopy (top left). Oscillator strength distribution obtained from the normalized TCSPC trace (top left) at 2 ns fitted to lognormal lineshape (top right). TDFSS data for IBB-Importin β (bottom left) and IBB (bottom right) obtained from TCSPC traces normalized to fluorescence oscillator distributions from fsTA spectroscopy at 1000 ps, 1500 ps and 2000 ps.

The TDFSS data obtained from normalized TCSPC traces overlapped well with the TDFSS data from the fsTA spectroscopy with small systematic offsets (See Figure 6.9). Finally, the TDFSS data from TCSPC traces normalized to fsTA spectroscopy oscillator distributions at 1000 ps combined with the TDFSS data from fsTA spectroscopy, after correcting for systematic offsets (55 cm^{-1} for free IBB and 45 cm^{-1} for IBB-Importin β), yielded TDFSS data across ~ 5 orders of magnitude in time from 100 fs to ~ 20 ns (See Figure 6.9). The data also clearly showed convergence of stokes shift at longer times indicating that the relaxation process was completed during the measurement. The convergence was validated by simply fitting the stokes shift data from ~ 10 ns - 18 ns with straight line which showed a slope of practically ~ 0 (>0.01 over a time range window of ~ 8 ns). This clearly demonstrated lack of any frequency shift after ~ 10 ns and

thus the fact that within the time window of the combined fsTA and TCSPC data convergence was achieved.

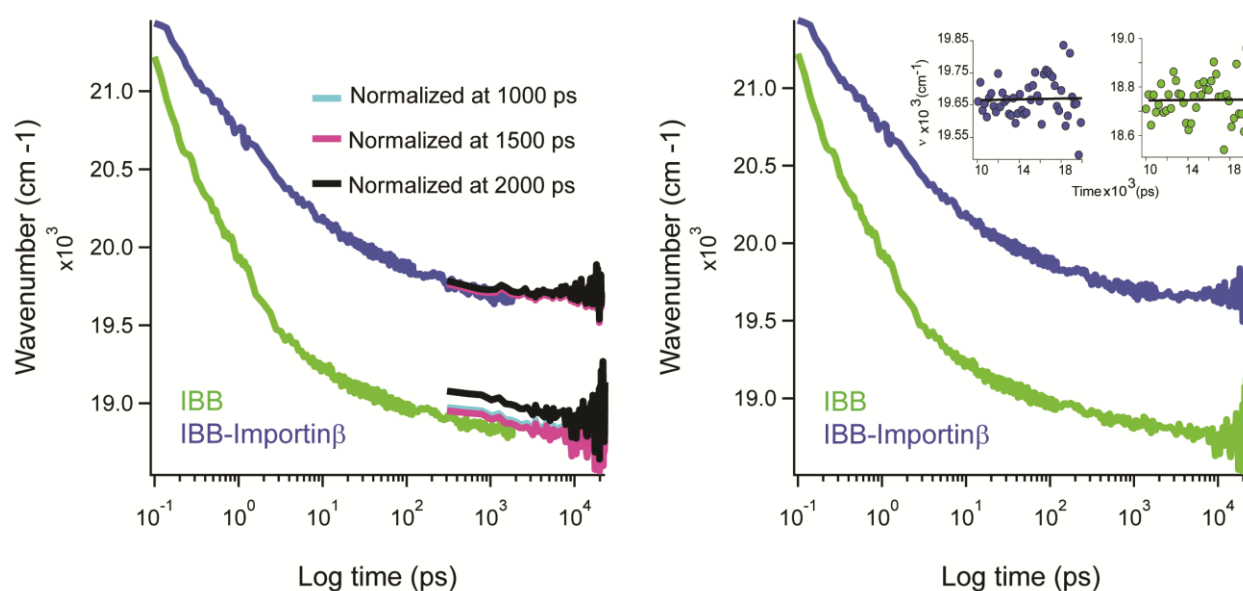


Figure 6.9 TDFSS from 100 fs to ~20 ns from combined fsTA and TCSPC data for IBB and IBB-Importin β : The femtosecond data in the figure is from experiments I performed in Prof. Dr. Ernsting’s laboratory with Prof. Dr. Ernsting and Dr. Kavalenko. An overlay of TDFSS data from fsTA spectroscopy and TCSPC for IBB and IBB-Importin β systems are shown (left). The TDFSS data from fsTA spectroscopy is shown in green and blue for IBB and IBB-Importin β respectively and the TDFSS data from TCSPC is shown in cyan, magenta and black representing data from TCSPC traces normalized to fsTA oscillator distributions at 1000 ps, 1500 ps and 2000 ps. Continuous TDFSS data from 100 fs to 20 ns from combined fsTA and TCSPC data (right) obtained after correcting for a small systematic offset between TDFSS data from fsTA spectroscopy and TCSPC. The TDFSS data for IBB and IBB-Importin β is shown in green and blue respectively. The inset in the right plot shows the TDFSS data between ~10-18 ns for IBB (green) and IBB-Importin β (blue) fitted with a straight line (black) that had a negligible slope indicating no change in frequency in this time range.

6.2.2 Power law nature of solvent response of IBB and IBB-Importin β

The continuous TDFSS data presented as $\nu(t)$ was converted to the normalized solvation correlation function $C(t)$ using Equation 3.10. To obtain $C(t)$ the values for $\nu(0)$ which represents frequency at zero time was obtained by back-interpolation of the TDFSS data upto 0 time. The $\nu(\infty)$ for $C(t)$ calculation which represents the frequency at infinite time, that is when the solvent relaxation process had converged, was obtained by averaging the frequencies of the TDFSS data over the last three nanoseconds when the stokes shift had showed convergence. The $\nu(\infty)$ for acrylodan labelled IBBS24C in free state and in IBB-Importin β was 18774 cm⁻¹ and 19674 cm⁻¹

respectively. The $C(t)$ for IBB-Importin β readily showed a much slower decay compared to that of IBB (See Figure 6.10). The $C(t)$ also highlighted the ultrafast nature of the solvation dynamics, within just 1 ps the $C(t)$ values reached 0.5; since $C(t)$ is a normalized function this indicates ~50% of the solvation was completed for both cases in ~1 ps. The $C(t)$ was also highly non-exponential. Decay of such a non-exponential relaxation function can be described with a continuous probability distribution of time constants $p(\tau)$, as shown in Equation 10.1 where $C(t)$ is the solvation correlation function, τ time constants and t is time.

Equation 10.1

$$C(t) = \int_0^{\infty} p(\tau) e^{-\frac{t}{\tau}} d\tau$$

If $C(t)$ is expressed in terms of rate constants instead of time constants (where rate is the inverse of the time constant such that $e^{-t/\tau} = e^{-kt}$), then a continuous probability distribution of rate constants $p(k)$ describes its decay and Equation 10.1 in that case evolves into equation 10.2.

Equation 10.2

$$C(t) = \int_0^{\infty} p(k) e^{-kt} dk$$

The recovery of $p(k)$ or $p(\tau)$ from $C(t)$ thus involves numerical inversion of Equation 10.1 or 10.2. This is achieved by performing an inverse Laplace transform. Laplace transform $F(s)$ of a function $f(x)$ is given by Equation 10.3. Now if $F(s)$ is the Laplace transform of $f(x)$, the inverse Laplace transform of $f(x)$ is $F(s)$ as shown in Equation 10.4 where \mathcal{L}^{-1} is the inverse Laplace transform. Comparison of Equations 10.2 and 10.3 explains why $C(t)$ can be imagined as a Laplace transform of $p(k)$ and thus explains the need of inverse Laplace transform to recover $p(k)$ from $C(t)$.

Equation 10.3

$$F(s) = \int_0^{\infty} f(x) e^{-sx} dx$$

Equation 10.4

$$\mathcal{L}^{-1} F(s) = f(x) \text{ when } F(s) = \int_0^{\infty} f(x) e^{-sx} dx$$

In reality however, the inversion was performed not on equation 10.2 but on 10.5. This is because the data was spread over 5 orders of magnitude in time.

Equation 10.5

$$C(t) = \int_0^{\infty} p(\log_{10}k) e^{-(\log_{10}k)t} d(\log_{10}k)$$

An inversion of Laplace transform is a numerically ill-posed problem and very sensitive to noise in the data¹⁸⁷. Among the feasible solutions the preferred solution was chosen by a Maximum Entropy Method based criterion, to have a model free solution¹⁸⁷. Inverse Laplace transform has been used to uncover the rate distribution for a wide range of relaxation processes such as NMRT2 relaxation¹⁸⁸ and Dynamic Light Scattering (DLS)¹⁸⁹. An inverse Laplace transform was performed to obtain a probability distribution of rate constants $p(k)$ for the $C(t)$. The rate constants k when converted to time constants τ ($k=1/\tau$), one obtains a probability distribution time constants $p(\tau)$, shown in Figure 6.10. The $p(\tau)$ clearly highlighted the non-exponential nature of the $C(t)$ as there were several very broad and overlapping peaks indicating the lack of a discrete set of time constants behind the decay. The $p(\tau)$ data was plotted in log scale as it covers 5 orders of magnitude in time and hence the peaks in $p(\tau)$ in reality were even broader and overlapping than it appears. Qualitatively the $p(\tau)$ for IBB was dominated by time constants under 10 ps while for IBB-Importin β contribution of slower time constants seemed to increase in agreement with the slower decay of the $C(t)$.

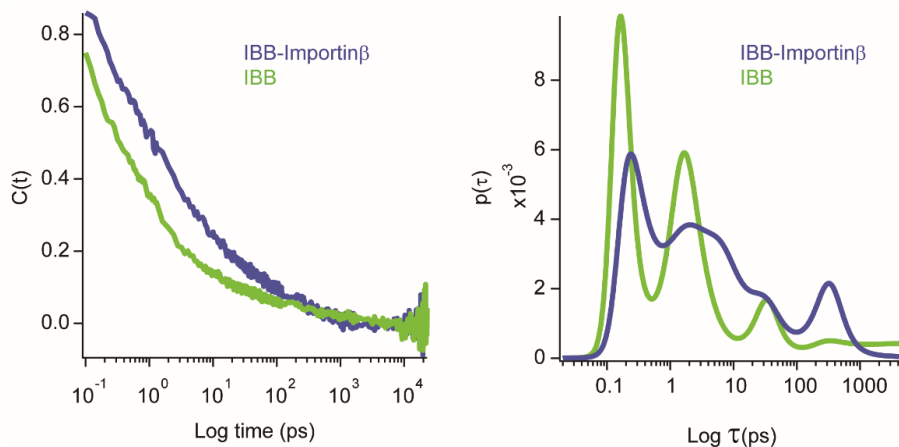


Figure 6.10 $C(t)$ and $p(\tau)$ from inverse Laplace transform of $C(t)$ for IBB and IBB-Importin β : The femtosecond data in the figure is from experiments I performed in Prof. Dr. Ernsting's laboratory with Prof. Dr. Ernsting and Dr. Kovalenko. Data for $p(k)$ was provided by Professor. Dr. Bernhard Dick (University of Regensburg), a colleague of Prof. Dr. Ernsting. $C(t)$ for IBB in green and IBB-Importin β in blue is shown (left). $p(\tau)$ for IBB in green and IBB-Importin β in blue obtained from inverse Laplace transform of $C(t)$ is shown (right).

The lack of discrete exponential time constants governing the $C(t)$ indicates the solvent relaxation process to be more of a continuous type of relaxation. Hence, I tried fitting the TDFSS data for IBB and IBB-Importin β with an empirical powerlaw described equation 10.6, where $\nu(t)$ is the frequency at a given time t , a and b are constants and n is the powerlaw exponent of time.

Equation 10.6

$$\nu(t) = a + bt^{-n}$$

The entire TDFSS data can be fitted nicely to this empirical powerlaw, with minor deviations under 1 ps (Figure 6.11). The powerlaw exponent decreases from 0.34 in IBB to 0.26 in IBB-Importin β (See Figure 6.11). The powerlaw exponent determines the timescales in which the relaxation is dominant, thus a decrease in the exponent means the relaxation progresses to longer times and becomes slower. Thus the reduction in the power law exponent indicates a slowing down of solvation dynamics in IBB across all time scales in comparison to IBB-Importin β .

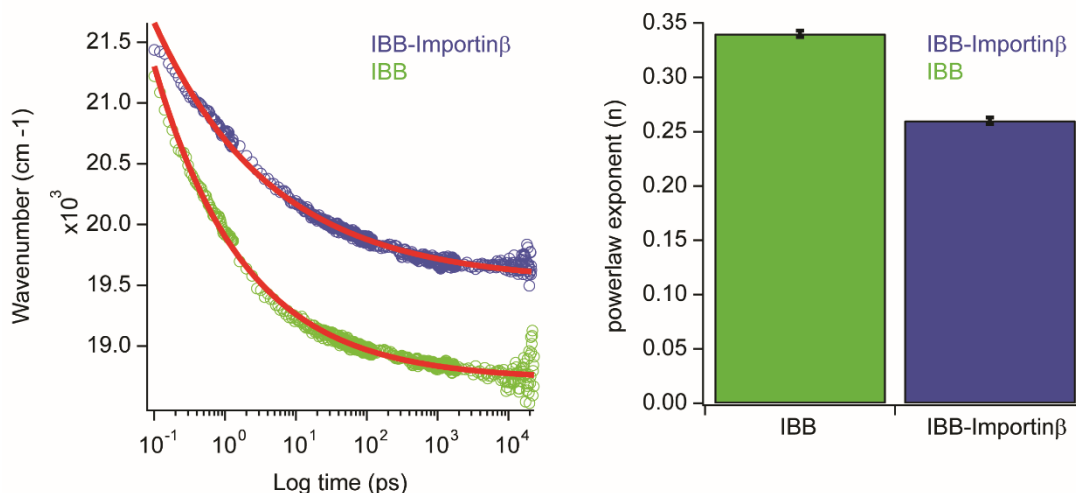


Figure 6.11 type relaxation of solvation in IBB and IBB-Importin β : TDFSS data for IBB (green) and IBB-Importin β (blue) fitted to an empirical powerlaw (red line) is shown (left). The powerlaw exponent for IBB (green) and IBB-Importin β (blue) with error bars representing the error in the fit parameter is shown (right).

These new results highlight a crucial fact that unlike widely reported in literature solvation dynamics on protein is not necessarily governed by discrete timescales^{145,139,177} and can show powerlaw type of relaxation indicating intertwining of multiple timescales and consequently the process giving rise to those timescales which leads to such a collective response. Power law type solvation dynamics had been reported in several different DNAs when probed with intercalating probes as well as base pair mimics^{123,190,191,125}. Even modulation of powerlaw dynamics was seen in DNA with an intercalating fluorophore when a T-T mismatch was introduced; the modulation in this case was an increase of the powerlaw exponent from 0.15 to 0.24 in presence

of the mismatch resulting in a faster relaxation. However, to the best of my knowledge power law type solvation dynamics has never been reported in any protein environment. The exact molecular basis of power law type decay of solvent response is unknown and subject of debate^{192,193,194}. This result shed some new light on protein solvation dynamics in general. The fact that IBB-Importin β solvation dynamics is slower than that of IBB is in agreement with solely TCSPC based measurements mentioned before. fsTA spectroscopy extends the range of times where this slow down happens across all timescales starting from sub-picosecond timescales. This suggests major rearrangement of surface water in IBB upon Importin β binding such that the water dynamics are slowed down. Implications of such slowed dynamics have already been discussed in previous sections; the slowing down of dynamics is likely related to the stabilization of the interface in IBB-Importin β via creating energy barriers from water network rearrangement that impedes disassociation.

Acknowledgements

First and foremost I would like to thank my supervisor Prof. Dr. Edward Lemke for his constant motivation and support over these years. His openness to ideas, ways of approaching a problem and the ability to see the bigger picture has been truly inspirational; his supervision has been instrumental for my holistic development over these years.

I would also like to thank my TAC members Prof. Dr. Michael Knop, Dr. Christoph Müller and Dr. Jonas Ries for their insightful advices and feedbacks during all the TAC meetings.

I would also like to thank the individuals with whom I had the pleasure of collaborating for my project. Their contributions have enriched my project greatly. I would like to thank Prof. Dr. Frauke Gräter and Dr. Davide Mercadante for providing us very useful MD insights to complement my experiments. I would like to thank Prof. Dr. Nikolaus Ernstring and Dr. Sergey Kovalenko for welcoming me in their lab to perform femtosecond spectroscopy, which provided very useful insights.

This journey would not have been as fun if it was not for an amazing set of vibrantly diverse co-workers I had the pleasure of interacting with in our lab. I would like to thank all the past and present members of the Lemke Lab and I consider myself extremely lucky to work in an environment where people share their joys and sorrows with each other everyone stands for the other. I would like to thank Swati for the being the very caring person she always had been. Niccolo for clarifying many fundamentals to me and always bringing an alternate perspective on the table. Jun, for your smile and constant encouragements and sharing my geekiness and enthusiasm for different cuisines. Ivana for all the chitchat moments we had and being a great support. Gemma for all your unique and inspirational perspectives, which you had plenty, illustrator tricks and cloning help. Gustavo thank you some very interesting polymer physics discussions. Christine for holding me by the hand and teaching me almost all the wetlab stuff I know now and being a mobile Wikipedia for protein purification, for bringing in a lot of energy into the lab and most importantly for sharing my pains and excitements. Iker, throughout my PhD I had the pleasure of sitting right across you; thank you for all the chit chat/whisper moments we had across our desks or in your corner, thank you for always having extremely objective and unbiased opinions, for giving some very creative ideas about my project and taking time to proofread portions of my thesis and thank you for always being there. Christopher, thanks for all the new cloning strategies you always bring up, your unique irony, for being the mostly the sole companion in the lab on weekends and for the very interesting conversations and for proofreading my thesis sections with very short notices. Piau, for all your advices and 'I am sceptical' comments that made me think about things much more rigorously and patiently answering all my optics questions. Giorgia for being the extremely positive person you are and

answering many of my microfluidic questions. Giulia for always answering all my questions about physical models and their appropriateness and many other fruitful discussions. Sofya for your very 'British' sharp yet seasoned sense of humour and sarcasm that never fails to liven up the atmosphere. Natalia for help whenever I had to synthesize something and chemistry you bring in the group meetings that sends me back nostalgically to my organic lecture in University. Joana for contributing to positive atmosphere and making sure that the lab runs in order. Daniel thanks for all your help on the software we use to analyse data. Paul for all your jokes and the fun moments.

I am also grateful to my previous supervisors Prof. Dr. K. P. Das, Dr. R. Banerjee and Dr. S.W. Magennis with whom I had the opportunity to work throughout my bachelors and who were instrumental in developing my knack for fluorescence spectroscopy and biophysics.

Outside the lab I was also privileged enough to have befriended some unique individuals in EMBL who made my stay very pleasant. I would like to thank Shweta, Shyamal, Prasad, Julius, Mainak, Neha, Jurgen and Mevlut for their constant support and encouragement.

I am also indebted to my friends from University and School, whom I always found by my side. I would like to thank Dutta, Arka, Sarbotrika, Rajdeep, Deep, Anish, Upasak, Azam, Tawseef, Shahneela, Athar and Jayanta for being there through thick and thin (though going by sizes it would mostly be thick in my case). You guys had been family to me and I am privileged to have known you. Distance never stopped you from being there beside me whenever I needed you.

Whatever I am today it's in large parts due to the support and love I had for my family. I would like to thank my uncle and aunty for being the degenerate set of parents when I was growing up, my sister for the wonderful person she is and the strong support she always had been; I really do not know how having my own sister would have been any different. I would like to thank my maternal grandma for all those afternoons after school when she would engage me with the most interesting stories and for her immeasurable love for me. I owe >50% of my vocabulary to her, thanks to her reading to me Enid Blyton or Roald Dahl and eventually Mark Twain, Shakespeare and the likes every day when I would come back from school.

Finally, I would like to thank my parents, however the attempt itself is futile as I probably cannot thank them enough. Thank you for being there in every step of my life, for walking that extra mile or rather miles to realize my dreams, for defining for me integrity, work ethics and the value of excellence, for always patronizingly encouraging my curiosity and never suppressing it and most importantly for making me firmly believe that I could potentially never dig a hole deep enough from which you guys cannot rescue me. If rebirth exists, I would like to be born of you guys again.

Bibliography

1. Redfern, O. C.; Dessailly, B.; Orengo, C. A., Exploring the structure and function paradigm. *Current Opinion in Structural Biology* **2008**, *18* (3), 394-402.
2. Martínez Cuesta, S.; Rahman, Syed A.; Furnham, N.; Thornton, Janet M., The Classification and Evolution of Enzyme Function. *Biophysical Journal* **2015**, *109* (6), 1082-1086.
3. Catazaro, J.; Caprez, A.; Guru, A.; Swanson, D.; Powers, R., Functional Evolution of PLP-dependent Enzymes based on Active-Site Structural Similarities. *Proteins* **2014**, *82* (10), 2597-2608.
4. Kriwacki, R. W.; Hengst, L.; Tennant, L.; Reed, S. I.; Wright, P. E., Structural studies of p21Waf1/Cip1/Sdi1 in the free and Cdk2-bound state: conformational disorder mediates binding diversity. *Proc Natl Acad Sci U S A* **1996**, *93* (21), 11504-9.
5. Boesch, C.; Bundi, A.; Oppliger, M.; Wüthrich, K., ¹H Nuclear-Magnetic-Resonance Studies of the Molecular Conformation of Monomeric Glucagon in Aqueous Solution. *European Journal of Biochemistry* **1978**, *91* (1), 209-214.
6. Torchia, J.; Rose, D. W.; Inostroza, J.; Kamei, Y.; Westin, S.; Glass, C. K.; Rosenfeld, M. G., The transcriptional co-activator p/CIP binds CBP and mediates nuclear-receptor function. *Nature* **1997**, *387*, 677.
7. Nolte, R. T.; Wisely, G. B.; Westin, S.; Cobb, J. E.; Lambert, M. H.; Kurokawa, R.; Rosenfeld, M. G.; Willson, T. M.; Glass, C. K.; Milburn, M. V., Ligand binding and co-activator assembly of the peroxisome proliferator-activated receptor- γ . *Nature* **1998**, *395*, 137.
8. Dunker, A. K.; Babu, M. M.; Barbar, E.; Blackledge, M.; Bondos, S. E.; Dosztanyi, Z.; Dyson, H. J.; Forman-Kay, J.; Fuxreiter, M.; Gsponer, J.; Han, K. H.; Jones, D. T.; Longhi, S.; Metallo, S. J.; Nishikawa, K.; Nussinov, R.; Obradovic, Z.; Pappu, R. V.; Rost, B.; Selenko, P.; Subramaniam, V.; Sussman, J. L.; Tompa, P.; Uversky, V. N., What's in a name? Why these proteins are intrinsically disordered: Why these proteins are intrinsically disordered. *Intrinsically Disord Proteins* **2013**, *1* (1), e24157.
9. Wright, P. E.; Dyson, H. J., Intrinsically unstructured proteins: re-assessing the protein structure-function paradigm. *J Mol Biol* **1999**, *293* (2), 321-31.
10. Pentony, M. M.; Ward, J.; Jones, D. T., Computational resources for the prediction and analysis of native disorder in proteins. *Methods Mol Biol* **2010**, *604*, 369-93.
11. Dunker, a. K.; Brown, C. J.; Obradovic, Z., Identification and functions of usefully disordered proteins. *Advances in Protein Chemistry* **2002**, *62*, 25-49.
12. Dunker, a. K.; Obradovic, Z.; Romero, P.; Garner, E. C.; Brown, C. J., Intrinsic protein disorder in complete genomes. *Genome informatics. Workshop on Genome Informatics* **2000**, *11*, 161-171.
13. Pentony, M. M.; Jones, D. T., Modularity of intrinsic disorder in the human proteome. *Proteins* **2010**, *78* (1), 212-21.
14. Kafri, M.; Metzl-Raz, E.; Jona, G.; Barkai, N., The Cost of Protein Production. *Cell Reports* **2016**, *14* (1), 22-31.
15. Ward, J. J.; Sodhi, J. S.; McGuffin, L. J.; Buxton, B. F.; Jones, D. T., Prediction and functional analysis of native disorder in proteins from the three kingdoms of life. *J Mol Biol* **2004**, *337* (3), 635-45.
16. Dunker, A. K.; Cortese, M. S.; Romero, P.; Iakoucheva, L. M.; Uversky, V. N., Flexible nets. The roles of intrinsic disorder in protein interaction networks. *FEBS J* **2005**, *272* (20), 5129-48.
17. Babu, M. M., The contribution of intrinsically disordered regions to protein function, cellular complexity, and human disease. *Biochemical Society Transactions* **2016**, *44* (5), 1185-1200.
18. Uversky, V. N.; Gillespie, J. R.; Fink, A. L., Why are "natively unfolded" proteins unstructured under physiologic conditions? *Proteins: Structure, Function, and Bioinformatics* **2000**, *41* (3), 415-427.

19. Dyson, H. J.; Wright, P. E., Coupling of folding and binding for unstructured proteins. *Current Opinion in Structural Biology* **2002**, *12* (1), 54-60.
20. Fuxreiter, M.; Tompa, P., Fuzzy interactome: the limitations of models in molecular biology. *Trends in Biochemical Sciences* **2009**, *34* (1), 3-3.
21. Sharma, R.; Raduly, Z.; Miskei, M.; Fuxreiter, M., Fuzzy complexes: Specific binding without complete folding. *FEBS Letters* **2015**.
22. Tompa, P.; Fuxreiter, M., Fuzzy complexes: polymorphism and structural disorder in protein–protein interactions.
23. Wright, P. E.; Dyson, H. J., Linking folding and binding. *Current Opinion in Structural Biology* **2009**, *19* (1), 31-38.
24. Shammas, S. L.; Crabtree, M. D.; Dahal, L.; Wicky, B. I. M.; Clarke, J., Insights into coupled folding and binding mechanisms from kinetic studies. *Journal of Biological Chemistry* **2016**, *291* (13), 6689-6695.
25. Milles, S.; Mercadante, D.; Aramburu, I. V.; Jensen, M. R. b.; Banterle, N.; Koehler, C.; Tyagi, S.; Clarke, J.; Shammas, S. L.; Blackledge, M.; Gräter, F.; Lemke, E. A., Plasticity of an Ultrafast Interaction between Nucleoporins and Nuclear Transport Receptors. *Cell* **2015**, *163* (3), 734-745.
26. Mittag, T.; Orlicky, S.; Choy, W.-Y.; Tang, X.; Lin, H.; Sicheri, F.; Kay, L. E.; Tyers, M.; Forman-Kay, J. D., Dynamic equilibrium engagement of a polyvalent ligand with a single-site receptor. *Proceedings of the National Academy of Sciences* **2008**, *105* (46), 17772.
27. Dinkel, H.; Van Roey, K.; Michael, S.; Davey, N. E.; Weatheritt, R. J.; Born, D.; Speck, T.; Kruger, D.; Grebnev, G.; Kuban, M.; Strumillo, M.; Uyar, B.; Budd, A.; Altenberg, B.; Seiler, M.; Chemes, L. B.; Glavina, J.; Sanchez, I. E.; Diella, F.; Gibson, T. J., The eukaryotic linear motif resource ELM: 10 years and counting. *Nucleic Acids Res* **2014**, *42* (Database issue), D259-66.
28. Fuxreiter, M.; Tompa, P.; Simon, I., Local structural disorder imparts plasticity on linear motifs. *Bioinformatics* **2007**, *23* (8), 950-956.
29. Liu, J.; Perumal, N. B.; Oldfield, C. J.; Su, E. W.; Uversky, V. N.; Dunker, A. K., Intrinsic disorder in transcription factors. *Biochemistry* **2006**, *45* (22), 6873-6888.
30. Staby, L.; Shea, C.; Willemoës, M.; Theisen, F.; Kragelund, B. B.; Skriver, K., Eukaryotic transcription factors: paradigms of protein intrinsic disorder. *Biochemical Journal* **2017**, *474* (15), 2509.
31. Hansen, J. C.; Lu, X.; Ross, E. D.; Woody, R. W., Intrinsic Protein Disorder, Amino Acid Composition, and Histone Terminal Domains. *Journal of Biological Chemistry* **2006**, *281* (4), 1853-1856.
32. Wright, P. E.; Dyson, H. J., Intrinsically Disordered Proteins in Cellular Signaling and Regulation. *Nature reviews. Molecular cell biology* **2015**, *16* (1), 18-29.
33. Dyson, H. J.; Wright, P. E., Role of Intrinsic Protein Disorder in the Function and Interactions of the Transcriptional Coactivators CREB-binding Protein (CBP) and p300. *The Journal of Biological Chemistry* **2016**, *291* (13), 6714-6722.
34. Szklarczyk, D.; Franceschini, A.; Wyder, S.; Forslund, K.; Heller, D.; Huerta-Cepas, J.; Simonovic, M.; Roth, A.; Santos, A.; Tsafou, K. P.; Kuhn, M.; Bork, P.; Jensen, L. J.; von Mering, C., STRING v10: protein–protein interaction networks, integrated over the tree of life. *Nucleic Acids Research* **2015**, *43* (Database issue), D447-D452.
35. Uversky, V. N., p53 Proteoforms and Intrinsic Disorder: An Illustration of the Protein Structure–Function Continuum Concept. *International Journal of Molecular Sciences* **2016**, *17* (11), 1874.
36. Izzo, A.; Schneider, R., The role of linker histone H1 modifications in the regulation of gene expression and chromatin dynamics. *Biochimica et Biophysica Acta (BBA) - Gene Regulatory Mechanisms* **2016**, *1859* (3), 486-495.
37. Xu, Y., Regulation of p53 responses by post-translational modifications. *Cell Death And Differentiation* **2003**, *10*, 400.

38. Hofmann, H.; Soranno, a.; Borgia, a.; Gast, K.; Nettels, D.; Schuler, B., Polymer scaling laws of unfolded and intrinsically disordered proteins quantified with single-molecule spectroscopy. *Proceedings of the National Academy of Sciences* **2012**, *109* (40), 16155-16160.
39. Brangwynne, Clifford P.; Tompa, P.; Pappu, Rohit V., Polymer physics of intracellular phase transitions. *Nature Physics* **2015**, *11*, 899.
40. Feric, M.; Vaidya, N.; Harmon, T. S.; Mitrea, D. M.; Zhu, L.; Richardson, T. M.; Kriwacki, R. W.; Pappu, R. V.; Brangwynne, C. P., Coexisting Liquid Phases Underlie Nucleolar Subcompartments. *Cell* **2016**, *165* (7), 1686-1697.
41. Brangwynne, C. P.; Mitchison, T. J.; Hyman, A. A., Active liquid-like behavior of nucleoli determines their size and shape in *Xenopus laevis* oocytes. *Proc Natl Acad Sci U S A* **2011**, *108* (11), 4334-9.
42. Nott, T. J.; Petsalaki, E.; Farber, P.; Jarvis, D.; Fussner, E.; Plochowitz, A.; Craggs, T. D.; Bazett-Jones, D. P.; Pawson, T.; Forman-Kay, J. D.; Baldwin, A. J., Phase transition of a disordered nuage protein generates environmentally responsive membraneless organelles. *Mol Cell* **2015**, *57* (5), 936-47.
43. Brangwynne, C. P.; Eckmann, C. R.; Courson, D. S.; Rybarska, A.; Hoegge, C.; Gharakhani, J.; Julicher, F.; Hyman, A. A., Germline P granules are liquid droplets that localize by controlled dissolution/condensation. *Science* **2009**, *324* (5935), 1729-32.
44. Buchan, J. R.; Parker, R., Eukaryotic Stress Granules : The Ins and Out of Translation. *Mol Cell* **2009**, *36* (6).
45. Schmidt, H. B.; Görlich, D., Transport Selectivity of Nuclear Pores, Phase Separation, and Membraneless Organelles. *Trends in Biochemical Sciences* **2016**, *41* (1), 46-61.
46. Kabachinski, G.; Schwartz, T. U., The nuclear pore complex – structure and function at a glance. *Journal of Cell Science* **2015**, *128* (3), 423-429.
47. Beck, M.; Lučić, V.; Förster, F.; Baumeister, W.; Medalia, O., Snapshots of nuclear pore complexes in action captured by cryo-electron tomography. *Nature* **2007**, *449*, 611.
48. Beck, M.; Hurt, E., The nuclear pore complex: understanding its function through structural insight. *Nat Rev Mol Cell Biol* **2017**, *18* (2), 73-89.
49. von Appen, A.; Kosinski, J.; Sparks, L.; Ori, A.; DiGuilio, A. L.; Vollmer, B.; Mackmull, M. T.; Banterle, N.; Parca, L.; Kastiris, P.; Buczak, K.; Mosalaganti, S.; Hagen, W.; Andres-Pons, A.; Lemke, E. A.; Bork, P.; Antonin, W.; Glavy, J. S.; Bui, K. H.; Beck, M., In situ structural analysis of the human nuclear pore complex. *Nature* **2015**, *526* (7571), 140-3.
50. Kosinski, J.; Mosalaganti, S.; von Appen, A.; Teimer, R.; DiGuilio, A. L.; Wan, W.; Bui, K. H.; Hagen, W. J.; Briggs, J. A.; Glavy, J. S.; Hurt, E.; Beck, M., Molecular architecture of the inner ring scaffold of the human nuclear pore complex. *Science* **2016**, *352* (6283), 363-5.
51. Denning, D. P.; Patel, S. S.; Uversky, V.; Fink, A. L.; Rexach, M., Disorder in the nuclear pore complex: the FG repeat regions of nucleoporins are natively unfolded. *Proc Natl Acad Sci U S A* **2003**, *100* (5), 2450-5.
52. Patel, S. S.; Belmont, B. J.; Sante, J. M.; Rexach, M. F., Natively Unfolded Nucleoporins Gate Protein Diffusion across the Nuclear Pore Complex. *Cell* **2007**, *129* (1), 83-96.
53. Timney, B. L.; Raveh, B.; Mironska, R.; Trivedi, J. M.; Kim, S. J.; Russel, D.; Wenthe, S. R.; Sali, A.; Rout, M. P., Simple rules for passive diffusion through the nuclear pore complex. *The Journal of Cell Biology* **2016**.
54. Görlich, D., Transport into and out of the cell nucleus. *The EMBO Journal* **1998**, *17* (10), 2721-2727.
55. Cushman, I.; Palzkill, T.; Moore, M. S., Using peptide arrays to define nuclear carrier binding sites on nucleoporins. *Methods* **2006**, *39* (4), 329-41.
56. Hallberg, E.; Wozniak, R. W.; Blobel, G., An integral membrane protein of the pore membrane domain of the nuclear envelope contains a nucleoporin-like region. *J Cell Biol* **1993**, *122* (3), 513-21.

57. Radu, A.; Moore, M. S.; Blobel, G., The peptide repeat domain of nucleoporin Nup98 functions as a docking site in transport across the nuclear pore complex. *Cell* **1995**, *81* (2), 215-22.
58. Wentte, S. R.; Rout, M. P.; Blobel, G., A new family of yeast nuclear pore complex proteins. *J Cell Biol* **1992**, *119* (4), 705-23.
59. Wentte, S. R.; Blobel, G., NUP145 encodes a novel yeast glycine-leucine-phenylalanine-glycine (GLFG) nucleoporin required for nuclear envelope structure. *J Cell Biol* **1994**, *125* (5), 955-69.
60. Strawn, L. A.; Shen, T.; Shulga, N.; Goldfarb, D. S.; Wentte, S. R., Minimal nuclear pore complexes define FG repeat domains essential for transport. *Nature Cell Biology* **2004**, *6*, 197.
61. Denning, D. P.; Rexach, M. F., Rapid evolution exposes the boundaries of domain structure and function in natively unfolded FG nucleoporins. *Mol Cell Proteomics* **2007**, *6* (2), 272-282.
62. Schmidt, H. B.; Görlich, D.; Kohler, A.; Bradatsch, B.; Bassler, J.; Hurt, E.; Reza, R.; Acheson, J.; Krishnan, V. V.; Newsam, S.; Gopinathan, A.; Lau, E. Y.; Colvin, M. E.; Uversky, V. N.; Rexach, M. F., Nup98 FG domains from diverse species spontaneously phase-separate into particles with nuclear pore-like permselectivity. *eLife* **2015**, *4*, 51-62.
63. Naim, B.; Zbaida, D.; Dagan, S.; Kapon, R.; Reich, Z., Cargo surface hydrophobicity is sufficient to overcome the nuclear pore complex selectivity barrier. *The EMBO Journal* **2009**, *28* (18), 2697-2705.
64. Ribbeck, K.; Görlich, D., The permeability barrier of nuclear pore complexes appears to operate via hydrophobic exclusion. *The EMBO Journal* **2002**, *21* (11), 2664-2671.
65. Yamada, J.; Phillips, J. L.; Patel, S.; Goldfien, G.; Calestagne-Morelli, A.; Huang, H.; Reza, R.; Acheson, J.; Krishnan, V. V.; Newsam, S.; Gopinathan, A.; Lau, E. Y.; Colvin, M. E.; Uversky, V. N.; Rexach, M. F., A bimodal distribution of two distinct categories of intrinsically disordered structures with separate functions in FG nucleoporins. *Mol Cell Proteomics* **2010**, *9* (10), 2205-24.
66. Fuertes, G.; Banterle, N.; Ruff, K. M.; Chowdhury, A.; Mercadante, D.; Koehler, C.; Kachala, M.; Estrada Girona, G.; Milles, S.; Mishra, A.; Onck, P. R.; Gräter, F.; Esteban-Martín, S.; Pappu, R. V.; Svergun, D. I.; Lemke, E. A., Decoupling of size and shape fluctuations in heteropolymeric sequences reconciles discrepancies in SAXS vs. FRET measurements. *Proceedings of the National Academy of Sciences* **2017**, *114* (31), E6342-E6351.
67. Labokha, A. A.; Gradmann, S.; Frey, S.; Hü Lsmann, B. B.; Urlaub, H.; Baldus, M.; Görlich, D., Systematic analysis of barrier-forming FG hydrogels from *Xenopus* nuclear pore complexes. *The EMBO Journal* **2013**, *32302*, 204-218.
68. Frey, S.; Görlich, D., A Saturated FG-Repeat Hydrogel Can Reproduce the Permeability Properties of Nuclear Pore Complexes. *Cell* **2007**.
69. Lim, R. Y.; Fahrenkrog, B.; Koser, J.; Schwarz-Herion, K.; Deng, J.; Aebi, U., Nanomechanical basis of selective gating by the nuclear pore complex. *Science* **2007**, *318* (5850), 640-3.
70. Lim, R. Y. H.; Huang, B.; Kapinos, L. E., How to operate a nuclear pore complex by Kap-centric control. *Nucleus* **2015**, *6* (5), 366-372.
71. Eisele, N. B.; Frey, S.; Piehler, J.; Görlich, D.; Richter, R. P., Ultrathin nucleoporin phenylalanine-glycine repeat films and their interaction with nuclear transport receptors. *EMBO Reports* **2010**, *11* (5), 366-372.
72. Zahn, R.; Osmanović, D.; Ehret, S.; Araya Callis, C.; Frey, S.; Stewart, M.; You, C.; Görlich, D.; Hoogenboom, B. W.; Richter, R. P., A physical model describing the interaction of nuclear transport receptors with FG nucleoporin domain assemblies. *eLife* **2016**, *5*, e14119.
73. Vovk, A.; Gu, C.; Opferman, M. G.; Kapinos, L. E.; Lim, R. Y. H.; Coalson, R. D.; Jasnow, D.; Zilman, A., Simple biophysics underpins collective conformations of the intrinsically disordered proteins of the Nuclear Pore Complex. *eLife* **2016**, *5*, e10785.
74. Moroianu, J., Distinct nuclear import and export pathways mediated by members of the karyopherin beta family. *J Cell Biochem* **1998**, *70* (2), 231-9.

75. O'Reilly, A. J.; Dacks, J. B.; Field, M. C.; Brenner, S. E.; Chervitz, S. A., Evolution of the Karyopherin- β Family of Nucleocytoplasmic Transport Factors; Ancient Origins and Continued Specialization. *PLoS ONE* **2011**, *6* (4), e19308-e19308.
76. Chook, Y. M.; Blobel, G., Structure of the nuclear transport complex karyopherin-beta2-Ran x GppNHp. *Nature* **1999**, *399* (6733), 230-7.
77. Cingolani, G.; Petosa, C.; Weis, K.; Muller, C. W., Structure of importin-beta bound to the IBB domain of importin-alpha. *Nature* **1999**, *399* (6733), 221-9.
78. Monecke, T.; Haselbach, D.; Voss, B.; Russek, A.; Neumann, P.; Thomson, E.; Hurt, E.; Zachariae, U.; Stark, H.; Grubmüller, H.; Dickmanns, A.; Ficner, R., Structural basis for cooperativity of CRM1 export complex formation. *Proc Natl Acad Sci U S A* **2013**, *110* (3), 960-5.
79. Conti, E.; Muller, C. W.; Stewart, M., Karyopherin flexibility in nucleocytoplasmic transport. *Curr Opin Struct Biol* **2006**, *16* (2), 237-44.
80. Fukuhara, N.; Fernandez, E.; Ebert, J.; Conti, E.; Svergun, D., Conformational variability of nucleocytoplasmic transport factors. *The Journal of biological chemistry* **2004**, *279* (3), 2176-81.
81. Halder, K.; Dölker, N.; Van, Q.; Gregor, I.; Dickmanns, A.; Baade, I.; Kehlenbach, Ralph H.; Ficner, R.; Enderlein, J.; Grubmüller, H.; Neumann, H., MD Simulations and FRET Reveal an Environment-Sensitive Conformational Plasticity of Importin- β . *Biophysical Journal* **2015**, *109* (2), 277-286.
82. Bayliss, R.; Leung, S. W.; Baker, R. P.; Quimby, B. B.; Corbett, A. H.; Stewart, M., Structural basis for the interaction between NTF2 and nucleoporin FxFG repeats. *EMBO J* **2002**, *21* (12), 2843-53.
83. Aibara, S.; Katahira, J.; Valkov, E.; Stewart, M., The principal mRNA nuclear export factor NXF1:NXT1 forms a symmetric binding platform that facilitates export of retroviral CTE-RNA. *Nucleic Acids Research* **2015**, *43* (3), 1883-1893.
84. Finlay, D. R.; Forbes, D. J., Reconstitution of biochemically altered nuclear pores: transport can be eliminated and restored. *Cell* **1990**, *60* (1), 17-29.
85. Lubas, W. A.; Smith, M.; Starr, C. M.; Hanover, J. A., Analysis of nuclear pore protein p62 glycosylation. *Biochemistry* **1995**, *34* (5), 1686-94.
86. Gorlich, D.; Pante, N.; Kutay, U.; Aebi, U.; Bischoff, F. R., Identification of different roles for RanGDP and RanGTP in nuclear protein import. *EMBO J* **1996**, *15* (20), 5584-94.
87. Kehlenbach, R. H.; Dickmanns, A.; Kehlenbach, A.; Guan, T.; Gerace, L., A role for RanBP1 in the release of CRM1 from the nuclear pore complex in a terminal step of nuclear export. *J Cell Biol* **1999**, *145* (4), 645-57.
88. Seedorf, M.; Damelin, M.; Kahana, J.; Taura, T.; Silver, P. A., Interactions between a nuclear transporter and a subset of nuclear pore complex proteins depend on Ran GTPase. *Mol Cell Biol* **1999**, *19* (2), 1547-57.
89. Yaseen, N. R.; Blobel, G., GTP hydrolysis links initiation and termination of nuclear import on the nucleoporin nup358. *J Biol Chem* **1999**, *274* (37), 26493-502.
90. Bayliss, R.; Littlewood, T.; Strawn, L. A.; Wente, S. R.; Stewart, M., GLFG and FxFG nucleoporins bind to overlapping sites on importin-beta. *J Biol Chem* **2002**, *277* (52), 50597-606.
91. Isgro, T. A.; Schulten, K., Binding Dynamics of Isolated Nucleoporin Repeat Regions to Importin- β . *Structure* **2005**, *13* (12), 1869-1879.
92. Isgro, T. A.; Schulten, K., Association of Nuclear Pore FG-repeat Domains to NTF2 Import and Export Complexes. *Journal of Molecular Biology* **2007**, *366* (1), 330-345.
93. Otsuka, S.; Iwasaka, S.; Yoneda, Y.; Takeyasu, K.; Yoshimura, S. H., Individual binding pockets of importin-beta for FG-nucleoporins have different binding properties and different sensitivities to RanGTP. *Proceedings of the National Academy of Sciences of the United States of America* **2008**, *105* (42), 16101-16106.
94. Kubitschek, U.; Grünwald, D.; Hoekstra, A.; Rohleder, D.; Kues, T.; Siebrasse, J. P.; Peters, R., Nuclear transport of single molecules. *The Journal of Cell Biology* **2005**, *168* (2).

95. Musser, S. M.; Grunwald, D., Deciphering the Structure and Function of Nuclear Pores Using Single-Molecule Fluorescence Approaches. *J Mol Biol* **2016**, *428* (10 Pt A), 2091-119.
96. Sun, C.; Fu, G.; Ciziene, D.; Stewart, M.; Musser, S. M., Choreography of importin-alpha/CAS complex assembly and disassembly at nuclear pores. *Proc Natl Acad Sci U S A* **2013**, *110* (17), E1584-93.
97. Yang, C. H.; Kuo, W. T.; Chuang, Y. T.; Chen, C. Y.; Lin, C. C., Cyclin B1 destruction box-mediated protein instability: the enhanced sensitivity of fluorescent-protein-based reporter gene system. *Biomed Res Int* **2013**, *2013*, 732307.
98. Bednenko, J.; Cingolani, G.; Gerace, L., Importin beta contains a COOH-terminal nucleoporin binding region important for nuclear transport. *J Cell Biol* **2003**, *162* (3), 391-401.
99. Ben-Efraim, I.; Gerace, L., Gradient of increasing affinity of importin beta for nucleoporins along the pathway of nuclear import. *J Cell Biol* **2001**, *152* (2), 411-7.
100. Milles, S.; Lemke, E. A., Mapping Multivalency and Differential Affinities within Large Intrinsically Disordered Protein Complexes with Segmental Motion Analysis. *Angewandte Chemie International Edition* **2014**, *53* (28), 7364-7367.
101. Tetenbaum-Novatt, J.; Hough, L. E.; Mironska, R.; McKenney, A. S.; Rout, M. P., Nucleocytoplasmic transport: a role for nonspecific competition in karyopherin-nucleoporin interactions. *Mol Cell Proteomics* **2012**, *11* (5), 31-46.
102. Aramburu, I. V.; Lemke, E. A., Floppy but not sloppy: Interaction mechanism of FG-nucleoporins and nuclear transport receptors. *Seminars in Cell & Developmental Biology* **2017**, *68*, 34-41.
103. Sparks, S.; Temel, D. B.; Rout, M. P.; Cowburn, D., Deciphering the "Fuzzy" Interaction of FG Nucleoporins and Transport Factors Using Small-Angle Neutron Scattering. *Structure* **2018**, *26* (3), 477-484.e4.
104. Spaar, A.; Dammer, C.; Gabdoulline, R. R.; Wade, R. C.; Helms, V., Diffusional Encounter of Barnase and Barstar. *Biophysical Journal* **2006**, *90* (6), 1913-1924.
105. Hough, L. E.; Dutta, K.; Sparks, S.; Temel, D. B.; Kamal, A.; Tetenbaum-Novatt, J.; Rout, M. P.; Cowburn, D., The molecular mechanism of nuclear transport revealed by atomic-scale measurements. *eLife* **2015**, *4* (September), 1-23.
106. Raveh, B.; Karp, J. M.; Sparks, S.; Dutta, K.; Rout, M. P.; Sali, A.; Cowburn, D., Slide-and-exchange mechanism for rapid and selective transport through the nuclear pore complex. *Proc Natl Acad Sci U S A* **2016**, *113* (18), E2489-97.
107. Scheiner, S., AB Initio Studies of Hydrogen Bonds: The Water Dimer Paradigm. *Annual Review of Physical Chemistry* **1994**, *45* (1), 23-56.
108. Phillips, D. C., THE HEN EGG-WHITE LYSOZYME MOLECULE. *Proceedings of the National Academy of Sciences* **1967**, *57* (3), 483.
109. Rosta, E.; Nowotny, M.; Yang, W.; Hummer, G., Catalytic Mechanism of RNA Backbone Cleavage by Ribonuclease H from QM/MM Simulations. *Journal of the American Chemical Society* **2011**, *133* (23), 8934-8941.
110. Mukherjee, A., Entropy Balance in the Intercalation Process of an Anti-Cancer Drug Daunomycin. *The Journal of Physical Chemistry Letters* **2011**, *2* (24), 3021-3026.
111. Lins, L.; Brasseur, R., The hydrophobic effect in protein folding. *The FASEB Journal* **1995**, *9* (7), 535-540.
112. Mondal, S.; Mukherjee, S.; Bagchi, B., Protein Hydration Dynamics: Much Ado about Nothing? *The Journal of Physical Chemistry Letters* **2017**, *8* (19), 4878-4882.
113. King, J. T.; Arthur, E. J.; Brooks, C. L.; Kubarych, K. J., Site-Specific Hydration Dynamics of Globular Proteins and the Role of Constrained Water in Solvent Exchange with Amphiphilic Cosolvents. *The Journal of Physical Chemistry B* **2012**, *116* (19), 5604-5611.
114. Maroncelli, M., The dynamics of solvation in polar liquids. *Journal of Molecular Liquids* **1993**, *57*, 1-37.

115. Gertner, B. J.; Whitnell, R. M.; Wilson, K. R.; Hynes, J. T., Activation to the transition state: reactant and solvent energy flow for a model SN2 reaction in water. *Journal of the American Chemical Society* **1991**, *113* (1), 74-87.
116. Maroncelli, M.; Macinnis, J.; Fleming, G. R., Polar Solvent Dynamics and Electron-Transfer Reactions. *Science* **1989**, *243* (4899), 1674.
117. Heitele, H., Dynamic Solvent Effects on Electron-Transfer Reactions. *Angewandte Chemie International Edition in English* **1993**, *32* (3), 359-377.
118. Jimenez, R.; Fleming, G. R.; Kumar, P. V.; Maroncelli, M., Femtosecond solvation dynamics of water. *Nature* **1994**, *369*, 471.
119. Nandi, N.; Roy, S.; Bagchi, B., Ultrafast solvation dynamics in water: Isotope effects and comparison with experimental results. *The Journal of Chemical Physics* **1995**, *102* (3), 1390-1397.
120. Nandi, N.; Bhattacharyya, K.; Bagchi, B., Dielectric Relaxation and Solvation Dynamics of Water in Complex Chemical and Biological Systems. *Chemical Reviews* **2000**, *100* (6), 2013-2046.
121. Pal, S. K.; Zewail, A. H., Dynamics of Water in Biological Recognition. *Chemical Reviews* **2004**, *104* (4), 2099-2124.
122. Pal, S. K.; Peon, J.; Bagchi, B.; Zewail, A. H., Biological Water: Femtosecond Dynamics of Macromolecular Hydration. *The Journal of Physical Chemistry B* **2002**, *106* (48), 12376-12395.
123. Andreatta, D.; Pérez Lustres, J. L.; Kovalenko, S. A.; Ernsting, N. P.; Murphy, C. J.; Coleman, R. S.; Berg, M. A., Power-Law Solvation Dynamics in DNA over Six Decades in Time. *Journal of the American Chemical Society* **2005**, *127* (20), 7270-7271.
124. Pal, N.; Verma, S. D.; Sen, S., Probe Position Dependence of DNA Dynamics: Comparison of the Time-Resolved Stokes Shift of Groove-Bound to Base-Stacked Probes. *Journal of the American Chemical Society* **2010**, *132* (27), 9277-9279.
125. Shweta, H.; Singh, M. K.; Yadav, K.; Verma, S. D.; Pal, N.; Sen, S., Effect of T-T Mismatch on DNA Dynamics Probed by Minor Groove Binders: Comparison of Dynamic Stokes Shifts of Hoechst and DAPI. *The Journal of Physical Chemistry B* **2017**, *121* (48), 10735-10748.
126. Sen, P.; Ghosh, S.; Mondal, S. K.; Sahu, K.; Roy, D.; Bhattacharyya, K.; Tominaga, K., A Femtosecond Study of Excitation-Wavelength Dependence of Solvation Dynamics in a Vesicle. *Chemistry – An Asian Journal* **2006**, *1* (1-2), 188-194.
127. Bürsing, H.; Kundu, S.; Vöhringer, P., Solvation Dynamics at Aqueous Lipid–Membrane Interfaces Explored by Temperature-Dependent 3-Pulse-Echo Peak Shifts: Influence of the Lipid Polymorphism. *The Journal of Physical Chemistry B* **2003**, *107* (10), 2404-2414.
128. Sýkora, J.; Slavíček, P.; Jungwirth, P.; Barucha, J.; Hof, M., Time-Dependent Stokes Shifts of Fluorescent Dyes in the Hydrophobic Backbone Region of a Phospholipid Bilayer: Combination of Fluorescence Spectroscopy and Ab Initio Calculations. *The Journal of Physical Chemistry B* **2007**, *111* (21), 5869-5877.
129. Hong, H.; Rinehart, D.; Tamm, L. K., Membrane Depth-Dependent Energetic Contribution of the Tryptophan Side Chain to the Stability of Integral Membrane Proteins. *Biochemistry* **2013**, *52* (25), 4413-4421.
130. Fiset, O.; Päslock, C.; Barnes, R.; Isas, J. M.; Langen, R.; Heyden, M.; Han, S.; Schäfer, L. V., Hydration Dynamics of a Peripheral Membrane Protein. *Journal of the American Chemical Society* **2016**, *138* (36), 11526-11535.
131. Dachwitz, E.; Parak, F.; Stockhausen, M., On the Dielectric Relaxation of Aqueous Myoglobin Solutions. *Berichte der Bunsengesellschaft für physikalische Chemie* **1989**, *93* (12), 1454-1458.
132. Wuthrich, K.; Billeter, M.; Guntert, P.; Luginbuhl, P.; Riek, R.; Wider, G., NMR studies of the hydration of biological macromolecules. *Faraday Discussions* **1996**, *103* (0), 245-253.
133. Halle, B., Protein hydration dynamics in solution: a critical survey. *Philosophical Transactions of the Royal Society of London. Series B: Biological Sciences* **2004**, *359* (1448), 1207.

134. Pal, S. K.; Peon, J.; Zewail, A. H., Biological water at the protein surface: Dynamical solvation probed directly with femtosecond resolution. *Proceedings of the National Academy of Sciences* **2002**, *99* (4), 1763.
135. Kamal, J. K. A.; Zhao, L.; Zewail, A. H., Ultrafast hydration dynamics in protein unfolding: Human serum albumin. *Proceedings of the National Academy of Sciences of the United States of America* **2004**, *101* (37), 13411.
136. Zhong, D.; Pal, S. K.; Zhang, D.; Chan, S. I.; Zewail, A. H., Femtosecond dynamics of rubredoxin: Tryptophan solvation and resonance energy transfer in the protein. *Proceedings of the National Academy of Sciences* **2002**, *99* (1), 13.
137. Qiu, W.; Zhang, L.; Okobiah, O.; Yang, Y.; Wang, L.; Zhong, D.; Zewail, A. H., Ultrafast Solvation Dynamics of Human Serum Albumin: Correlations with Conformational Transitions and Site-Selected Recognition. *The Journal of Physical Chemistry B* **2006**, *110* (21), 10540-10549.
138. Zhang, L.; Wang, L.; Kao, Y.-T.; Qiu, W.; Yang, Y.; Okobiah, O.; Zhong, D., Mapping hydration dynamics around a protein surface. *Proceedings of the National Academy of Sciences* **2007**, *104* (47), 18461.
139. Jia, M.; Yang, J.; Qin, Y.; Wang, D.; Pan, H.; Wang, L.; Xu, J.; Zhong, D., Determination of Protein Surface Hydration by Systematic Charge Mutations. *The Journal of Physical Chemistry Letters* **2015**, *6* (24), 5100-5105.
140. Yang, J.; Wang, Y.; Wang, L.; Zhong, D., Mapping Hydration Dynamics around a β -Barrel Protein. *Journal of the American Chemical Society* **2017**, *139* (12), 4399-4408.
141. Qin, Y.; Yang, Y.; Zhang, L.; Fowler, J. D.; Qiu, W.; Wang, L.; Suo, Z.; Zhong, D., Direct Probing of Solvent Accessibility and Mobility at the Binding Interface of Polymerase (Dpo4)-DNA Complex. *The Journal of Physical Chemistry A* **2013**, *117* (50), 13926-13934.
142. Yang, Y.; Qin, Y.; Ding, Q.; Bakhtina, M.; Wang, L.; Tsai, M.-D.; Zhong, D., Ultrafast Water Dynamics at the Interface of the Polymerase–DNA Binding Complex. *Biochemistry* **2014**, *53* (33), 5405-5413.
143. Sykora, J.; Brezovsky, J.; Koudelakova, T.; Lahoda, M.; Fortova, A.; Chernovets, T.; Chaloupkova, R.; Stepankova, V.; Prokop, Z.; Smatanova, I. K.; Hof, M.; Damborsky, J., Dynamics and hydration explain failed functional transformation in dehalogenase design. *Nature Chemical Biology* **2014**, *10*, 428.
144. Jha, A.; Ishii, K.; Udgaonkar, J. B.; Tahara, T.; Krishnamoorthy, G., Exploration of the Correlation between Solvation Dynamics and Internal Dynamics of a Protein. *Biochemistry* **2011**, *50* (3), 397-408.
145. Qin, Y.; Wang, L.; Zhong, D., Dynamics and mechanism of ultrafast water–protein interactions. *Proceedings of the National Academy of Sciences* **2016**, *113* (30), 8424.
146. Gallat, F. X.; Laganowsky, A.; Wood, K.; Gabel, F.; van Eijck, L.; Wuttke, J.; Moulin, M.; Härtlein, M.; Eisenberg, D.; Colletier, J. P.; Zaccai, G.; Weik, M., Dynamical Coupling of Intrinsically Disordered Proteins and Their Hydration Water: Comparison with Folded Soluble and Membrane Proteins. *Biophysical Journal* **2012**, *103* (1), 129-136.
147. Rani, P.; Biswas, P., Diffusion of Hydration Water around Intrinsically Disordered Proteins. *The Journal of Physical Chemistry B* **2015**, *119* (42), 13262-13270.
148. Rani, P.; Biswas, P., Local Structure and Dynamics of Hydration Water in Intrinsically Disordered Proteins. *The Journal of Physical Chemistry B* **2015**, *119* (34), 10858-10867.
149. Barnes, R.; Sun, S.; Fichou, Y.; Dahlquist, F. W.; Heyden, M.; Han, S., Spatially Heterogeneous Surface Water Diffusivity around Structured Protein Surfaces at Equilibrium. *Journal of the American Chemical Society* **2017**, *139* (49), 17890-17901.
150. Uversky, V. N., Targeting intrinsically disordered proteins in neurodegenerative and protein dysfunction diseases: another illustration of the D(2) concept. *Expert Review of Proteomics* **2010**, *7* (4), 543-564.

151. Pavlova, A.; Cheng, C.-Y.; Kinnebrew, M.; Lew, J.; Dahlquist, F. W.; Han, S., Protein structural and surface water rearrangement constitute major events in the earliest aggregation stages of tau. *Proceedings of the National Academy of Sciences of the United States of America* **2016**, *113* (2), E127-E136.
152. Arya, S.; Singh, A. K.; Khan, T.; Bhattacharya, M.; Datta, A.; Mukhopadhyay, S., Water Rearrangements upon Disorder-to-Order Amyloid Transition. *The Journal of Physical Chemistry Letters* **2016**, *7* (20), 4105-4110.
153. Mims, M. P.; Sturgis, C. B.; Sparrow, J. T.; Morrisett, J. D., Acrylodan can label amino as well as sulfhydryl groups: Results with low-density lipoprotein, lipoprotein[a], and lipid-free proteins. *Biochemistry* **1993**, *32* (35), 9215-9220.
154. Time-Domain Lifetime Measurements. In *Principles of Fluorescence Spectroscopy*, Lakowicz, J. R., Ed. Springer US: Boston, MA, 2006; pp 97-155.
155. Time-Dependent Anisotropy Decays. In *Principles of Fluorescence Spectroscopy*, Lakowicz, J. R., Ed. Springer US: Boston, MA, 2006; pp 383-412.
156. Rice, S. A.; Kenney-Wallace, G. A., Time-resolved fluorescence depolarization studies of rotational relaxation in viscous media. *Chemical Physics* **1980**, *47* (2), 161-170.
157. Dynamics of Solvent and Spectral Relaxation. In *Principles of Fluorescence Spectroscopy*, Lakowicz, J. R., Ed. Springer US: Boston, MA, 2006; pp 237-276.
158. Middelhoek, E. R.; Zhang, H.; Verhoeven, J. W.; Glasbeek, M., Subpicosecond studies of the solvation dynamics of fluoroprobe in liquid solution. *Chemical Physics* **1996**, *211* (1), 489-497.
159. Lu, W.; Kim, J.; Qiu, W.; Zhong, D., Femtosecond studies of tryptophan solvation: correlation function and water dynamics at lipid surfaces. *Chemical Physics Letters* **2004**, *388* (1), 120-126.
160. Energy Transfer. In *Principles of Fluorescence Spectroscopy*, Lakowicz, J. R., Ed. Springer US: Boston, MA, 2006; pp 443-475.
161. Eggeling, C.; Berger, S.; Brand, L.; Fries, J. R.; Schaffer, J.; Volkmer, A.; Seidel, C. A. M., Data registration and selective single-molecule analysis using multi-parameter fluorescence detection. *Journal of Biotechnology* **2001**, *86* (3), 163-180.
162. Sisamakos, E.; Valeri, A.; Kalinin, S.; Rothwell, P. J.; Seidel, C. A. M., Chapter 18 - Accurate Single-Molecule FRET Studies Using Multiparameter Fluorescence Detection. In *Methods in Enzymology*, Walter, N. G., Ed. Academic Press: 2010; Vol. 475, pp 455-514.
163. Kudryavtsev, V.; Sikor, M.; Kalinin, S.; Mokranjac, D.; Seidel, C. A. M.; Lamb, D. C., Combining MFD and PIE for Accurate Single-Pair Förster Resonance Energy Transfer Measurements. *ChemPhysChem* **2012**, *13* (4), 1060-1078.
164. Enderlein, J.; Goodwin, P. M.; Van Orden, A.; Patrick Ambrose, W.; Erdmann, R.; Keller, R. A., A maximum likelihood estimator to distinguish single molecules by their fluorescence decays. *Chemical Physics Letters* **1997**, *270* (5), 464-470.
165. Lee, N. K.; Kapanidis, A. N.; Wang, Y.; Michalet, X.; Mukhopadhyay, J.; Ebright, R. H.; Weiss, S., Accurate FRET Measurements within Single Diffusing Biomolecules Using Alternating-Laser Excitation. *Biophysical Journal* **2005**, *88* (4), 2939-2953.
166. Fluorescence Correlation Spectroscopy. In *Principles of Fluorescence Spectroscopy*, Lakowicz, J. R., Ed. Springer US: Boston, MA, 2006; pp 797-840.
167. Fischermeier, E.; Pospíšil, P.; Sayed, A.; Hof, M.; Solioz, M.; Fahmy, K., Dipolar Relaxation Dynamics at the Active Site of an ATPase Regulated by Membrane Lateral Pressure. *Angewandte Chemie International Edition* **2016**, *56* (5), 1269-1272.
168. Prendergast, F. G.; Meyer, M.; Carlson, G. L.; Iida, S.; Potter, J. D., Synthesis, spectral properties, and use of 6-acryloyl-2-dimethylaminonaphthalene (Acrylodan). A thiol-selective, polarity-sensitive fluorescent probe. *Journal of Biological Chemistry* **1983**, *258* (12), 7541-7544.

169. Kumbhakar, M.; Goel, T.; Mukherjee, T.; Pal, H., Role of Micellar Size and Hydration on Solvation Dynamics: A Temperature Dependent Study in Triton-X-100 and Brij-35 Micelles. *The Journal of Physical Chemistry B* **2004**, *108* (50), 19246-19254.
170. Kumbhakar, M.; Goel, T.; Mukherjee, T.; Pal, H., Nature of the Water Molecules in the Palisade Layer of a Triton X-100 Micelle in the Presence of Added Salts: A Solvation Dynamics Study. *The Journal of Physical Chemistry B* **2005**, *109* (29), 14168-14174.
171. Li, X.-H.; Culver, J. A.; Rhoades, E., Tau Binds to Multiple Tubulin Dimers with Helical Structure. *Journal of the American Chemical Society* **2015**, *137* (29), 9218-9221.
172. Al-Hassan, K. A.; Khanfer, M. F., Fluorescence Probes for Cyclodextrin Interiors. *Journal of Fluorescence* **1998**, *8* (2), 139-152.
173. Solvent and Environmental Effects. In *Principles of Fluorescence Spectroscopy*, Lakowicz, J. R., Ed. Springer US: Boston, MA, 2006; pp 205-235.
174. Jain, N.; Narang, D.; Bhasne, K.; Dalal, V.; Arya, S.; Bhattacharya, M.; Mukhopadhyay, S., Direct Observation of the Intrinsic Backbone Torsional Mobility of Disordered Proteins. *Biophysical Journal* **111** (4), 768-774.
175. Samsonov, S.; Teyra, J.; Pisabarro, M. T., A molecular dynamics approach to study the importance of solvent in protein interactions. *Proteins: Structure, Function, and Bioinformatics* **2008**, *73* (2), 515-525.
176. Mukherjee, S.; Mondal, S.; Deshmukh, A. A.; Gopal, B.; Bagchi, B., What Gives an Insulin Hexamer Its Unique Shape and Stability? Role of Ten Confined Water Molecules. *The Journal of Physical Chemistry B* **2018**, *122* (5), 1631-1637.
177. Li, T.; Hassanali, A. A.; Kao, Y.-T.; Zhong, D.; Singer, S. J., Hydration Dynamics and Time Scales of Coupled Water-Protein Fluctuations. *Journal of the American Chemical Society* **2007**, *129* (11), 3376-3382.
178. Lindorff-Larsen, K.; Maragakis, P.; Piana, S.; Eastwood, M. P.; Dror, R. O.; Shaw, D. E., Systematic Validation of Protein Force Fields against Experimental Data. *PLOS ONE* **2012**, *7* (2), e32131.
179. Mercadante, D.; Milles, S.; Fuertes, G.; Svergun, D. I.; Lemke, E. A.; Gräter, F., Kirkwood-Buff Approach Rescues Overcollapse of a Disordered Protein in Canonical Protein Force Fields. *The Journal of Physical Chemistry B* **2015**, *119* (25), 7975-7984.
180. Huang, J.; Rauscher, S.; Nawrocki, G.; Ran, T.; Feig, M.; de Groot, B. L.; Grubmüller, H.; MacKerell Jr, A. D., CHARMM36m: an improved force field for folded and intrinsically disordered proteins. *Nature Methods* **2016**, *14*, 71.
181. Rauscher, S.; Gapsys, V.; Gajda, M. J.; Zweckstetter, M.; de Groot, B. L.; Grubmüller, H., Structural Ensembles of Intrinsically Disordered Proteins Depend Strongly on Force Field: A Comparison to Experiment. *Journal of Chemical Theory and Computation* **2015**, *11* (11), 5513-5524.
182. Zachariae, U.; Grubmüller, H., Importin- β : Structural and Dynamic Determinants of a Molecular Spring. *Structure* **16** (6), 906-915.
183. Mitrousis, G.; Olia, A. S.; Walker-Kopp, N.; Cingolani, G., Molecular Basis for the Recognition of Snurportin 1 by Importin β . *Journal of Biological Chemistry* **2008**, *283* (12), 7877-7884.
184. Dobryakov, A. L.; Kovalenko, S. A.; Weigel, A.; Pérez-Lustres, J. L.; Lange, J.; Müller, A.; Ernsting, N. P., Femtosecond pump/supercontinuum-probe spectroscopy: Optimized setup and signal analysis for single-shot spectral referencing. *Review of Scientific Instruments* **2010**, *81* (11), 113106.
185. Dallmann, A.; Pfaffe, M.; Mügge, C.; Mahrwald, R.; Kovalenko, S. A.; Ernsting, N. P., Local THz Time Domain Spectroscopy of Duplex DNA via Fluorescence of an Embedded Probe. *The Journal of Physical Chemistry B* **2009**, *113* (47), 15619-15628.
186. Hill, J.; Huskic, D.; Parker, J.; Carpino, R.; Olsen, K. W., Modification of Bovine Serum Albumin (BSA) with a Maleimido-functionalized, 8-arm Polyethylene Glycol Backbone (Mal-PEG8) as a Drug Delivery System. *The FASEB Journal* **2017**, *31* (1_supplement), 922.7-922.7.

187. Steinbach, P. J.; Chu, K.; Frauenfelder, H.; Johnson, J. B.; Lamb, D. C.; Nienhaus, G. U.; Sauke, T. B.; Young, R. D., Determination of rate distributions from kinetic experiments. *Biophysical Journal* **1992**, *61* (1), 235-245.
188. É, C.; Moussaoui, S.; Idier, J.; Mariette, F., Efficient Maximum Entropy Reconstruction of Nuclear Magnetic Resonance T1-T2 Spectra. *IEEE Transactions on Signal Processing* **2010**, *58* (12), 6040-6051.
189. Livesey, A. K.; Licinio, P.; Delaye, M., Maximum entropy analysis of quasielastic light scattering from colloidal dispersions. *The Journal of Chemical Physics* **1986**, *84* (9), 5102-5107.
190. Andreatta, D.; Sen, S.; Pérez Lustres, J. L.; Kovalenko, S. A.; Ernsting, N. P.; Murphy, C. J.; Coleman, R. S.; Berg, M. A., Ultrafast Dynamics in DNA: "Fraying" at the End of the Helix. *Journal of the American Chemical Society* **2006**, *128* (21), 6885-6892.
191. Pal, N.; Shweta, H.; Singh, M. K.; Verma, S. D.; Sen, S., Power-Law Solvation Dynamics in G-Quadruplex DNA: Role of Hydration Dynamics on Ligand Solvation inside DNA. *The Journal of Physical Chemistry Letters* **2015**, *6* (9), 1754-1760.
192. Bagchi, B., Anomalous power law decay in solvation dynamics of DNA: a mode coupling theory analysis of ion contribution. *Molecular Physics* **2014**, *112* (9-10), 1418-1426.
193. Sen, S.; Gearheart, L. A.; Rivers, E.; Liu, H.; Coleman, R. S.; Murphy, C. J.; Berg, M. A., Role of Monovalent Counterions in the Ultrafast Dynamics of DNA. *The Journal of Physical Chemistry B* **2006**, *110* (26), 13248-13255.
194. Sen, S.; Andreatta, D.; Ponomarev, S. Y.; Beveridge, D. L.; Berg, M. A., Dynamics of Water and Ions Near DNA: Comparison of Simulation to Time-Resolved Stokes-Shift Experiments. *Journal of the American Chemical Society* **2009**, *131* (5), 1724-1735.